

First measurement of the sixth order cumulant of
net-proton multiplicity distributions in $\sqrt{s_{\text{NN}}} = 200$ GeV
Au+Au collisions at the STAR experiment

Toshihiro Nonaka

February 2018

First measurement of the sixth order cumulant of
net-proton multiplicity distributions in $\sqrt{s_{\text{NN}}} = 200$ GeV
Au+Au collisions at the STAR experiment

Toshihiro Nonaka
Doctral Program in Physics

Submitted to the Graduate School of
Pure and Applied Sciences
in Partial FulFillment of the Requirements
for the Degree of Doctor of Philosophy in
Science

at the
University of Tsukuba

Abstract

The existence of quarks and gluons has been explained by the standard model. In our universe, they are confined in a hadron and never observed solely due to the asymptotic freedom and the confinement explained by the Quantum Chromo Dynamics (QCD). A few micro seconds after the Big Bang, however, it is predicted that quarks and gluons are deconfined, which is called the Quark Gluon Plasma (QGP). The understanding of QGP would possibly reveal the nature of the early universe. Heavy ion colliding experiments have been carried out in order to form the QGP in the laboratory. Based of the various results obtained in the last two decades, we have definitely succeeded to form the QGP in the heavy ion colliding experiments. The hadron gas phase and the QGP phase are thus drawn in the QCD phase diagram as a function of the temperature (T) and the baryon chemical potential (μ_B). The next step is to understand the phase structure between those two phases. According to the Lattice Gauge Theory calculation, the transition from QGP to hadronic system at small μ_B has been considered as a smooth crossover, while lots of model calculations predict the first order phase transition at large μ_B . If the first order phase transition exists at large μ_B , the QCD critical end point should exist at the lower density end of the phase boundary. In Relativistic Heavy Ion Collider (RHIC), the Beam Energy Scan (BES) program is performed to search for the QCD phase structure. By changing the colliding energy, various different T- μ_B regions would be explored in the QCD phase diagram. Several recent results from the BES program the STAR experiments indicate possible signal from the first order phase transition and the critical point, although they are not yet conclusive. Beside these intensive searches for the phase structure at large μ_B , experimental inputs for understanding the structure at small μ_B are still missing, where a smooth crossover is predicted by the Lattice Gauge Theory calculation. The large number of observables are expected to be not very much sensitive to the crossover transition due to the predicted continuity of the phase transition.

Fluctuation of conserved quantities is one of the powerful tools to study the QCD phase structure especially to find the critical end point, where the correlation length could change or diverge. One of the possible ways to test the prediction for a smooth crossover is to measure the higher order cumulants of net-baryon or net-charge multiplicity distribution. Net-proton multiplicity distributions can be studied as a reasonable proxy for net-baryon distributions. The STAR experiment has measured the fourth order cumulant ratio ($\kappa\sigma^2 = C_4/C_2$) of net-proton multiplicity distribution in Au+Au collisions with its value of about ~ 0.92 at $\sqrt{s_{NN}} = 200$ GeV, which is consistent with the model prediction of a hadronic gas. Generally the higher order the cumulant, the more sensitive it is to the change of the correlation length. Therefore the signature of the phase transition could be observed via the fluctuation measurements of the higher order cumulants. Correction methods on various backgrounds and experimental artifacts have not been established yet. It is pointed out that the previous methods used in the STAR experiment up to the fourth order cumulant would not be corrected for the non-binomial detector effects, and possible additional effect from the volume fluctuations from participants has not been fully considered and corrected. Since the higher order cumulant consists of the combination of all the lower order cumulants, therefore the sixth order cumulants will be largely affected by those effects compared to the lower order cumulants. For the measurement of the sixth order cumulant, it is thus essential to further investigate the existing method and to develop new methods for various corrections for the final experimental and detector effects as well as for the initial physics effects like the participant fluctuations.

More efficient methods have been developed for the efficiency correction on cumulants based on the binomial model of the experimental detector efficiency. The calculation cost has been reduced by factor of 1/100 compared to the conventional previous formulas. A new unfolding method has been developed,

which is necessary to correct the non-binomial experimental detector effect. The effect of the volume fluctuation on higher order cumulants has also been investigated with two methods, the Centrality Bin Width Correction (CBWC) and the Volume Fluctuation Correction (VFC). These methods are implemented to the analysis on the sixth order cumulant of the net-proton multiplicity distribution in Au+Au collisions at $\sqrt{s_{\text{NN}}} = 200$ GeV. The centrality dependence of C_6/C_2 shows systematically negative values from mid-central to the most central collisions, which might be interpreted as a signal of a smooth crossover. Results are compared to the Poisson and the binomial baselines. Over the wide centrality region, C_6/C_2 shows systematically smaller values from the Poisson baseline. The binomial baseline can describe the results better than the Poisson baseline, however results in 30–40 and 10–20% centralities show even smaller values than the binomial expectation. These experimental results are also compared to the UrQMD model. It is found that the UrQMD model is closed to the Poisson baseline. The results show systematic suppression compared to the UrQMD model for all centralities except for the most central collisions. More statistics would be necessary in order to draw more definite conclusions about the possible signals from the crossover phase transition.

Acknowledgement

I would like to appreciate Prof. ShinIchi Esumi for his kind guidance to the physics of the heavy ion colliding experiment. I really enjoyed the discussions on fluctuation analysis, which was very exciting so that I forgot about the time. My fluctuation analysis all started with Dr. Hiroshi Masui. He kindly guided me to the fluctuation analysis in the STAR experiment. Especially, the automation technique for the efficiency correction on cumulants was so useful and impressive. Prof. Xiaofeng Luo, Prof. Nu Xu and Prof. Bedangas Mohanty also helped me fit into the fluctuation analysis in STAR. They kindly taught me the analysis details on the higher order fluctuations. Discussions with them were so fruitful. I would like to express my special thanks to Dr. Masakiyo Kitazawa in Osaka University. His short-term class in Tsukuba University when I was a master course is one of the reason for me to have an interested in the fluctuation analysis. His ideas on the efficiency correction were so impressive and made the calculations quite easy and efficient. I would like to appreciate Dr. Takafumi Niida, Dr. Takahito Todoroki and Dr. Sanshiro Mizuno. They kindly supported me for our shift taking, life in BNL and the analysis in the STAR environment.

My motivation on the heavy ion physics in Ph.D course was originally motivated by MRPC-TOF development during master course student. Prof. Tatsuya Chujo led me to the MRPC development and made me realize the pleasure to contribute to the development of the fast timing detector. Prof. Motoi Inaba kindly provided me great supports on the electronics especially on pre-amplifiers for MRPC. Prof. Yasuo Miake always surprised me by his shape questions, which became hints for further understanding of MRPC. Mr. Sumio Kato kindly managed the network environment.

I would like to thank Ritsuya Hosokawa for his kind support as Ph.D student in the same grade. I was always surprised at his heavy drinking. I would like to appreciate Naoto Tanaka and Hiroshi Nakagomi. Fishing with them is a good memory. I would like to thank R. Aoyama and T. Sugiura. We work together on the STAR experiment. Short stay with them in BNL for the shift taking was quite hard. Technical and physics discussions with them were so exciting.

Many thanks to maser and doctoral students in our high energy nuclear collision group (utkhii) in Tsukuba group, especially to H. Yokoyama, K. Gunji, T. Nakajima, S. Horiuchi, D. Watanabe, K. Ohsima, H. Ozaki, K. Kihara, T. Kobayashi, W. Sato, M. Hirano, J. Lee, I. Sakatani, T. Shioya, H. Yamamoto, K. Ito, Y. Fukuda, B. C. Kim, R. Koyama, S. Kudo, K. Matsunaga, Y. Rebaza, K. Sato, T. Ichisawa, H. Kato, D. Kawana, Y. Kawamura, K. Nakagawa and T. Suzuki. My reseach life and the coffee time with them were quite comfortable. I would like to appreciate S. Sakai and Y. Watanabe for the physics discussions and holding banquets.

I would like to give a special thanks to Hitomi Koyama, Ikuo Koyama, Kyoko Koyama, Ryota Koyama, Yuta Koyama and Tora-hei Koyama for their continuous supporting and encouragement on my research life. They warmly welcomed me to their house, trip and fishing.

Finally, I would like to express my gratitude to my family, Yasuyuki, Kazuko and Takafumi, for their understanding, scolding and encouraging for over two decades.

I wouldn't be who I am now without all those who worked, played and lived with me. I will never forget the feeling of gratitude and all the memories with them.

Contents

1	Introduction	2
1.1	Quantum Chromo Dynamics (QCD)	2
1.1.1	Asymptotic freedom and confinement	2
1.1.2	QCD phase diagram	3
1.2	Search for the QCD phase structure	3
1.2.1	Relativistic heavy ion collision	4
1.2.2	Beam Energy Scan Program (BES)	4
1.2.3	Freeze-out line	5
1.2.4	Turn-off the QGP signal	5
1.2.5	First order phase transition	6
1.2.6	Critical end point	7
1.2.7	Physics motivation – search for the crossover	8
1.2.8	Technical motivation – investigate the analysis methods	10
1.3	Moments and cumulants	11
1.3.1	Definitions	11
1.3.2	Additivity of cumulants	12
1.3.3	Factorial moments and factorial cumulants	13
1.3.4	Cumulants of conserved quantities	13
1.3.5	Statistical baseline	14
2	Experiment	17
2.1	Relativistic Heavy Ion Collider (RHIC)	17
2.2	The STAR detector	17
2.2.1	Time Projection Chamber (TPC)	18
2.2.2	Time Of Flight (TOF)	20
2.2.3	Vertex Position Detector (VPD)	22
2.3	Datasets	27
2.3.1	Run by run QA	27
2.3.2	Event and track selection	27
2.3.3	Proton identification	29
3	Detector Effect	31
3.1	Efficiency correction	31
3.1.1	Single efficiency bin	31
3.1.2	Many efficiency bins	32
3.1.3	Importance of precise efficiency correction	34
3.1.4	Statistical error estimation	36

3.2	Unfolding	37
3.2.1	Methodology	37
3.2.2	Binomial model	44
3.3	Embedding simulation	46
3.3.1	Single particle efficiency	46
3.3.2	Efficiency distribution	47
4	Volume Fluctuation	51
4.1	Centrality Bin Width Correction (CBWC)	51
4.1.1	Centrality Bin Width Correction (CBWC)	51
4.1.2	Auto-correlation effect	52
4.2	Volume Fluctuation Correction	52
4.2.1	Derivation	53
4.2.2	Toy model	55
4.3	CBWC vs VFC	55
4.3.1	Centrality resolution effect	55
4.3.2	UrQMD model	56
5	Results and Discussions	60
5.1	Systematic uncertainties	60
5.2	Up to 4th order cumulants	62
5.3	6th order fluctuation	63
5.4	Interpretation	67
5.5	Comparison with theoretical calculations	67
6	Conclusions	70
A	Centrality definition	71
B	Tips on the efficiency correction	74
B.1	Stirling number of the first kind	74
B.2	Factorial moments with the binomial model	74
C	Net-proton distribution	76
C.1	Shape for the sixth order cumulant	76
C.2	Net-proton distribution	77
D	Robustness to the time dependence	80

List of Figures

1.1	(Left) Coupling constant α as a function of momentum transfer [1]. (Right) Static potential between quarks and antiquarks calculated by lattice QCD as a function of distance [2].	3
1.2	Example of QCD phase diagram [3].	4
1.3	An image of the time evolution of the relativistic heavy ion collision [4].	5
1.4	Extracted chemical freeze-out temperature T_{ch} as a function of baryon chemical potential μ_{B} , compared with the theoretical predictions (left), and the kinetic freeze-out temperature T_{kin} as a function of the average transverse radial flow velocity $\langle\beta\rangle$ (right) measured at the STAR experiment in BES energies. [5].	6
1.5	(Left) The charged hadron yields normalized by number of binary collisions as a function of the number of participant nucleons at $3.0 < p_T < 3.5$ GeV/c and $4.0 < p_T < 4.5$ GeV/c in BES energies [6]. (Right) The slope parameter of the directed flow at midrapidity $dv_1/dy _{y=0}$ for proton, antiproton and netproton as a function of beam energy [7].	7
1.6	Published results of the ratio of higher order cumulants up to fourth order as a function of beam energy for net-charge (left), net-proton (middle) and net-kaon (right) multiplicity distributions [8–10].	8
1.7	Recent STAR preliminary results on $\kappa\sigma^2$ (left) and $S\sigma$ (middle) for net-proton multiplicity distributions measured at $0.4 < p_T < 2.0$ (GeV/c) as a function of beam energy [11]. The theoretical prediction is also shown in the right hand side panel [12].	9
1.8	The energy density computed by lattice QCD as a function of the temperature [13]. .	9
1.9	(Left) The ratio of the sixth to second order baryon number susceptibility ($\chi_6^{\text{B}}/\chi_2^{\text{B}}$) as a function of temperature for vanishing and finite density μ_q/T . The green shaded area represents the chiral crossover region. (Right) The expected values of $\chi_4^{\text{B}}/\chi_2^{\text{B}}$ and $\chi_6^{\text{B}}/\chi_2^{\text{B}}$ with different freeze-out conditions [14].	10
1.10	An example of skewness and kurtosis [15].	12
2.1	An aerial photo of RHIC.	18
2.2	Overview of the STAR detector	19
2.3	A schematic of the STAR TPC [16]	21
2.4	A schematic on the anode pad plane with one full sector [16].	21
2.5	The energy loss as a function of momentum with the Bethe-Bloch expectations. The magnetic field is set to be 0.25 T [16].	22
2.6	$1/\beta$ as a function of momentum, measured in Run 9 at $\sqrt{s_{\text{NN}}} = 200$ GeV in p+p collisions [17].	23
2.7	A two-side view on the MRPC detector [18].	23
2.8	A schematic on TOF trays.	24
2.9	The front view of one assembly (left) and a photograph of two assemblies (right) [19].	25

2.10	The front view of one assembly (left) and a photograph of two assemblies (right) [19].	25
2.11	Correlation of the primary vertex position along the beam pipe measured by VPD Z_{vtx}^{VPD} and measured by TPC Z_{vtx}^{TPC} , in p+p collisions at $\sqrt{s_{NN}} = 510$ GeV recorded in 2012 (left), and in Au+Au collisions at $\sqrt{s_{NN}} = 200$ GeV recorded in 2009 (right) [19]. The insets show the difference between them $\Delta Z = Z_{vtx}^{VPD} - Z_{vtx}^{TPC}$ from which the Z_{vtx} resolution of VPD can be extracted.	26
2.12	Averaged z-vertex position, radial vertex position, number of primary tracks, distance of closest approach (DCA), transverse momentum, and pseudo-rapidity as a function of run index in Run11. Mean values in the same trigger condition are shown in red solid lines, and $\pm 3\sigma$ lines are shown green.	27
2.13	(a) Radial vertex position, (b) vertex position along the beam pipe, (c) the difference of vertex positions along the beam pipe between TPC and VPD, (d) number of hit points in TPC used for the track reconstruction (e) number of hit points in TPC used for calculating dE/dx.	28
2.14	(a) Number of primary tracks associated with TOF, and (b) the number of primary tracks associated with TOF requiring $\beta > 0.1$ in the Run10 central trigger. (c) and (d) are for the Run11 minimum bias trigger.	29
2.15	(Left) dE/dx measured by TPC as a function of momentum multiplied by charge. (Right) m^2 measured by TOF as a function of momentum multiplied by charge [20].	30
3.1	Comparison of number of necessary terms in correction formulas in two methods [21].	35
3.2	Deviation of the efficiency corrected values of cumulants using averaged efficiency, assuming (a) Gauss distribution and (b) distribution that has 5% smaller cumulants than Poisson distribution.	36
3.3	Efficiency corrected C_6 and C_6/C_2 and their statistical errors estimated by bootstrap, as a function of 50 independent trials. Red dotted lines represent the averaged value for 50 trials.	37
3.4	Flowchart for our unfolding method by using simple toy model with Poisson distributions. (A) is the experimental true, (B) is the simulation true, (C) is the experimental measured and (D) is the simulation measured distribution. RM_{rev} is the reversed response matrix. (C.F._rec) and (C.F._gen) are correction functions in reconstructed and generated coordinates.	39
3.5	Cumulants up to fourth order as a function of iteration. Red lines represent the true cumulants, black lines are incremental unfolding, and blue lines are conventional unfolding. Results of independent 30 trials are superimposed.	40
3.6	Flowchart for our unfolding method by using critical a distribution. (A) is the experimental true, (B) is the simulation true, (C) is the experimental measured and (D) is the simulation measured distribution. RM_{rev} is the reversed response matrix. (C.F._rec) and (C.F._gen) are correction functions in reconstructed and generated coordinates.	41
3.7	Two-dimensional distributions for protons and antiprotons at 1 st , 20 th and 80 th iteration of incremental unfolding, and 200 th iteration of conventional unfolding Initial distributions for experiment and simulation are also shown.	42
3.8	Net-proton distributions at 1 st , 20 th and 80 th iteration of incremental unfolding, and 200 th iteration of conventional unfolding Initial distributions for experiment and simulation are also shown.	42
3.9	Cumulants up to fourth order as a function of iteration. Red lines represent the true cumulants, black lines are incremental unfolding, and blue lines are conventional unfolding. Results of independent 30 trials are superimposed.	43

3.10	Results of toy model calculation with 100 bootstrap samplings with 100k events. Cumulants up to fourth order are shown as a function of 100 independent trials. Red lines represent the averaged value over trials.	44
3.11	An image for the implementation of efficiency bins in unfolding. $N_{p(\text{pbar}), \text{low}(\text{high})}$ and $n_{p(\text{pbar}), \text{low}(\text{high})}$ are generated and reconstructed number of (anti)protons at low(high) p_T regions. $F_{p(\text{pbar}), \text{low}(\text{high})}$ is the fraction at low and high p_T regions with respect to combined p_T . $\varepsilon_{p(\text{pbar}), \text{low}(\text{high})}$ is the efficiency in a corresponding bin.	45
3.12	(Top) Unfolded distribution for protons and antiprotons at 0–5%, 5–10%, 30–40% and 70–80% centralities. (Bottom) Cumulants up to fourth order as a function of centrality. Blue squares are results of efficiency correction, and red circles are efficiency correction. Any volume fluctuation correction is not applied.	45
3.13	TPC tracking efficiency (black), TOF matching efficiency (blue) and combined efficiency at $0.8 < p_T < 2.0$ (GeV/c)(red) for protons as a function of p_T for each centrality. . .	46
3.14	p_T integrated efficiency for protons (open) and antiprotons (filled) at $0.4 < p_T < 0.8$ (GeV/c) (red) and $0.8 < p_T < 2.0$ (GeV/c) (blue) as a function of refmult3. Dotted lines are polynomial fittings.	47
3.15	TPC tracking efficiency for protons at 0–5% centrality as a function of azimuthal angles and rapidity.	47
3.16	Hypergeometric and beta-binomial distributions with $N = 10$ and $\varepsilon = 0.6$. Distributions with different α are shown in different colors. Black points represent a binomial distribution. Bottom panels show the ratio to binomial.	48
3.17	Number of reconstructed protons are plotted with different number of embedded protons from 7 to 13 in 0–5% centrality at $1.0 < p_T < 2.0$ (GeV/c), which are fitted by binomial (red), hypergeometric (blue) and beta-binomial (green) distributions. Fitting results for χ^2/NDF and α are also shown in each panel.	49
3.18	χ^2/NDF extracted from Fig. 3.17 as a function of number of embedded protons for binomial (red), hypergeometric (blue) and beta-binomial (green) fittings.	50
3.19	The non-binomial parameter α extracted from the beta-binomial fitting to the embedding data as a function of the number of input (anti)protons. Data points are fitted by $y = a/x + b$ to extrapolate to the large number of (anti)protons.	50
4.1	$\kappa\sigma^2$ (C_4/C_2) as a function of centrality with different rapidity coverage for centrality definition using UrQMD model [22].	52
4.2	$\kappa\sigma^2$ (C_4/C_2) of net-proton distribution as a function of centrality with different centrality definition using UrQMD model [22].	53
4.3	Upper panel shows the net-proton distributions at 0–5, 20–30 and 60–70% centralities. N_{part} fluctuates according to the Glauber model for red lines, while N_{part} is fixed in black lines. Lower panels show the ratio between two net-proton distributions.	55
4.4	Cumulants up to fourth order as a function of centrality. For black circles N_{part} fluctuates which includes participant fluctuation given by the Glauber model For red squares N_{part} is fixed, which are true value of cumulant in this model. Black solid lines are results of VFC, and blue crosses are results of CBWC.	56
4.5	(Left) Multiplicity distributions with 100% (red), 50% (blue) and 20% (green) centrality resolution generated by Glauber and two component model. Distributions with 50% and 20% centrality resolution were defined by random sampling from the distribution with 100% resolution. (Right) Results up to fourth order cumulant as a function of centrality without CBWC nor CBWC, with CBWC and with VFC from left to right. Dotted lines represent the true cumulants.	57

4.6	(a) The refmult3 distribution and (b) the N_{part} distribution, where the colors represent the different centralities. (c) and (d) show the two-dimensional histogram for N_p and N_{pbar} at $N_{\text{part}} = 240$ in 10-20 and 0-10% centralities.	58
4.7	Cumulants up to sixth order as a function of centrality for CBWC-N (true), CBWC-M and VFC.	59
4.8	C_3/C_2 , C_4/C_2 and C_6/C_2 as a function of centrality for CBWC-N (true), CBWC-M and VFC. The ratios of CBWC-M and VFC to CBWC-N are shown in bottom panels.	59
5.1	Centrality dependence of C_6/C_2 in Run11 without any volume fluctuation corrections. Results from the efficiency correction are shown in red circles, and results from the unfolding with the beta-binomial model are shown in green crosses.	61
5.2	Cumulants up to fourth order as a function of centrality using the experimental data. Results without CBWC nor VFC, with VFC and with CBWC. In the former two cases, results with different centrality bin width of 8bin, 16bin and 32bin (corresponding to 2.5%, 5.0% and 10% centrality step) are shown.	62
5.3	The centrality dependence of C_3/C_2 normalized by the value of Skellam (top) and C_4/C_2 (bottom) at $\sqrt{s_{\text{NN}}} = 7.7, 19.6, 62.4$ and 200 GeV. Results using CBWC are shown in blue crosses, and VFC results are shown in green triangles. The Skellam baselines are shown in dotted lines.	63
5.4	The STAR preliminary results on the beam energy dependence of $\kappa\sigma^2 = C_4/C_2$ and $S\sigma/\text{Skellam} = (C_3/C_2)/\text{Skellam}$ using CBWC [23], where VFC results at $\sqrt{s_{\text{NN}}} = 7.7, 19.6$ and 62.4 and 200 GeV are superimposed in green circles, orange diamonds and purple stars for 0-5, 5-10 and 70-80% centralities, respectively.	64
5.5	Centrality dependence of C_6/C_2 for Run10 and Run11. Statistical errors are shown in bars, while systematic uncertainties are shown in brackets. The expanded plot is shown in right hand side from 20% centrality.	65
5.6	C_6/C_2 as a function of centrality, where results from Run10 and Run11 are merged. The expanded plot is shown in right hand side from 20% centrality. Skellam and the binomial baselines are also shown.	65
5.7	C_6/C_2 as a function of centrality with Skellam baseline and the results of UrQMD model. CBWC is applied in UrQMD model as is done in experimental data.	66
5.8	C_6/C_2 as a function of centrality using CBWC or VFC for both experimental data and UrQMD model. Results with CBWC are shown in purple and the results with VFC are in green. Results of UrQMD model are shown in band.	66
5.9	Significance with respect to zero as a function of centrality for CBWC and VFC. The expanded plot is shown in right hand side panel.	67
5.10	$\chi_6^{\text{B}}/\chi_2^{\text{B}}$ calculated with the lattice QCD as a function of temperature [24]. The red shaded area is the region of interest at $\sqrt{s_{\text{NN}}} = 200$ GeV.	68
5.11	Final results on C_6/C_2 of net-proton distribution at $\sqrt{s_{\text{NN}}} = 200$ GeV, where the corresponding results calculated by the lattice QCD on the ratio of sixth to second order susceptibility of the net-baryon distribution [24] are superimposed in red shadows.	69
A.1	Luminosity dependence of averaged refmult3 in $-2 < V_z < 0$ cm. Blue markers are uncorrected and fitted by first order polynomial function (red lines) which is used for the correction. Corrected results are shown in blue markers.	71
A.2	(Left) Tail of the refmult3 distribution fitted by error function shown in a red line. The blue dotted line represents the parameter c in Eq. (A.1). (Right) Maximum value of refmult3 distribution as a function of V_z (black) and the corrected distribution (red).	72

A.3	(Left) Refmult3 distribution (black points) fitted by MC distribution generated by Glauber and two-component model (red points). (Right) Ratio of MC to refmult3 distribution. The solid blue line represents the fitting for trigger inefficiency correction.	73
C.1	A simple sketch to stack n boxes for the n-th order cumulant.	77
C.2	Gaussian distributions with the mean value of 0 and the sigma of 5, in which another two symmetric Gaussians around $N = \pm 15$ are added (left) or subtracted (right). Red lines represent the Gaussian fittings. The ratio to the fitting are shown in the bottom panels.	78
C.3	(Top) Net-proton distributions in 0-5, 30-40 and 70-80% centralities. Blue squares are the measured distribution. Red circles are unfolded distribution without any volume fluctuation corrections. Black lines represent Skellam distributions, and dotted green lines are Gaussian distributions. (Bottom) Ratios of the unfolded distribution to the Skellam and Gaussian distributions.	79
D.1	Relative deviations with respect to the true value of cumulants up to the sixth order as a function of the fraction of bad events in which the efficiency drops with $\Delta\varepsilon$	80

Chapter 1

Introduction

1.1 Quantum Chromo Dynamics (QCD)

Quantum Chromo Dynamics (QCD) is the theory of strong interactions between quarks and gluons. Quarks and gluons have three kinds of color charge, red, green and blue, and for baryons and mesons the color charge of white is required due to the combinations of constituent quarks. In this section, I introduce the important characteristics of QCD.

1.1.1 Asymptotic freedom and confinement

In electrodynamics, the coulomb interaction between two particles is given by

$$\vec{F}(\vec{r}) = k \frac{e_1 e_2}{r^2} \frac{\vec{r}}{r}, \quad \vec{r} = \vec{x} - \vec{y}, \quad r = |\vec{r}|, \quad (1.1)$$

where e denotes the charge of the particle and two particles are put in \vec{x} and \vec{y} . Equation (1.1) indicates that the coulomb force becomes repulsive when the charges for two particles are identical, and vice versa. It also indicates that the coulomb force becomes strong with small $r = |\vec{r}|$ and becomes weak with large r . In the case of QCD, however, the static potential V_s is given by

$$V_s = -\frac{4}{3} \times \frac{\alpha_s}{r} + k \times r, \quad (1.2)$$

$$\alpha_s(\mu_R^2) \approx \frac{12\pi}{(33 - 2n_q) \log(\mu_R^2 / \Lambda_{\text{QCD}}^2)}, \quad (1.3)$$

where α_s is called running coupling constant with μ_R and Λ_{QCD} being the QCD scale which are determined experimentally. This α_s becomes small in small r and becomes large in large r , which is called asymptotic freedom. Asymptotic freedom was discovered by deep inelastic scattering (DIS) experiments colliding a high energy electron to a proton, which gave an indirect evidence of quarks as well. Equation (1.3) was shown analytically from the lowest term of perturbative expansion in high energy scale. In low energy scale (long distance), α_s becomes large, which could be the reason for the confinement of quarks and gluons. However, higher order terms become more important in low energy scale, thus, the confinement of quarks cannot be shown analytically. The confinement of quarks and gluons is shown numerically by lattice QCD [2]. Lattice QCD is the non-perturbative approach of the first principles. Infinite volume is approximated with finite space of lattice, and the QCD theory is solved on the lattice numerically.

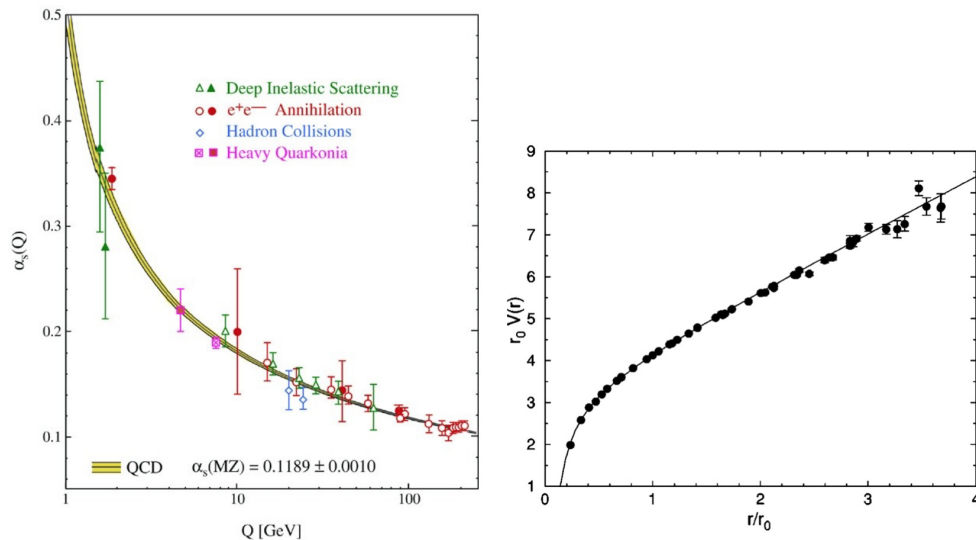


Figure 1.1: (Left) Coupling constant α as a function of momentum transfer [1]. (Right) Static potential between quarks and antiquarks calculated by lattice QCD as a function of distance [2].

1.1.2 QCD phase diagram

The state of the QCD matter can be characterized by the two-dimensional plane of the temperature (T) and the baryon chemical potential (μ_B), which is called the QCD phase diagram. Figure 1.2 shows one example of the QCD phase diagram. In high temperature and high density region, quarks and gluons are released from the confinement, then the strongly interacting matter called quark gluon plasma (QGP) is created. In high density and low temperature region, color superconductors are predicted, which is also expected to exist in neutron stars. We note that the boundaries shown in Fig. 1.2 are still predictions and there is no experimental evidence. Theoretically, it has been shown by the lattice QCD that the phase transition between the hadronic phase and the QGP phase is smooth crossover at vanishing baryon chemical potential [25, 26], while in nonzero μ_B , the first order phase transition is predicted by various models. These predictions make it easy for us to expect the QCD critical point [3, 27, 28], where the first order phase transition end.

1.2 Search for the QCD phase structure

For the last several decades, relativistic heavy ion collisions have been carried out to discover and study the QGP. Considering various experimental results, it may be no doubt that the QGP has been successfully created experimentally. Our next step is to shed light on the QCD phase structure. So far, however, we find only three things from the experiments as below:

- The QCD phase diagram contains the QGP phase as well as the hadron gas phase.
- The chemical freeze-out line can be drawn in the phase diagram, which is very close to the chiral crossover region estimated by the lattice QCD.
- The kinetic freeze-out line can be drawn at the low temperature side of the chemical freeze-out line.

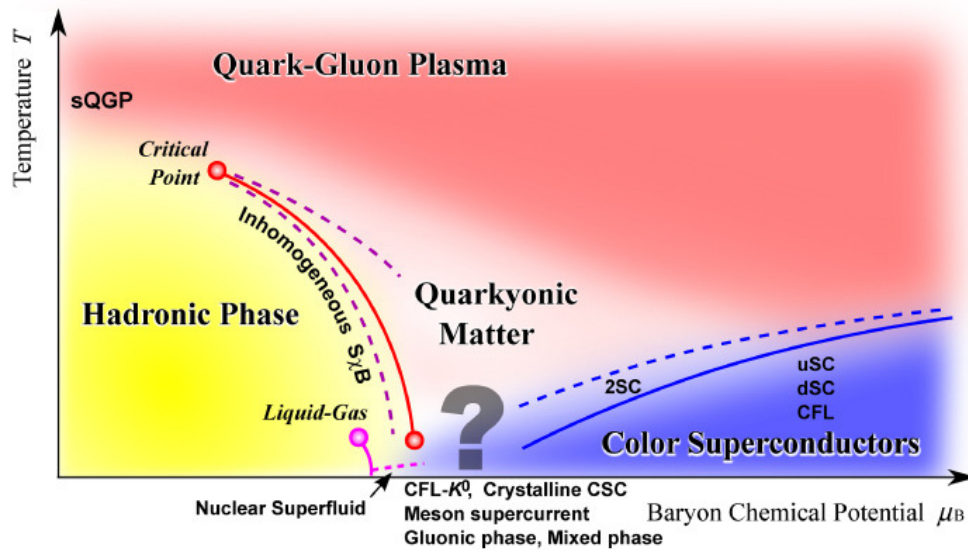


Figure 1.2: Example of QCD phase diagram [3].

Therefore, the QCD phase diagram in Fig. 1.2 is nothing more than an image expected from few experimental inputs and so many theoretical predictions. Most importantly, experimental inputs on the location and the order of the phase transition line are still missing. In this section, we introduce some experimental attempts and results to reveal the QCD phase structure following the dynamics on the relativistic heavy ion collisions.

1.2.1 Relativistic heavy ion collision

A few micro seconds after the Big Bang, our universe would be the QGP. The high energy heavy ion colliding experiment is the unique way to create the QGP and study the initial stage of our universe in the laboratory. Fig. 1.3 shows an image of the time evolution of the relativistic heavy ion collision. In the initial stage with two accelerated heavy ions, color glass condensate (CGC) could be realized in each heavy ion. At the collision of two heavy ions, hard scattering occurs, and the thermalization is achieved. The QGP can be formed if the colliding energy is substantially large. At this time, the hydrodynamical expansion starts. With decreasing the temperature and density of the system, the hadronization of QGP starts. After hadronization ceases, the chemical freeze-out occurs in which the yields of various hadron species are fixed, followed by the kinetic freeze-out, after when no more momentum transfer occurs.

1.2.2 Beam Energy Scan Program (BES)

The beam energy scan program has been carried out at $\sqrt{s_{NN}} = 7.7, 11.5, 14.5, 19.6, 27, 39, 62.4$ and 200 GeV in 2010, 2011 and 2014 at RHIC in order to search for the QCD phase structure. Heavy ion collisions with high beam energy allows nucleons to slip through each other with dropping large energy into the system, which leads to high temperature and low density of the created medium. Once we decrease the beam energy, however, the stopping effect of nucleons becomes dominant. Then the created system will be low temperature with high density. Therefore, the structure of the QCD phase diagram can be scanned and investigated by changing the colliding beam energy. From the next

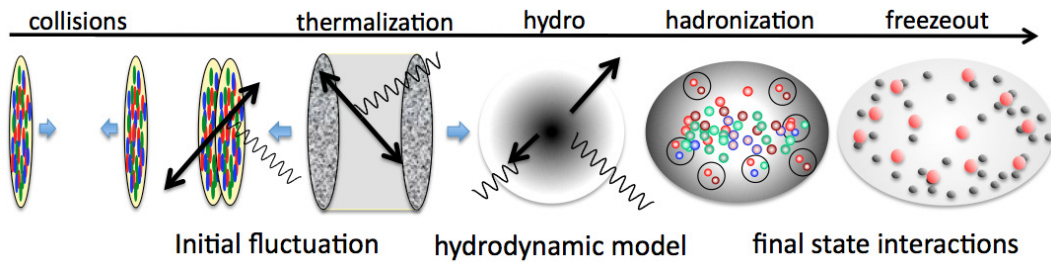


Figure 1.3: An image of the time evolution of the relativistic heavy ion collision [4].

subsection, we introduce some results from BES and discuss the expected scenarios on the QCD phase structure.

1.2.3 Freeze-out line

Two kinds of freeze-out are considered in heavy ion collisions: the chemical freeze-out and the kinetic freeze-out. The chemical freeze-out is the time when inelastic collisions cease and particle yields are fixed. Thus, the chemical freeze-out parameters are extracted by fitting the particle yields with the statistical thermal model. After the chemical freeze-out, elastic interactions among particles will continue until the average interparticle distance becomes large enough, then momenta of particles becomes unchanged, which is called the kinetic freeze-out. The kinetic freeze-out parameters can be obtained by the simultaneous fit to the p_T spectra for different particles using the blast wave model. Figure 1.4 shows the extracted chemical freeze-out temperature T_{ch} as a function of baryon chemical potential μ_B (left), and the kinetic freeze-out temperature T_{kin} as a function of the average transverse radial flow velocity $\langle\beta\rangle$ (right) measured at the STAR experiment in BES energies. The value of T_{kin} is smaller than T_{ch} . This is consistent with the picture of the freeze-out, the chemical freeze-out occurs followed by the kinetic freeze-out. The separation between T_{kin} and T_{ch} increases with increasing the beam energy, which might be due to the increase of hadronic interactions between the chemical and kinetic freeze-out at higher beam energies. The centrality dependence of μ_B is observed, which becomes strong in low beam energies, while T_{ch} is similar for all centralities. Importantly, the lattice QCD suggests the phase transition temperature around $T_c \approx 150 - 160$ MeV, which is close to the chemical freeze-out temperature. It may indicate that the phase transition occurs right before the chemical freeze-out.

1.2.4 Turn-off the QGP signal

When we search for the existence or locations of the first order phase transition and the QCD critical point by using certain observables, we have to implicitly require that the QGP is formed at the beam energy. If not, we should not find any signals for the phase transition. In order to study onset of charged particle suppression relative to the binary collision scaling, the normalized charged hadron yields per binary collision have been measured at two p_T bins of $3.0 < p_T < 3.5$ GeV/c and $4.0 < p_T < 4.5$ GeV/c in BES energies [6], as shown in the left hand side panel in Fig. 1.5. If the QGP is formed, high p_T partons lose their energy by passing through the volume of the QGP, and the hadron yields decrease with respect to low p_T . This is called the jet-quenching effect. Thus, the suppression of high p_T hadron yields has been considered to be an evidence of the QGP being formed. On the contrary, however, an absence of this effect does not rule out the possibility of the QGP,

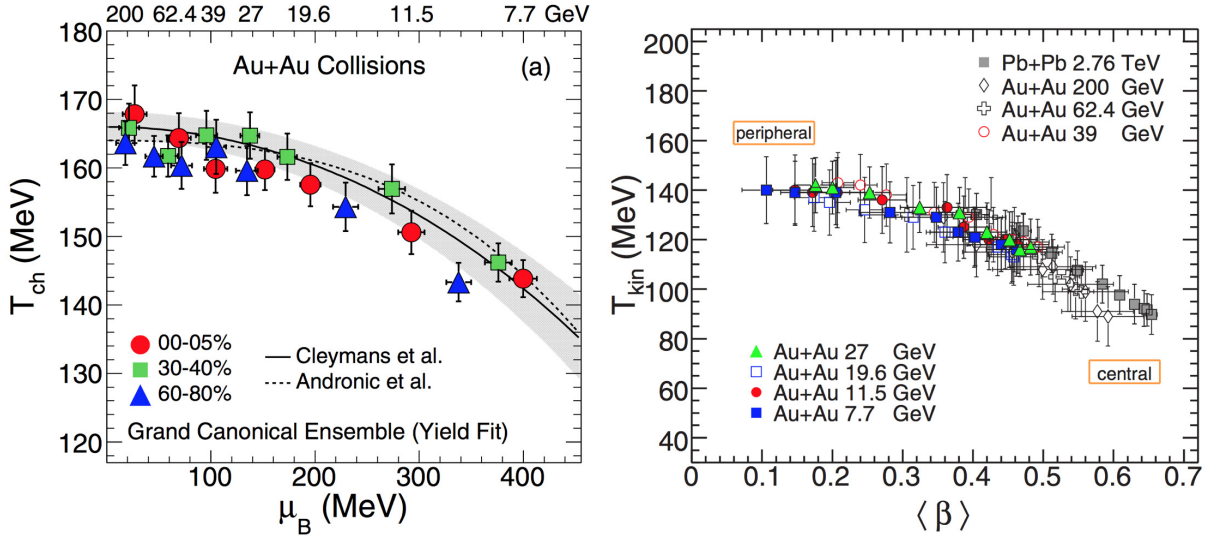


Figure 1.4: Extracted chemical freeze-out temperature T_{ch} as a function of baryon chemical potential μ_B , compared with the theoretical predictions (left), and the kinetic freeze-out temperature T_{kin} as a function of the average transverse radial flow velocity $\langle\beta\rangle$ (right) measured at the STAR experiment in BES energies. [5].

since there are other effects leading to the enhancement of hadron yields such as the Cronin effect, radial flow and particle coalescence. At 7.7 GeV and 11.5 GeV the yields increase monotonically with increasing $\langle N_{\text{part}} \rangle$. This would not prove that there is no jet-quenching effect due to the absence of the QGP, but simply that the enhancement effects grow rapidly than jet-quenching effect. The fact, that the yields become flat in central collisions 14.5 GeV, might be understood that the enhancement and suppression effects are comparable. In higher energies the yields show suppression in central collisions, and 200 GeV data shows the monotonic decrease with increasing $\langle N_{\text{part}} \rangle$, which would be because the jet-quenching effect is stronger than other enhancement effects. We note again that the observed enhancement of yields at the beam energy $\sqrt{s_{\text{NN}}} \leq 14.5$ GeV does not exclude the scenario that the QGP is still created in such low beam energy region. But considering that other measurements using low p_T probes also show some turn-off signal of the QGP in similar beam energy regions, the scenario of the vanishing QGP phase at the beam energy of $\sqrt{s_{\text{NN}}} \leq 14.5$ GeV may not be a bad estimate as all [29, 30].

1.2.5 First order phase transition

One possible observable to probe the first order phase transition is the directed flow v_1 , which is the first harmonic coefficient of the Fourier expansion of the azimuthal distribution. It has been predicted by hydrodynamic models that the dv_1/dy shows a minimum near midrapidity around $\sqrt{s_{\text{NN}}} = 4$ GeV for net-baryons [31]. The right hand side panel in Fig. 1.5 shows the slope parameter of the directed flow at midrapidity $dv_1/dy|_{y=0}$ for proton, antiproton and netproton as a function of beam energy [7]. The antiproton slope shows monotonic decrease with decreasing the beam energy, whereas the proton slope shows non-monotonic behaviour with the minimum value between 11.5 GeV and 19.6 GeV. This cannot be explained by the UrQMD model. Furthermore, net-proton slope exhibits sign change twice between 7.7–11.5 GeV and between 19.6–39 GeV. These results on the proton and net-proton slope are qualitatively consistent with hydrodynamics predictions, which might be a possible signal

for the first order phase transition. But we need to take care that the beam energy in which the predictions suggest the minimum value for the slope parameter is different from the observation. Further theoretical understandings are necessary.

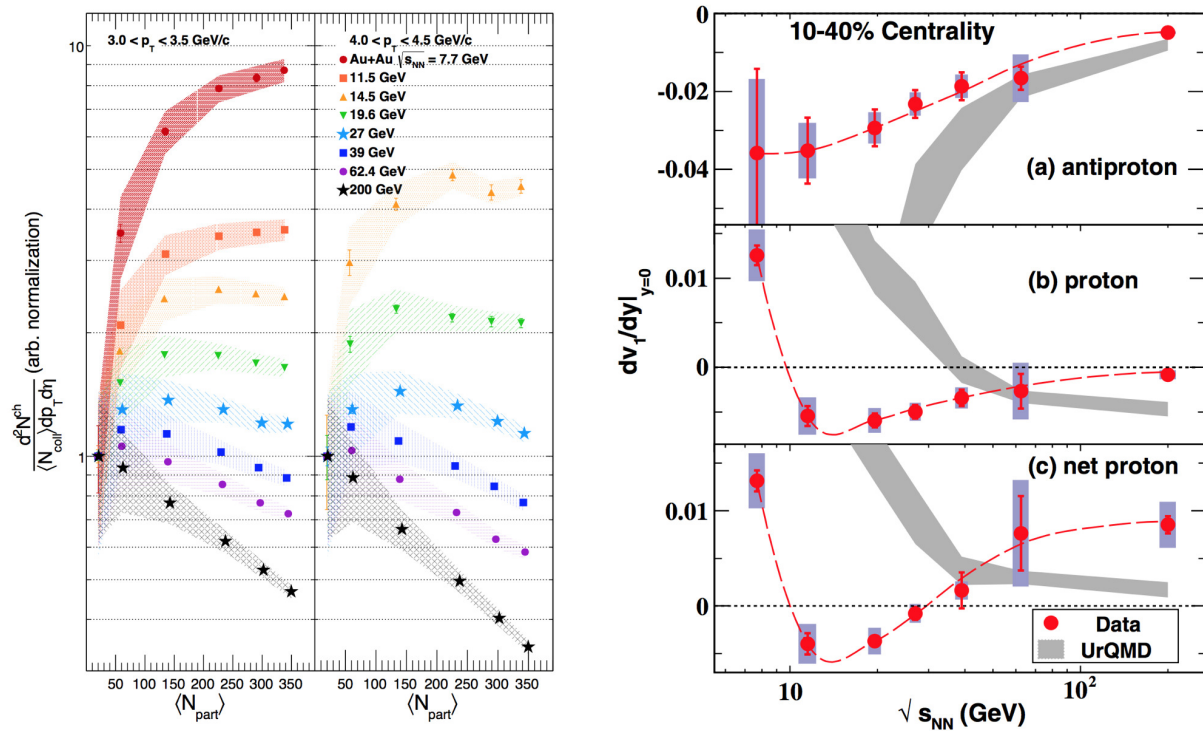


Figure 1.5: (Left) The charged hadron yields normalized by number of binary collisions as a function of the number of participant nucleons at $3.0 < p_T < 3.5$ GeV/c and $4.0 < p_T < 4.5$ GeV/c in BES energies [6]. (Right) The slope parameter of the directed flow at midrapidity $dv_1/dy|_{y=0}$ for proton, antiproton and netproton as a function of beam energy [7].

1.2.6 Critical end point

One of the most important results for the last ten years is the higher order fluctuation of conserved quantities, which provides us some possible signals for the location of the QCD critical point. It has been suggested that the measurements of higher order cumulants or moments (see Sec. 1.3) for the event-by-event net-charge, net-baryon and net-strangeness multiplicity distributions as a function of beam energy would show a non-monotonic behaviour with respect to the statistical baseline, if the trajectory of the system created in heavy ion collisions pass through near the critical point [32]. Figure 1.6 shows the published results of $\sigma^2/M = C_2/C_1$, $S\sigma = C_3/C_2$ and $\kappa\sigma^2 = C_4/C_2$ as a function of beam energy for net-charge, net-proton and net-kaon multiplicity distributions at the STAR experiment [8–10]. Net-proton and net-kaon are proxies for net-baryon and net-strangeness, respectively. Results of net-charge and net-kaon distributions show mostly monotonic behaviour with respect to the statistical baseline, while a non-monotonic kink is observed at $\sqrt{s_{NN}} = 19.6$ GeV for net-proton. More detailed studies on the net-proton fluctuations has been carried out [11], in which the non-monotonic behaviour of $\kappa\sigma^2 = C_4/C_2$ is observed as shown in Fig. 1.7 by extending the p_T coverage from $0.4 < p_T < 0.8$ GeV/c to $0.4 < p_T < 2.0$ GeV/c. Since this non-monotonic behaviour

is qualitatively consistent with the model calculation [12], it is considered as a possible signal from the QCD critical point. However, there are still large statistical errors in the low beam energy region. More statistics is required in order to derive more definite physics messages, which would be a main goal of the Beam Energy Scan Phase II starting from 2019.

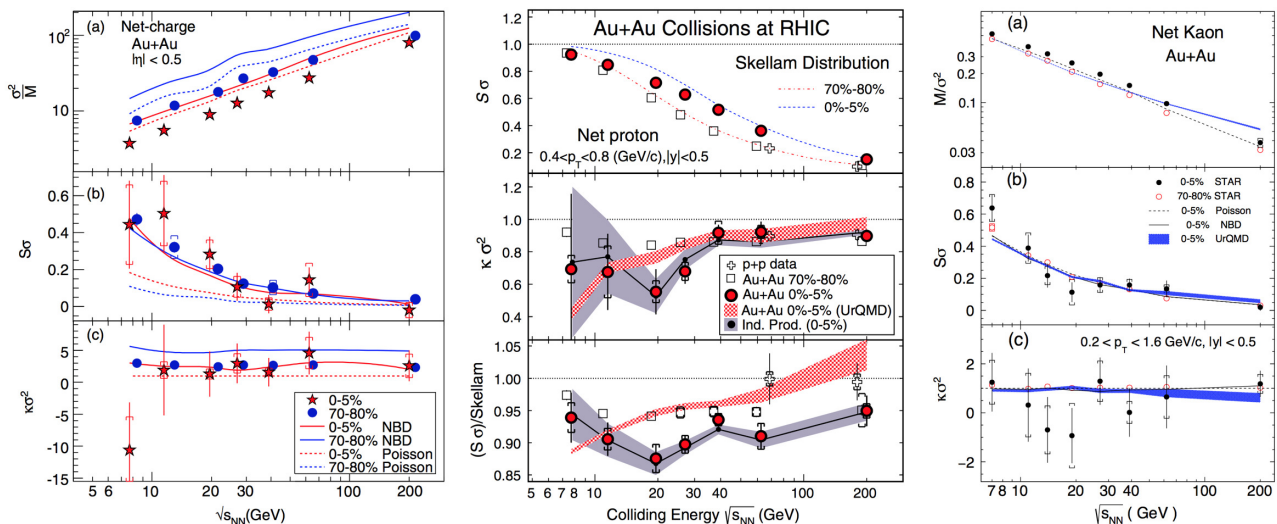


Figure 1.6: Published results of the ratio of higher order cumulants up to fourth order as a function of beam energy for net-charge (left), net-proton (middle) and net-kaon (right) multiplicity distributions [8–10].

1.2.7 Physics motivation – search for the crossover

The phase transition at vanishing baryon chemical potential can be calculated by using the lattice QCD, which has shown that the the phase transition is a smooth crossover without a clear boundary [26]. Figure. 1.8 shows the energy density computed by lattice QCD as a function of temperature [13]. It can be found that the energy density increases rapidly but smoothly starting from $T \approx 150$ MeV. However, there is no experimental evidence for this smooth crossover, because all observables would not show any discontinuity for the crossover. Theoretically, the model calculation predicts the sixth order cumulant for net-charge and net-baryon multiplicity distributions would become negative in $\sqrt{s_{NN}} \geq 60$ GeV. The left hand side panel in Fig. 1.9 shows the ratio of the sixth to second order baryon number susceptibility (χ_6^B/χ_2^B) as a function of the temperature for vanishing and finite density $\mu_q/T = 0, 0.14$ and 0.44 . For all the cases, we see the negative value of χ_6^B/χ_2^B near the chiral crossover region $0.9 < T/T_{pc} \approx 1.0$ and more than unity in $T/T_{pc} < 0.9$. The right hand side panel in Fig. 1.9 shows the expected values of χ_4^B/χ_2^B and χ_6^B/χ_2^B with different freeze-out conditions [14]. As discussed in SubSec. 1.2.3, the crossover region might be close enough to the chemical freeze-out line. Thus, the physics motivation of this study is to find the signal for the crossover phase transition by the measurement of C_6/C_2 for the net-proton multiplicity distribution as a function of centrality at $\sqrt{s_{NN}} = 200$ GeV. When considering the negative value of C_6/C_2 at the phase transition region, having more than unity for C_6/C_2 would provide us another scenario of the crossover region located far away from the chemical freeze-out line.

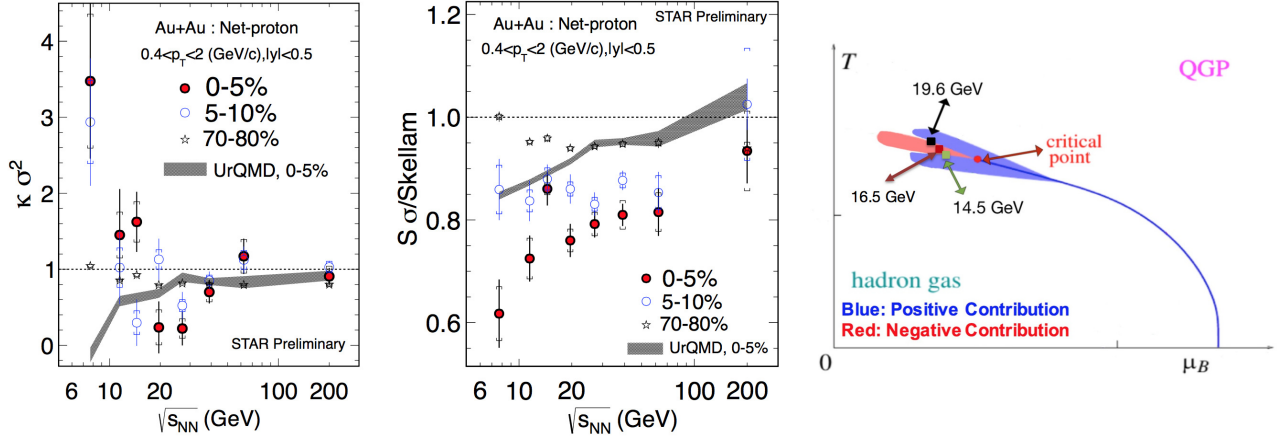


Figure 1.7: Recent STAR preliminary results on $\kappa\sigma^2$ (left) and $S\sigma$ (middle) for net-proton multiplicity distributions measured at $0.4 < p_T < 2.0$ (GeV/c) as a function of beam energy [11]. The theoretical prediction is also shown in the right hand side panel [12].

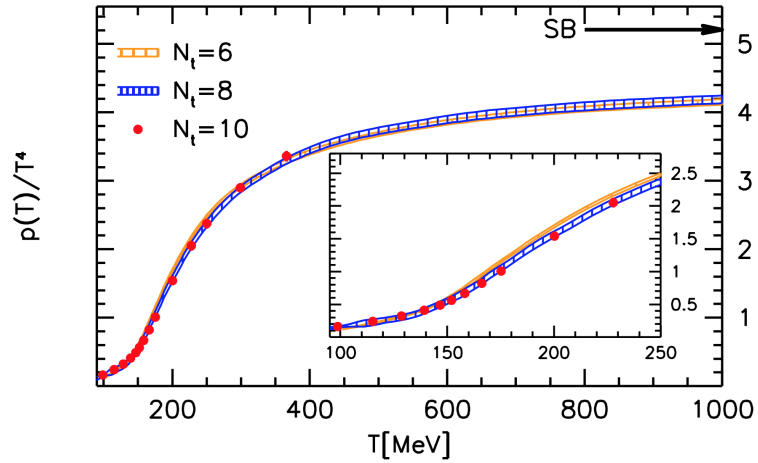


Figure 1.8: The energy density computed by lattice QCD as a function of the temperature [13].

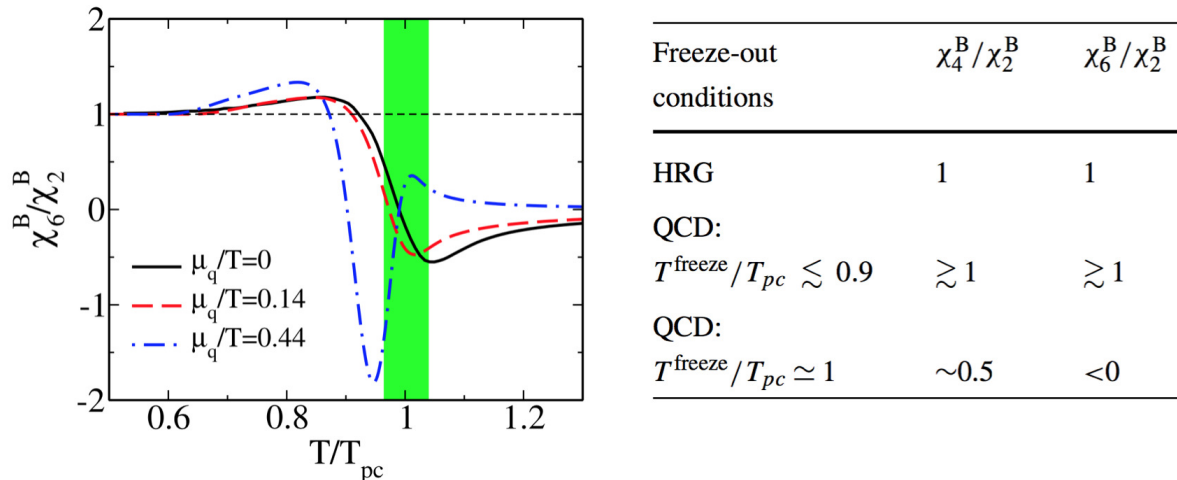


Figure 1.9: (Left) The ratio of the sixth to second order baryon number susceptibility (χ_6^B/χ_2^B) as a function of temperature for vanishing and finite density μ_q/T . The green shaded area represents the chiral crossover region. (Right) The expected values of χ_4^B/χ_2^B and χ_6^B/χ_2^B with different freeze-out conditions [14].

1.2.8 Technical motivation – investigate the analysis methods

The experimental measurement of higher order fluctuations of conserved quantities has a relatively short history. The first publication up to the fourth order cumulants was carried out in year 2010 from the STAR experiment without the efficiency correction (see Sec. 3.1). The second publication from STAR was done in 2014 with the efficiency correction to correct the finite detector efficiency. The Centrality Bin Width Correction (see Sec. 4.1) was applied in order to correct for a possible volume fluctuation in both publications. There were no other experimental groups until the HADES experiment presented the results up to the fourth order cumulants for the net-proton distribution in QM2017. In HADES preliminary results, their analysis methods were quite different from those in STAR. They tried unfolding technique to correct the detector effects including efficiency. In addition, they used another method (see Sec. 4.2) to correct the volume fluctuation instead of the Centrality Bin Width Correction. In this way, developments for the analysis technique on higher order fluctuations have been carried out by various people/groups/experiments. In other words, however, there are still no established ways to correct these effects. Furthermore, it is expected that the sixth order fluctuation are much more affected by these effects than the fourth order fluctuation, since the higher order cumulant consists of all the lower order cumulants or moments as will be seen in Eqs. (1.8)–(1.20). In order to accomplish the physics motivation mentioned above, the technical development is thus essential. Therefore, the existing and newly developed analysis methods have been investigated by applying to several models and the experimental data in order to extract more definite physics messages and to look for some scenarios including the signal from the phase transition.

1.3 Moments and cumulants

1.3.1 Definitions

Moments and cumulants are mathematical measures which represent the shape of the distribution. r th order moment μ_r are defined as:

$$\mu_r = \langle m^r \rangle = \frac{d^r}{d\theta^r} G(\theta) \Big|_{\theta=0}, \quad (1.4)$$

$$G(\theta) = \sum_m e^{m\theta} P(m) = \langle e^{m\theta} \rangle, \quad (1.5)$$

where $P(n)$ denotes a probability distribution function satisfying $\sum_n P(n) = 1$, $G(\theta)$ is a moment generating function, and a bracket represents the average over many events. Similarly, r th order cumulant C_r is given by

$$C_r = \langle m^r \rangle_c = \frac{d^r}{d\theta^r} K(\theta) \Big|_{\theta=0}, \quad (1.6)$$

$$K(\theta) = \ln G(\theta), \quad (1.7)$$

where $K(\theta)$ denotes a cumulant generating function. As is seen in Eqs. (1.4)–(1.7), moments and cumulants are connected each other via generating functions. Thus moments are expressed in terms of cumulants as

$$\mu_1 = C_1, \quad (1.8)$$

$$\mu_2 = C_2 + C_1^2, \quad (1.9)$$

$$\mu_3 = C_3 + 3C_2C_1 + C_1^3, \quad (1.10)$$

$$\mu_4 = C_4 + 4C_3C_1 + 3C_2^2 + 6C_2C_1^2 + C_1^4, \quad (1.11)$$

$$\mu_5 = C_5 + 5C_4C_1 + 10C_3C_2 + 10C_3C_1^2 + 15C_2^2C_1 + 10C_2C_1^3 + C_1^5, \quad (1.12)$$

$$\begin{aligned} \mu_6 = & C_6 + 6C_5C_1 + 15C_4C_2 + 15C_4C_1^2 + 10C_3^2 + 60C_3C_2C_1 + 20C_3C_1^3 \\ & + 15C_2^3 + 45C_2^2C_1^2 + 15C_2C_1^4 + C_1^6, \end{aligned} \quad (1.13)$$

and vice versa,

$$C_1 = \mu_1, \quad (1.14)$$

$$C_2 = \mu_2 - \mu_1^2, \quad (1.15)$$

$$C_3 = \mu_3 - 3\mu_2\mu_1 + 2\mu_1^3, \quad (1.16)$$

$$C_4 = \mu_4 - 4\mu_3\mu_1 - 3\mu_2^2 + 12\mu_2\mu_1^2 - 6\mu_1^4, \quad (1.17)$$

$$C_5 = \mu_5 - 5\mu_4\mu_1 - 10\mu_3\mu_2 + 20\mu_3\mu_1^2 + 30\mu_2^2\mu_1 - 60\mu_2\mu_1^3 + 24\mu_1^5, \quad (1.18)$$

$$\begin{aligned} C_6 = & \mu_6 - 6\mu_5\mu_1 - 15\mu_4\mu_2 + 30\mu_4\mu_1^2 - 10\mu_3^2 + 120\mu_3\mu_2\mu_1 - 120\mu_3\mu_1^3 \\ & + 30\mu_2^3 - 270\mu_2^2\mu_1^2 + 360\mu_2\mu_1^4 - 120\mu_1^6. \end{aligned} \quad (1.19)$$

Due to the complicated expression in higher order moments and cumulants, it is convenient to use the following recursion formula to implement the calculation:

$$C_r = \mu_r - \sum_{n=1}^{r-1} \binom{r-1}{n-1} C_n \mu_{r-n}, \quad (1.20)$$

where we can calculate r th order cumulant automatically by taking appropriate combinations for up to $r - 1$ th order moments.

Generally, moments shown in Eqs. (1.5) and (1.8)–(1.13) are called non-central moments. This is often compared to central moments. The r th order central moment μ'_r are defined as the parameters with respect to the mean value, which is given by

$$\mu'_r = \langle \delta m^r \rangle, \quad \delta m = m - \langle m \rangle, \quad (1.21)$$

where $\mu'_1 = 0$ by definition. Central moments are used for intuitive understanding of the shape of the distribution. The second order central moments is called standard deviation σ , the third order moment is the skewness S , and the four order moment is kurtosis κ . The standard deviation represents the width of the distribution. The skewness and the kurtosis represent the asymmetry and the sharpness of the distribution, respectively. The positive or negative value of the skewness and the kurtosis is illustrated in Fig. 1.10. The positive skewness gives the asymmetric shape leaned to the right hand side with respect to the mean position of the distribution, whereas the shape becomes left hand side leaned shape for the positive skewness. For the positive kurtosis, the center of the distribution becomes sharper and the tail becomes wider. The negative kurtosis provides the box-like shape.

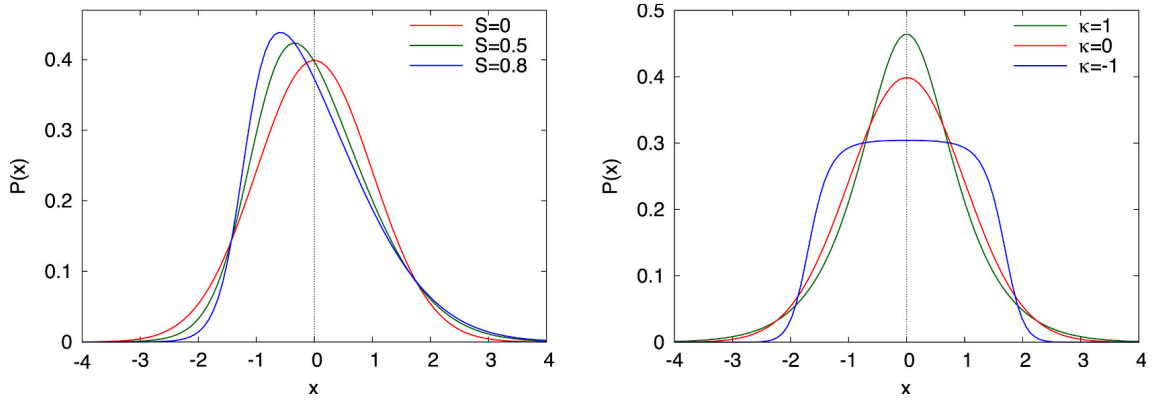


Figure 1.10: An example of skewness and kurtosis [15].

1.3.2 Additivity of cumulants

Although cumulants and moments are compatible measures each other, cumulants are more easy to handle due to their additivity [15]. Let us consider two independent probability distribution functions $P_1(m_1)$ and $P_2(m_2)$, where m_1 and m_2 are stochastic variables. Probability distribution function of $m = m_1 + m_2$ are then given by

$$P(m) = \sum_{m_1, m_2} \delta_{m, m_1 + m_2} P_1(m_1) P_2(m_2). \quad (1.22)$$

Moment and cumulant generating functions for $P(m)$ are calculated as follows:

$$\begin{aligned} G(\theta) &= \sum_m e^{m\theta} P(m) = \sum_m e^{m\theta} \sum_{m_1, m_2} \delta_{m, m_1 + m_2} P_1(m_1) P_2(m_2) \\ &= \sum_{m_1} e^{m_1\theta} P_1(m_1) \sum_{m_2} e^{m_2\theta} P_2(m_2) = G_1(\theta) G_2(\theta), \end{aligned} \quad (1.23)$$

$$K(\theta) = \ln G(\theta) = K_1(\theta) + K_2(\theta). \quad (1.24)$$

By taking r derivatives on Eq. (1.24), r -th order cumulant can be expressed as

$$\langle m^r \rangle_c = \langle m_1^r \rangle_c + \langle m_2^r \rangle_c, \quad (1.25)$$

which indicates that any order of cumulant for the probability distribution functions for sum of two independent stochastic variables are given by the sum of cumulants for probability distribution function for each variable. On the other hand, moments are obtained by

$$\langle m \rangle = \langle m_1 \rangle + \langle m_2 \rangle, \quad (1.26)$$

$$\langle m^2 \rangle = \langle m_1^2 \rangle + \langle m_2^2 \rangle + 2\langle m_1 \rangle \langle m_2 \rangle, \quad (1.27)$$

$$\langle m^3 \rangle = \langle m_1^3 \rangle + \langle m_2^3 \rangle + 3\langle m_1^2 \rangle \langle m_2 \rangle + 3\langle m_1 \rangle \langle m_2^2 \rangle, \quad (1.28)$$

where correlation terms of moments between two probability distribution functions for each stochastic variables appear. This is the reason why cumulants are preferred to moments for various usages. Note that this "additivity" of cumulants is only valid in the case of independent stochastic variables.

1.3.3 Factorial moments and factorial cumulants

For the efficiency correction discussed in Secs. 3.1.1 and 3.1.2, let us introduce factorial moments and factorial cumulants that can also characterize probability distribution functions [15]. The n th order factorial moment are defined as

$$\langle m^n \rangle_f = \langle m(m-1)\dots(m-n+1) \rangle = \frac{d^n}{ds^n} G_f(s) \Big|_{s=1}, \quad (1.29)$$

$$G_f(s) = \sum_m s^m P(m) = G(\ln s), \quad (1.30)$$

where $G_f(s)$ denotes the factorial moment generating function. Similarly, the n th order factorial cumulant is given by

$$\langle m^n \rangle_{fc} = \frac{d^n}{ds^n} K_f(s), \quad (1.31)$$

$$K_f(s) = \ln G_f(s) = K(\ln s), \quad (1.32)$$

where $K_f(s)$ denotes a factorial cumulant generating function. For the convenience, the expression for the factorial moments of net-particle distribution can be introduced by:

$$F_{ab} = \sum_{m=a}^{\infty} \sum_{\bar{m}=b}^{\infty} P(m, \bar{m}) \frac{m!}{(m-a)!} \frac{\bar{m}!}{(\bar{m}-b)!}, \quad (1.33)$$

where m and \bar{m} are number of positively and negatively charged particles.

1.3.4 Cumulants of conserved quantities

The cumulants of conserved quantities in quantum statistical mechanics are considered. The grand partition function for conserved quantity N is defined as

$$Z = \text{tr}[e^{-(H-\mu N)/T}], \quad (1.34)$$

where H is Hamiltonian, V is volume, T is temperature, and μ is chemical potential. Cumulants of N are given by derivatives of the grand potential $\Omega = -T \ln Z$ with respect to μ/T :

$$\langle N^n \rangle_c = \frac{\partial^n (-\omega/T)V}{\partial (\mu/T)^n} \equiv \chi_n V, \quad (1.35)$$

$$\Omega = \omega V \quad (1.36)$$

where the grand potential per unit volume is defined as ω , and χ_n is defined as susceptibility. Experimentally, the cumulants $\langle N \rangle_c$ can be calculated by looking at the event-by-event multiplicity distribution for conserved quantities, e.g., net-charge, net-baryon and net-strangeness distributions. Theoretically, susceptibilities can be computed by LQCD calculation. By taking ratio of different order of cumulants, the volume V can be canceled, thus, experimental and theoretical results can be directly compared.

1.3.5 Statistical baseline

Binomial distribution

The binomial distribution is defined by the number of success in a sequence of N independent trials with the success probability of p , which is given by

$$B_{p,N}(m) = \frac{N!}{m!(N-m)!} p^m (1-p)^{N-m}. \quad (1.37)$$

This is equal to the case that we measure the number of particles m with probability p in certain volume with respect to the total number of N particles in the whole volume. The generating functions are thus obtained as

$$\begin{aligned} G_B(\theta) &= \sum_m e^{m\theta} B_{p,N}(m) = \sum_m \frac{N!}{m!(N-m)!} (e^\theta p)^m (1-p)^{N-m} \\ &= (1-p + e^\theta p)^N, \end{aligned} \quad (1.38)$$

$$K_B(\theta) = N \ln(1-p + e^\theta p). \quad (1.39)$$

By taking derivatives on the cumulant generating function, cumulants up to sixth order are given by

$$\langle m^n \rangle_c = \xi_n N, \quad (1.40)$$

with

$$\xi_1 = p, \quad (1.41)$$

$$\xi_2 = p(1-p), \quad (1.42)$$

$$\xi_3 = p(1-p)(1-2p), \quad (1.43)$$

$$\xi_4 = p(1-p)(1-6p+6p^2), \quad (1.44)$$

$$\xi_5 = p(1-p)(1-2p)(1-12p+12p^2), \quad (1.45)$$

$$\xi_6 = p(1-p)(1-30p+150p^2-240p^3+120p^4). \quad (1.46)$$

Now one can consider the binomial baseline for the net-proton distribution by assuming protons and antiprotons follow the binomial distributions. The measured mean μ and the scaled variance $\sigma^2 \mu$ for the distribution of proton and antiproton are written by

$$\mu = Np, \quad \varepsilon = \frac{\sigma^2}{\mu} = 1-p, \quad (1.47)$$

Cumulants up to fourth order can be expressed by using μ and ε :

$$\langle m \rangle_c = \mu, \quad (1.48)$$

$$\langle m^2 \rangle_c = \mu\varepsilon, \quad (1.49)$$

$$\langle m^3 \rangle_c = \mu\varepsilon(2\varepsilon - 1), \quad (1.50)$$

$$\langle m^4 \rangle_c = \mu\varepsilon(6\varepsilon^2 - 6\varepsilon + 1), \quad (1.51)$$

$$\langle m^5 \rangle_c = \mu\varepsilon^2(2\varepsilon - 1)(12\varepsilon^2 - 12\varepsilon + 1), \quad (1.52)$$

$$\langle m^6 \rangle_c = \mu\varepsilon(120\varepsilon^4 - 240\varepsilon^3 + 150\varepsilon^2 - 30\varepsilon + 1). \quad (1.53)$$

Then the r th order cumulant of the net-proton distribution is given by

$$C_r^{met} = C_r^p + (-1)^r C_r^{\bar{p}}. \quad (1.54)$$

In the experiment, measured C_1 and C_2 for the (anti)proton distribution allow us to calculate Eqs. (1.48)–(1.53), which provides the binomial baseline for the net-proton distribution as shown in Eq. (1.54).

Poisson distribution

By taking $p \rightarrow 0$ limit of the binomial distribution, one obtains the Poisson distribution:

$$P_\lambda(m) = \frac{\lambda^m}{m!} e^{-\lambda}, \quad (1.55)$$

where λ denotes the mean value of the distribution. The cumulant generating function is given by

$$K_\lambda(\theta) = \lambda(e^\theta - 1). \quad (1.56)$$

Taking derivatives on this equation provides cumulants:

$$\langle m^n \rangle_c = \lambda \quad (n \geq 1). \quad (1.57)$$

It can be found that the all orders of cumulants are identical, and they are exactly equal to the mean value λ . Next, let us consider the difference of two Poisson distributions, which corresponds to the net-proton distribution. The probability distribution function is written as

$$S_{\lambda_1, \lambda_2}(m) = \sum_{m_1, m_2} \delta_{m, m_1 - m_2} P_{\lambda_1}(m_1) P_{\lambda_2}(m_2), \quad (1.58)$$

which is known as the Skellam distribution. Then the generating functions are given by

$$\begin{aligned} G(\theta) &= \sum_m e^{m\theta} \sum_{m_1, m_2} \delta_{m, m_1 - m_2} P_{\lambda_1}(m_1) P_{\lambda_2}(m_2) \\ &= \sum_{m_1} e^{m_1\theta} P_{\lambda_1}(m_1) \sum_{m_2} e^{-m_2\theta} P_{\lambda_2}(m_2) \\ &= G_{\lambda_1}(\theta) G_{\lambda_2}(-\theta), \end{aligned} \quad (1.59)$$

$$K(\theta) = K_{\lambda_1}(\theta) + K_{\lambda_2}(-\theta). \quad (1.60)$$

By taking derivatives on the cumulant generating function, the r th order cumulant is given by

$$\langle m^r \rangle = \lambda_1 + (-1)^r \lambda_2, \quad (1.61)$$

which indicates that the odd order cumulant is equal to the difference of two means of two Poisson distributions, whereas the even order cumulant is given by the sum of them. Therefore, the Skellam baseline for cumulant ratios for the net-particle distribution are written as

$$R_{2,1} = \frac{C_2}{C_1} = \frac{\lambda_1 + \lambda_2}{\lambda_1 - \lambda_2}, \quad R_{3,2} = \frac{C_3}{C_2} = \frac{\lambda_1 - \lambda_2}{\lambda_1 + \lambda_2}, \quad R_{6,2} = R_{4,2} = 1. \quad (1.62)$$

Experimentally, the Poisson distribution expresses the probability distribution to measure the number of particle m in a substantially small volume. If one decreases the acceptance smaller and smaller to the limit for measuring protons and antiprotons, the cumulants should become close to the values of the Poisson distribution. In this case, there will be no chance to be sensitive to the fluctuation arising from the possible critical point or phase transition. Keeping the acceptance as large as possible is thus important in the fluctuation analysis, and comparing the measured fluctuations with respect to the Skellam baseline would provide us some information on whether the observed signal is anything more than the statistical fluctuation or not.

Chapter 2

Experiment

2.1 Relativistic Heavy Ion Collider (RHIC)

Search for the QGP started from the late 80's in AGS and SPS accelerator in BNL and CERN by colliding heavy ions to the fixed target. Although some signs of hot and dense matter were observed at the SPS top energy of $\sqrt{s_{NN}} = 17$ GeV, it was not a definitive evidence. Relativistic Heavy Ion Collider (RHIC) is the world's first heavy ion collider starting from the year of 2000. Figure 2.1 shows an aerial photo of RHIC. RHIC consists of two concentric rings called "blue ring" and "yellow ring" with circumferential length of 3.8 km, made up of 1,740 superconducting magnets. Two rings intersect at six points, where different detectors were located at four of the intersection points, STAR, PHENIX, BRAHMS and PHOBOS. BRAHMS and PHOBOS completed their operations about ten years ago, and PHENIX is being dismantled since last year. STAR is the only experiment running in RHIC. At RHIC, various kinds of beam ion species can be accelerated, from the light nuclei such as deuteron and He^3 to the heavy ions like Cu, Au and U. The highest beam energy is $\sqrt{s_{NN}} = 510$ GeV in p+p collisions and $\sqrt{s_{NN}} = 200$ GeV in Au+Au collisions.

2.2 The STAR detector

The Solenoid Tracker At RHIC (STAR) is the detector located at the 6 o'clock in RHIC. Figure 2.2 shows an overview of the STAR detectors. STAR has large and uniform acceptance in midrapidity, which covers the pseudorapidity of $-1.8 < \eta < 1.8$ and full azimuthal angles, with excellent particle identification capability. As is seen in the name of STAR, the main tracker is Time Projection Chamber (TPC) which enables us three-dimensional tracking of produced charged particles. Due the large amount of particles produced in heavy ion collisions, lots of information are lost once the particle tracking is profiled into two-dimensional plane. Thus, the three-dimensional tracking achieved by TPC is one of the important features in the heavy ion colliding experiment. The Time Of Flight (TOF) detectors are located outside the TPC. TOF measures the timing when particles pass through the detector with less than 100 ps resolution, which enables us the particle identification at the intermediate momentum region. The Barrel Electro-Magnetic Calorimeter (BEMC) are located radially further outside of TOF, which covers $|\eta| < 1.0$ with full azimuthal angles. BEMC is used to trigger high momentum photons and electrons. The Endcap Electro-Magnetic Calorimeter (EEMC) of the same system with BEMC is located at the forward rapidity $1.0 < \eta < 2.0$ with the full azimuthal angles as well. The Beam Beam Counter (BBC) sits in 3.5 m away from the collision point covering $3.3 < |\eta| < 5.0$. The BBC consists of two rings of hexagonal scintillator tiles. It is used to measure relative luminosity for polarized p+p collisions. The Zero Degree Calorimeter (ZDC) is placed 18 m away from

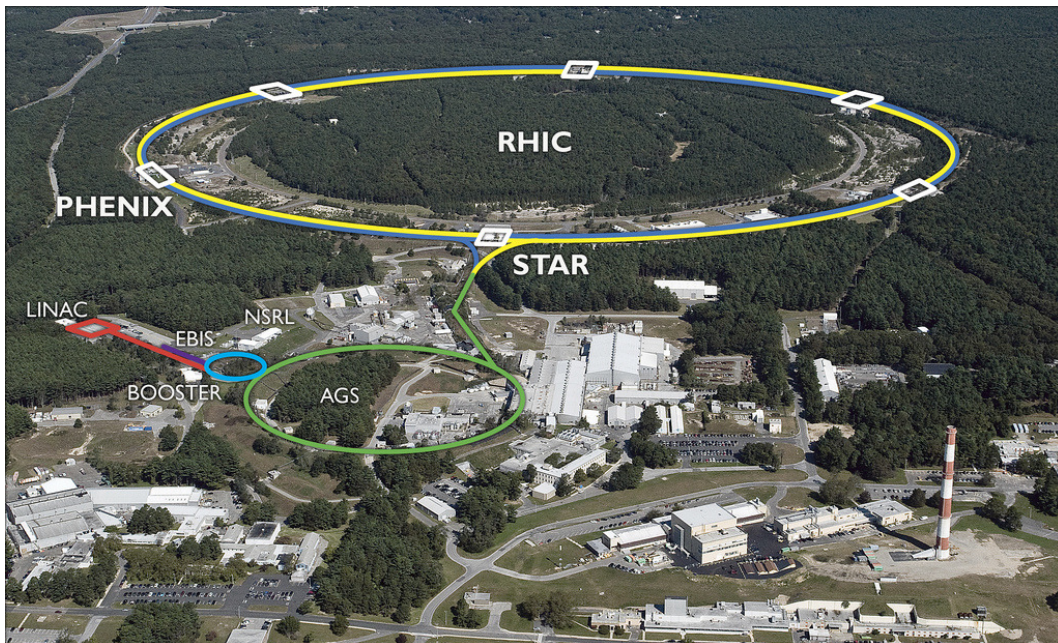


Figure 2.1: An aerial photo of RHIC.

the center of TPC, downstream of the dipole magnets, covering < 2.5 mrad in the polar angle. The ZDC is the hadronic calorimeter. It measures the energy of the spectator nucleons. The coincidence signals from detectors on either side of the interaction region are used for luminosity monitoring. The Vertex Position Detector (VPD) is used to provide minimum-bias trigger in Au+Au collisions, to measure the location of primary vertex along the beam pipe, and to determine the start time for TOF.

From the next subsection, details for TPC, TOF and VPD, mainly used for fluctuation measurements, will be explained.

2.2.1 Time Projection Chamber (TPC)

TPC is the primary tracking device in STAR, which performs tracking of charge particles to obtain momenta and to identify particles by measuring the ionization energy loss in the gas volume. Momenta are measured from 100 MeV/c up to 30 GeV/c. The schematic of TPC is shown in Fig. 2.3. The TPC is 4.2 m long and 4 m in diameter, and it is located inside a solenoidal magnets with 0.5 T. The TPC is filled with P10 gas (10% methane, 90% argon) regulated at 2 mbar above atmospheric pressure, where the uniform electric field is applied ≈ 135 V/cm by Central Membrane, field-cage cylinders and the readout end caps.

The readout system is based on Multi-Wire Proportional Chamber (MWPC). Once drifting electrons reach the anode wires, avalanche occurs with the amplification gain of 1000–3000. Then image charge is induced by moving the large amount of positively charged ions. Anode wires are located with 4 mm spacing, and the position resolution is thus limited by the spacing in this direction. The direction of anode wires are set to be perpendicular to the tracks with the highest transverse momentum. Momentum resolution of charged particles gets worse with increasing p_T since the radius of the curvature of the track becomes large. As MWPC has the best position resolution in the wire direction, better position resolution for higher p_T charged particles can be achieved by setting the

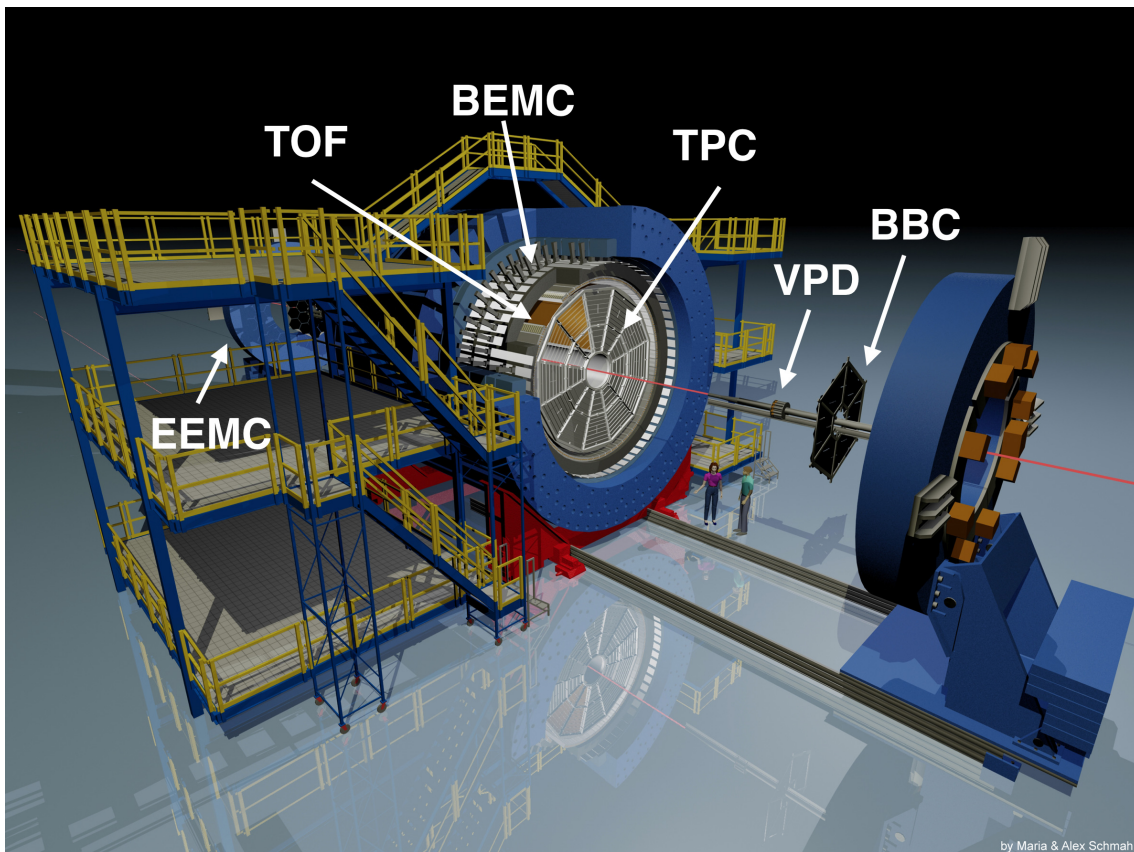


Figure 2.2: Overview of the STAR detector

anode wire direction roughly perpendicular to the straight tracks. Figure 2.4 shows a schematic on the anode pad plane of one full sector. For the outer radius subsectors, readout pads are occupied with no space between pad rows in order to optimize the dE/dx resolution. By collecting more signals from the ionization electrons, statistics on the dE/dx measurement can be improved. For the inner radius subsectors, smaller pad size is required due to the high track density. This is important for charged particles with lower momentum passing across the pad rows far from perpendicular. Compromising with the limited number of readout electronics, separated pad rows are used for the inner radius subsectors instead of the continuous pad coverage.

The x and y position of electron clusters are determined by the induced signals in a single pad row. The signals are induced only on three pads for typical tracks. By assuming that the signals are distributed with Gaussian, x position and its width with pad h_2 centered at $y = 0$ is given by

$$x = \frac{\sigma^2}{2w} \ln\left(\frac{h_3}{h_1}\right), \quad \sigma^2 = \frac{w^2}{\ln(h_2^2/h_1 h_3)}, \quad (2.1)$$

where h_1 , h_2 and h_3 are amplitudes on three pads and w is the pad width. This algorithm gets worse in the case of the large crossing angles, when any three adjacent pads have comparable amplitude of signals. Thus the weighted mean algorithm is also used as well. The z position of the track is determined by measuring the time of secondary electrons reaching the anode wire to induce signals. The z position is calculated by dividing the time by the drift velocity of electrons. This indicates that the reconstruction of z position strongly depends on the drift velocity, and it can change by the small change of the gas composition and the atmospheric pressure. In order to consider these effects, the drift velocity is measured every few hours by artificial tracks created using the reference laser beams.

The main purposes of TPC is the vertex reconstruction, the measurement of momentum and the identification of particles. The vertex resolution in the transverse plane is improved by the square root of the number of tracks used in the vertex reconstruction. A resolution is achieved to be about $350 \mu m$ with more than 1000 tracks. The momentum resolution is estimated by the embedding simulation, where the simulated tracks from Geant are embedded in the real event and the tracking is performed. Looking at the difference between true and reconstructed momentum of embedded tracks provides the relative momentum resolution. The best momentum resolution for pions is 2 % at $p_T \approx 400 \text{ MeV}/c$, and 3 % for antiprotons at $p_T \approx 800 \text{ MeV}/c$. The energy loss of charged particles in TPC gas volume are calculated by summing up the induced charged on the readout pads. After considering the change of the gas gain and the uncertainties arising from electronics, the dE/dx is extracted from the energy loss measured at up to 45 pad rows. Figure 2.5 shows the energy loss as a function of momentum. The magnetic field is set to be 0.25 T. It can be found that the pions and protons are separated up to $p \approx 1 \text{ GeV}/c$.

2.2.2 Time Of Flight (TOF)

As is seen in Fig. 2.5, the particle identification between pion and proton with TPC is limited in $p \leq 1 \text{ GeV}/c$. The particle identification at the intermediate momentum region more than $p \approx 1 \text{ GeV}/c$ can be achieved by using additional information from Time Of Flight (TOF) detectors. TOF measures the time when charged particles pass through with good resolution. As the distance L between the collision point and the TOF is known, the mass is given by

$$m^2 = p^2 \left[\left(\frac{t}{L} \right)^2 - 1 \right], \quad (2.2)$$

where t is the time difference between the start and stop time. The stop time is given by TOF, and the start time is measured by VPD (will be discussed in the next subsection). Figure 2.6 shows the

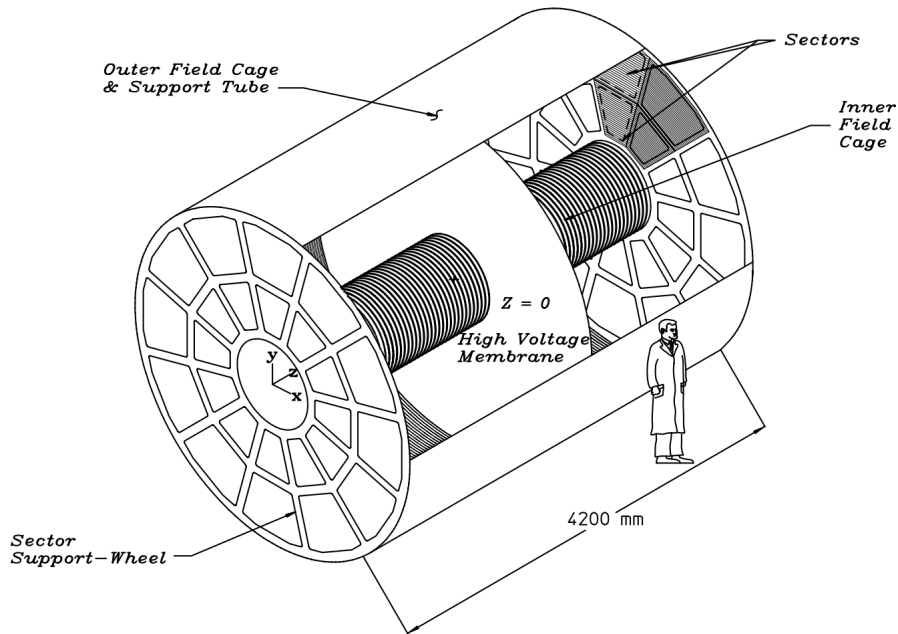


Figure 2.3: A schematic of the STAR TPC [16]

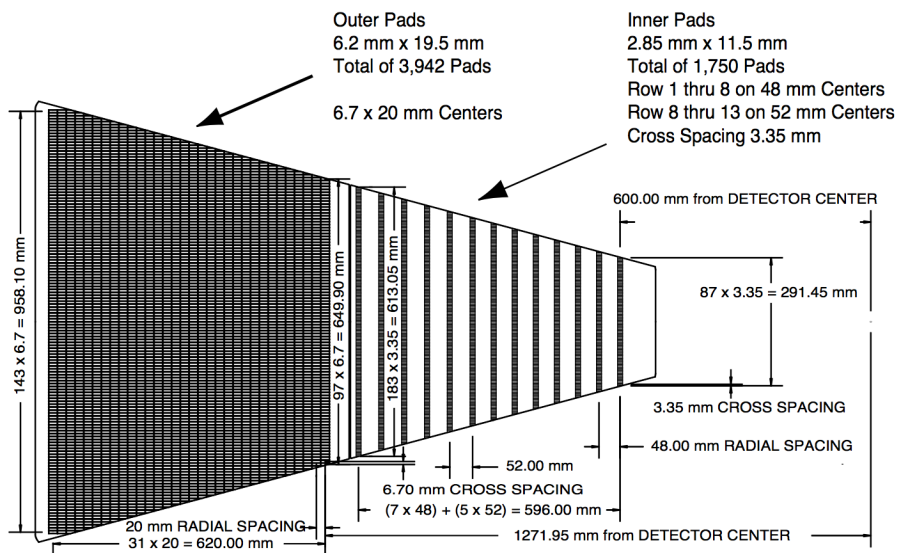


Figure 2.4: A schematic on the anode pad plane with one full sector [16].

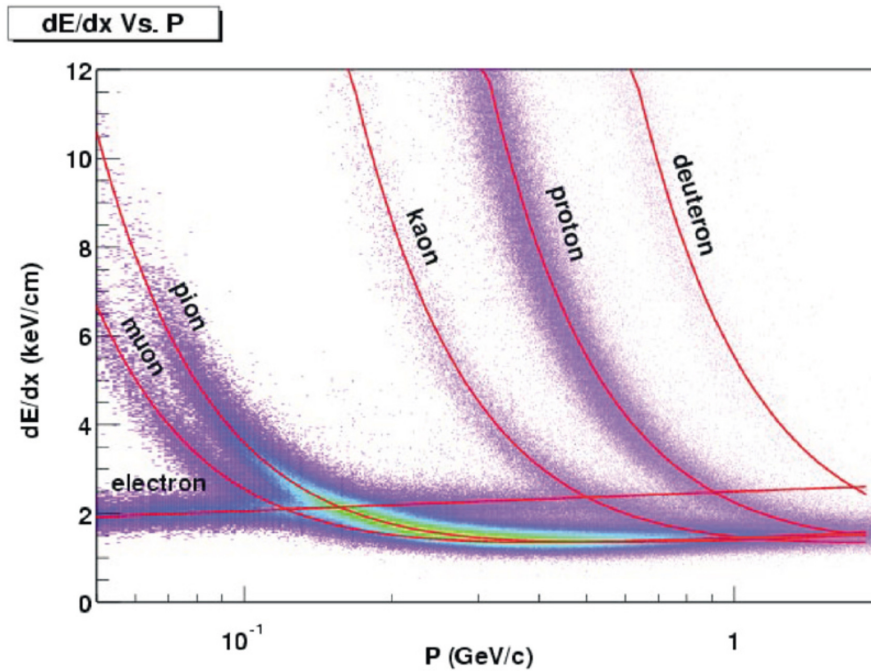


Figure 2.5: The energy loss as a function of momentum with the Bethe-Bloch expectations. The magnetic field is set to be 0.25 T [16].

inverse of $\beta = v/c$ as a function of the momentum provided by TPC. It can be found that pions, kaons, protons and deuterons are clearly separated in this momentum region, for example, proton and pion separation below 3 GeV/c.

The TOF system in STAR is based on the Multi-gap Resistive Plate Chamber (MRPC). A schematic on the side view of MRPC is shown in Fig. 2.7. Six small gas gaps of $220 \mu\text{m}$ are created with high resistive glass plates and fishing lines. They are stacked between two electrodes on which high voltages $\pm 7 \text{ kV}$ are applied. Then the high and uniform electric fields are formed in each small gas gap. Once a charged particle pass through the MRPC, gas molecules are ionized to produce secondary electrons and ions. Due to the high electric fields in a gas gap, an avalanche starts to grow up and move to the anode direction. This occurs at each gas gap but stops when an avalanche reach an adjacent glass plate. Image charges are induced on the readout pad by fast moving of avalanche electrons. Signals induced by secondary ions are negligible compared to those from electrons because they move slower than electrons due to their large mass. Independent six avalanches are produced simultaneously with respect to the incident of one charged particle, where the superposition of these independent signals would lead an improved timing resolution over the single gap case. Full installations of 120 trays for the barrel TOF system were carried out in the year 2010 with the acceptance of $|\eta| < 0.9$ and full azimuthal angles, and around 80 ps time resolution was achieved in Au+Au collisions at $\sqrt{s_{\text{NN}}} = 200 \text{ GeV}$.

2.2.3 Vertex Position Detector (VPD)

VPD measures the arrival time of tens to hundreds of photons from π^0 , and provides the information on event triggering [19]. The identical assemblies are located at both east and west sides with respect to the collision point, which corresponds to the pseudorapidity region of $4.24 \leq \eta \leq 5.1$. The primary

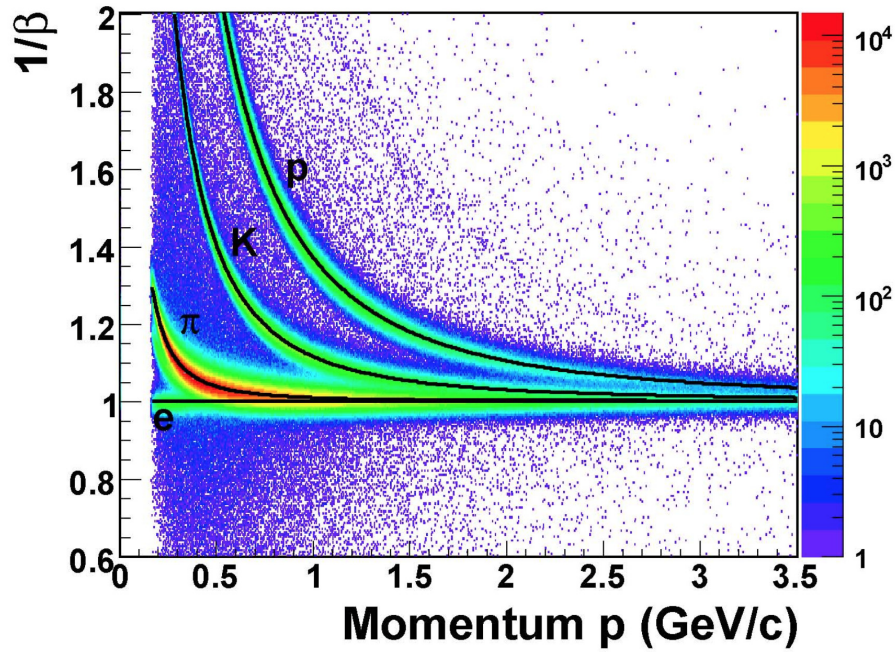


Figure 2.6: $1/\beta$ as a function of momentum, measured in Run 9 at $\sqrt{s_{NN}} = 200$ GeV in p+p collisions [17].

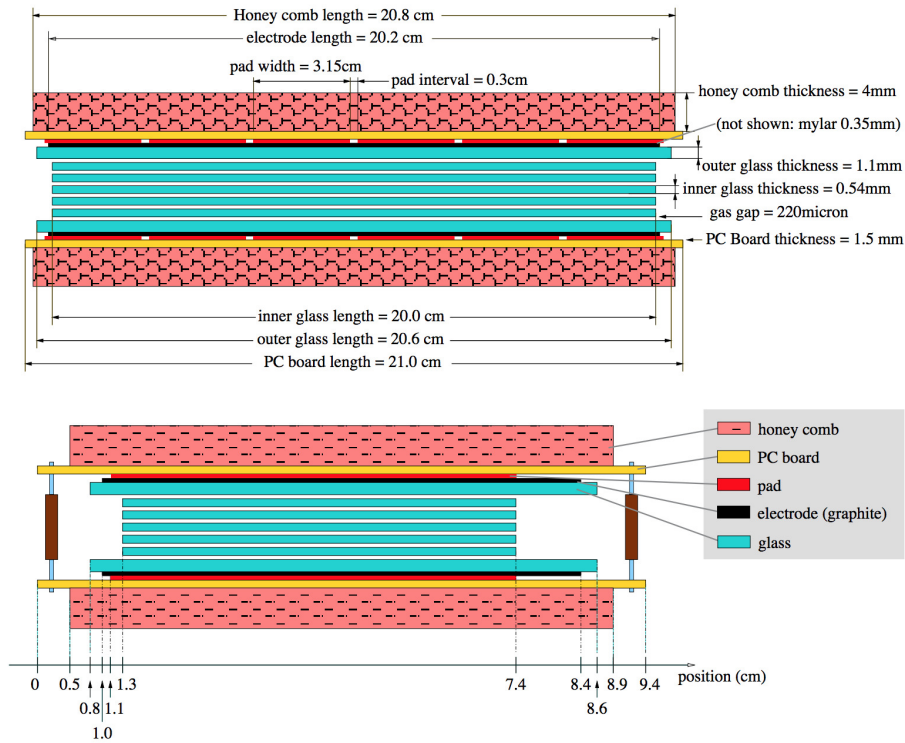


Figure 2.7: A two-side view on the MRPC detector [18].

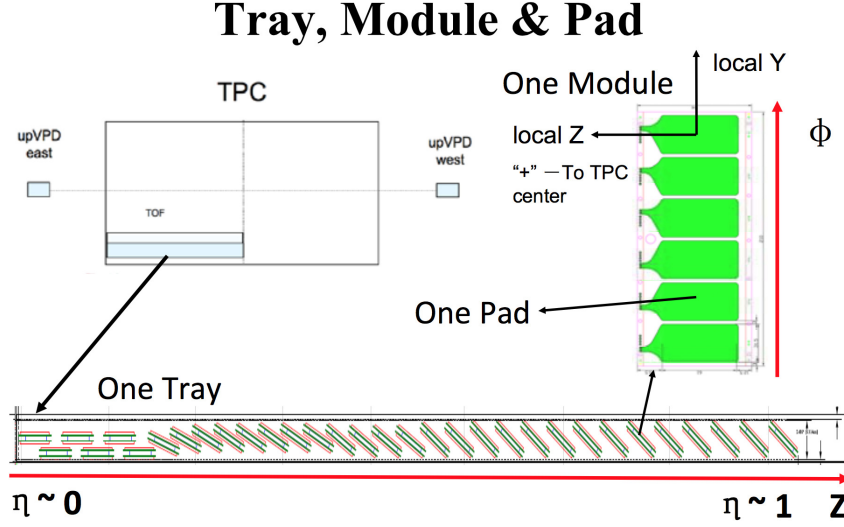


Figure 2.8: A schematic on TOF trays.

vertex position along the beam pipe, Z_{vtx} is given by

$$Z_{vtx} = c(T_{east} - T_{west})/2, \quad (2.3)$$

where the T_{east} and T_{west} are the times measured by each assembly, and c is the speed of light. By using these two times, the start time for TOF can be determined as

$$T_{start} = (T_{east} + T_{west})/2 - L/c, \quad (2.4)$$

where L is the distance between either assembly and the collision point. The front view of one assembly and a photograph of two assemblies are shown in Fig. 2.9. VPD consists of nineteen detectors made up by a scintillator and a PMT. Such well-segmented detector with nineteen readout channels provide the good time resolution by the central limit theorem, and thus leads to the better primary vertex resolution, which is given by

$$\sigma_{start} = \sigma_0/\sqrt{N}, \quad (2.5)$$

$$\sigma(Z_{vtx}) = (c/\sqrt{2})\sigma_0/\sqrt{N}, \quad (2.6)$$

where N is the number of readout channels and σ_0 represents the time resolution of a single readout detector. Figure 2.10 shows the time resolution of VPD at each readout channel with different collisions and beam energies. It can be found that the time resolution becomes better with increasing the beam energy. This is because VPD is doing multiple-particle timing, thus the time resolution gets better in higher beam energy due to larger multiplicity. By taking average of the times measured at all readout channels, the start time resolution reaches around 20 – 30 ps. The actual time resolution for single particle is the quadruple sum of the time resolution for VPD (start) and TOF (stop), thus less than 30 ps start time resolution of VPD is good enough compared to the stop time resolution of TOF about 80 ps. Figure 2.11 shows the correlation of the primary vertex position along the beam pipe measured by VPD Z_{vtx}^{VPD} and measured by TPC Z_{vtx}^{TPC} , in p+p collisions at $\sqrt{s_{NN}} = 510$ GeV recorded in 2012 (left), and in Au+Au collisions at $\sqrt{s_{NN}} = 200$ GeV recorded in 2009 (right). The insets show the difference between them $\Delta Z = Z_{vtx}^{VPD} - Z_{vtx}^{TPC}$ from which the Z_{vtx} resolution of VPD can be extracted, and it can be found that the resolutions are $\sigma(\Delta Z) = 2.3$ cm and 0.9 cm for p+p and Au+Au collisions, respectively.

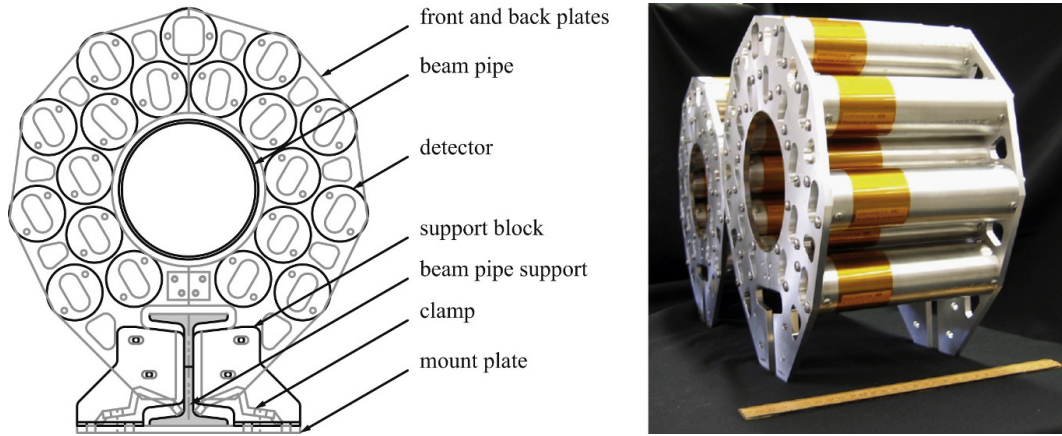


Figure 2.9: The front view of one assembly (left) and a photograph of two assemblies (right) [19].

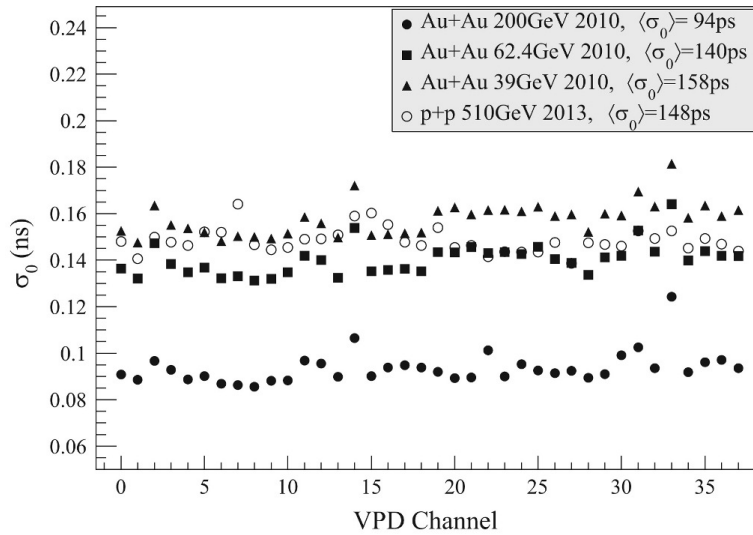


Figure 2.10: The front view of one assembly (left) and a photograph of two assemblies (right) [19].

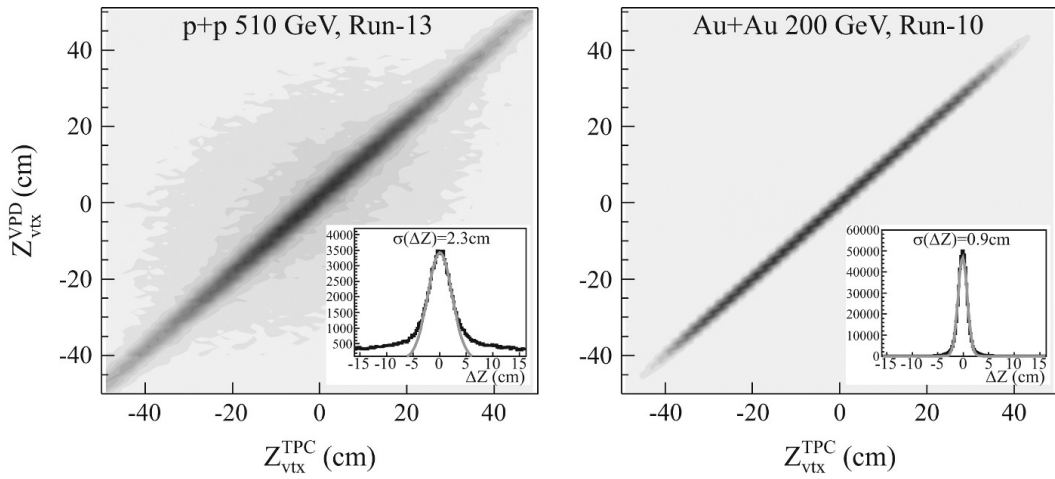


Figure 2.11: Correlation of the primary vertex position along the beam pipe measured by VPD Z_{vtx}^{VPD} and measured by TPC Z_{vtx}^{TPC} , in p+p collisions at $\sqrt{s_{NN}} = 510$ GeV recorded in 2012 (left), and in Au+Au collisions at $\sqrt{s_{NN}} = 200$ GeV recorded in 2009 (right) [19]. The insets show the difference between them $\Delta Z = Z_{vtx}^{VPD} - Z_{vtx}^{TPC}$ from which the Z_{vtx} resolution of VPD can be extracted.

2.3 Datasets

The measurements of higher order fluctuations are very statistical hungry. In order to reduce statistical errors, the datasets collected in 2010 and 2011 at $\sqrt{s_{NN}} = 200$ GeV are both analyzed independently and merged. Details for the datasets are summarized in Tab. 2.1.

Year	Trigger	Events
2010	minimum bias (10–80%)	200 M
2010	central trigger (0–10%)	160 M
2011	minimum bias (0–80%)	510 M

Table 2.1: Datasets used in the analysis.

2.3.1 Run by run QA

Figure 2.12 shows the averaged z-vertex position, radial vertex position, number of primary tracks, distance of closest approach (DCA), transverse momentum, and pseudo-rapidity as a function of run index in Run11. Outlier runs outside $\pm 3\sigma$ at each trigger condition are rejected from the analysis.

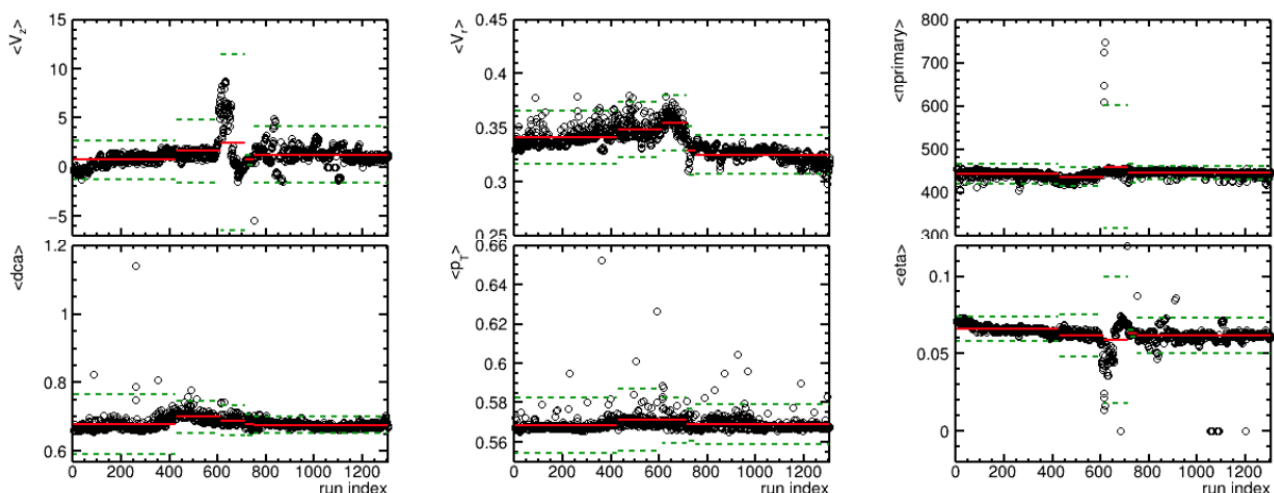


Figure 2.12: Averaged z-vertex position, radial vertex position, number of primary tracks, distance of closest approach (DCA), transverse momentum, and pseudo-rapidity as a function of run index in Run11. Mean values in the same trigger condition are shown in red solid lines, and $\pm 3\sigma$ lines are shown green.

2.3.2 Event and track selection

Event and track quality cuts are shown in Tab. 2.2, and also shown in Fig. 2.13. In order to reject pile up events, difference between z-vertex measured by TPC and VPD are limited within 3 cm. Residual pile up events are excluded from the correlation between the number of primary tracks associated with TOF and number of primary tracks in $|\eta| < 1.0$ measured by TPC (RefMult) as shown in Fig. 2.14-(a) and (c). Events including lots of wired tracks with wrong β information are rejected by looking at the correlation between the number of primary tracks associated with TOF requiring $\beta > 0.1$ and the

RefMult, which is shown in Fig 2.14-(b) and (d). Tracks associated to the primary vertex are selected with $DCA < 1.0$ cm. Primary tracks with good tracking quality are selected by requiring hit points for fitting the hit points and calculating the dE/dx .

$ V_z $	< 30 cm
V_r	< 2 cm
$ V_{pd}V_z - V_z $	< 3 cm
tofmatched	$> 0.50 \times \text{refmult} - 30$ (Run10)
tofmatchedbeta	$> 0.43 \times \text{refmult} - 15$ (Run10)
tofmatched	$> 0.50 \times \text{refmult} - 13$ (Run11)
tofmatchedbeta	$> 0.46 \times \text{refmult} - 10$ (Run11)
DCA	< 1 cm
nHitsFit	> 20
nHitsFit/nFitPoss	> 0.52
nHitsDedx	> 5

Table 2.2: Datasets used in analysis.

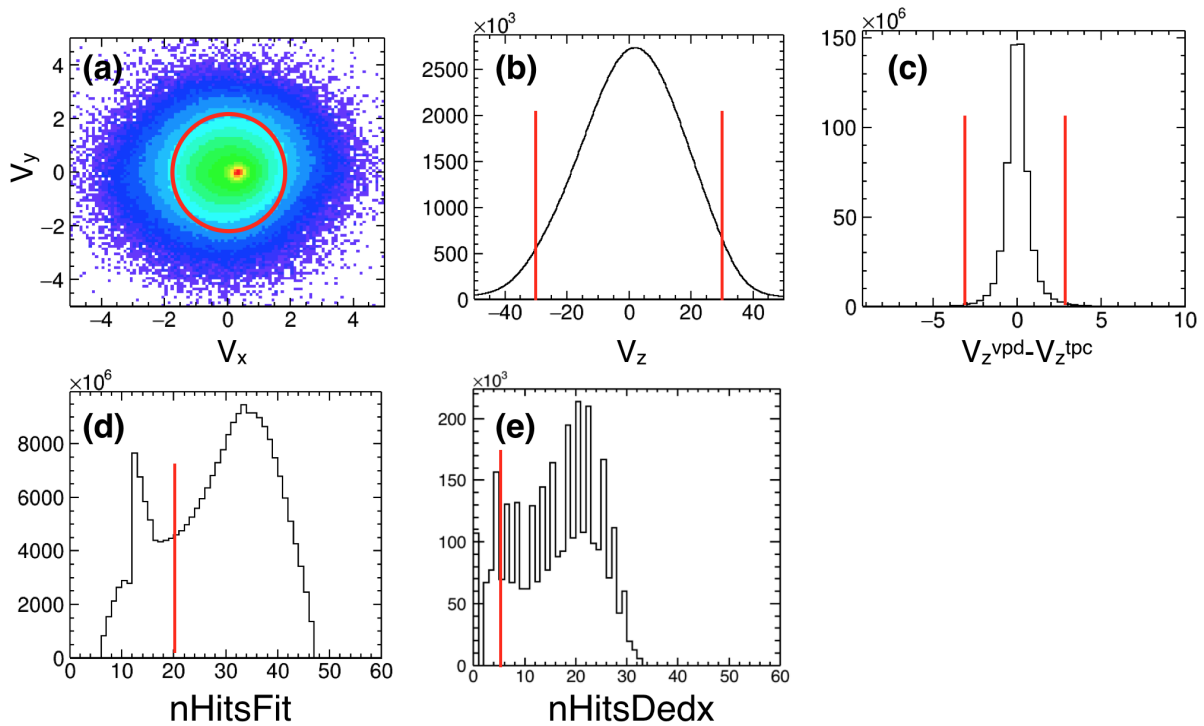


Figure 2.13: (a) Radial vertex position, (b) vertex position along the beam pipe, (c) the difference of vertex positions along the beam pipe between TPC and VPD, (d) number of hit points in TPC used for the track reconstruction (e) number of hit points in TPC used for calculating dE/dx .

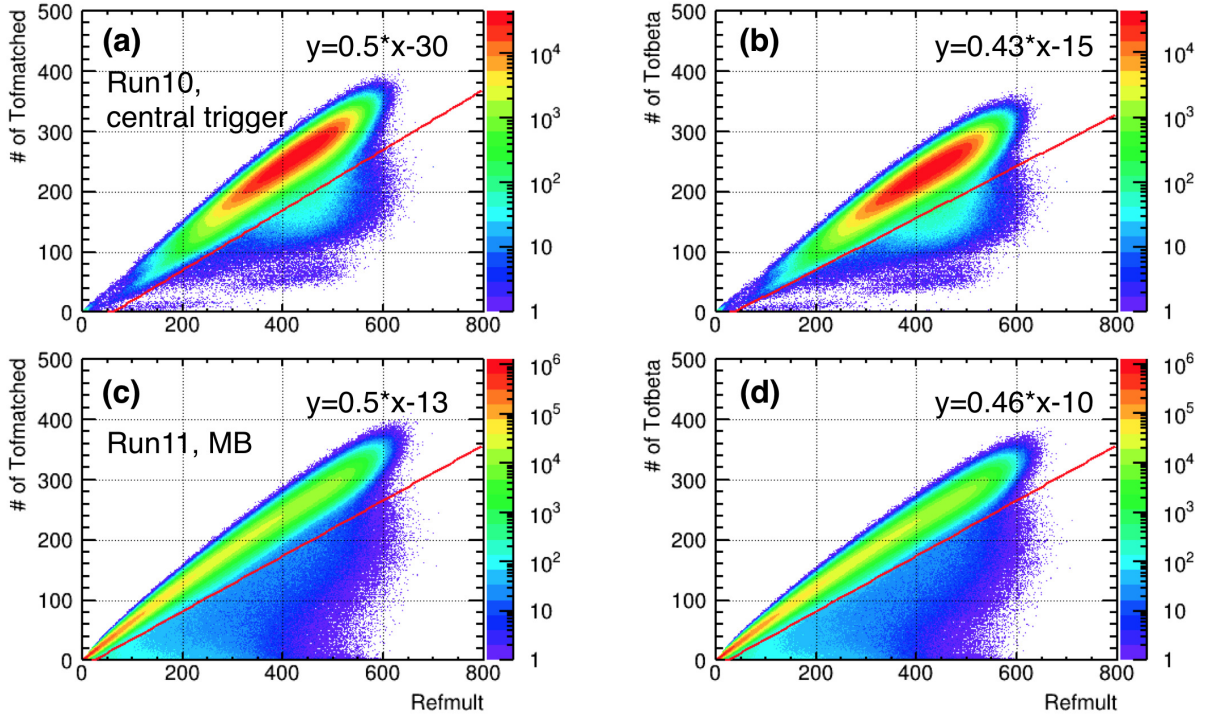


Figure 2.14: (a) Number of primary tracks associated with TOF, and (b) the number of primary tracks associated with TOF requiring $\beta > 0.1$ in the Run10 central trigger. (c) and (d) are for the Run11 minimum bias trigger.

2.3.3 Proton identification

Left hand side plot in Fig. 2.15 shows dE/dx measured by TPC as a function of momentum multiplied by charge. Protons and antiprotons are identified by using dE/dx measured by TPC at $0.4 < p_T < 0.8$ (GeV/c). At $0.8 < p_T < 2.0$ (GeV/c), however, it is difficult to identify protons only by using TPC due to the contamination from pions and kaons. Thus, at $0.8 < p_T < 2.0$ (GeV/c), combined PID with TOF is performed by requiring $0.6 < m^2 < 1.2$ (GeV/c²), which is shown in Fig. 2.15.

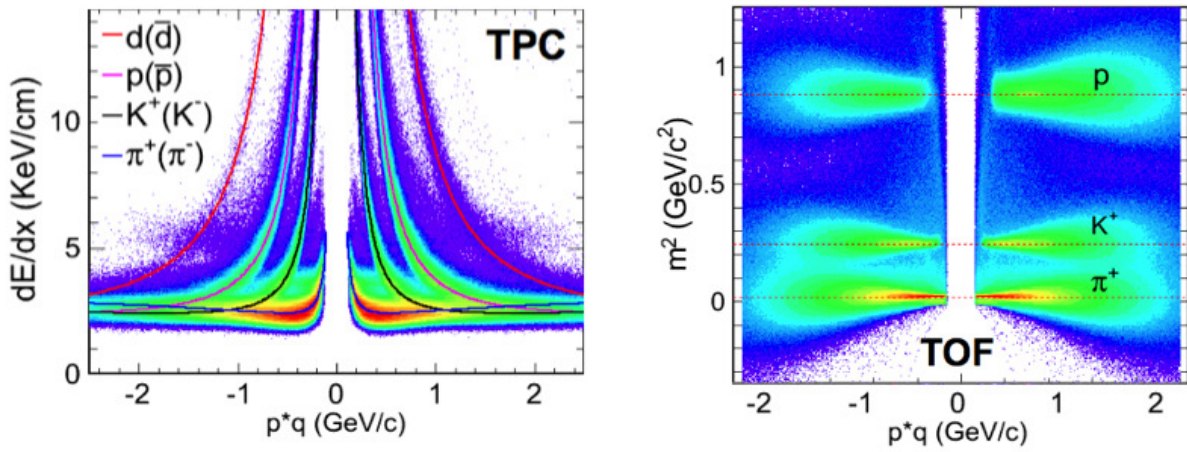


Figure 2.15: (Left) dE/dx measured by TPC as a function of momentum multiplied by charge. (Right) m^2 measured by TOF as a function of momentum multiplied by charge [20].

Chapter 3

Detector Effect

Experimentally, some particles with finite detector efficiency, which distorts the shape of event-by-event net-proton distributions. Conventional way to correct this effect is the analytical efficiency correction with the assumption of the binomial response of efficiency [33–36]. However, it is known that the efficiency correction does not work when the binomial assumption breaks. Unfolding is necessary to correct such effect. In this chapter, we show the conventional formulas for efficiency correction and their implementation. But the calculation cost for the conventional formulas increases with number of efficiency bins. In order to solve this problem, we show more efficient formulas that are robust to the increases of efficiency bins. Then we move to the discussions on details for our unfolding approach. Finally we try to investigate the non-binomial effect by using the existing embedding datasets.

3.1 Efficiency correction

3.1.1 Single efficiency bin

They are all derived based on the binomial model,

$$B(n, N; \varepsilon) = \frac{N!}{n!(N-n)!} \varepsilon^n (1-\varepsilon)^{N-n}, \quad (3.1)$$

where N and n denote the number of produced and measured particles, and ε represents the efficiency. When the efficiency follows the binomial distribution, the relationship between true and measured factorial moments can be expressed as

$$f_{i,j} = \varepsilon^i \bar{\varepsilon}^j F_{i,j}, \quad (3.2)$$

with F and f being true and measured factorial moments of the net-particle distribution. Since the relationships between measured and true cumulants are not straightforward, the efficiency correction is carried out using Eq. (3.2) as following steps:

- (a) Convert measured cumulants to measured factorial moments
- (b) Convert measured factorial moments to true factorial moments using Eq. (3.2)
- (c) Express the true cumulants in terms of true factorial moments

Final correction formulas can be found in Ref. [33] up to the sixth order cumulant, but it is cumbersome to implement those explicit formulas in our program. In order to automate the efficiency correction,

we decompose factorial moments into the correlation terms:

$$f_{ab} = \left\langle \sum_{i=0}^a s(a, i) M^i \sum_{j=0}^b s(b, j) \bar{M}^j \right\rangle = \sum_{i=0}^a \sum_{j=0}^b s(a, i) s(b, j) \langle M^i \bar{M}^j \rangle, \quad (3.3)$$

$$F_{ab} = \left\langle \sum_{i=0}^a s(a, i) N^i \sum_{j=0}^b s(b, j) \bar{N}^j \right\rangle = \sum_{i=0}^a \sum_{j=0}^b s(a, i) s(b, j) \langle N^i \bar{N}^j \rangle, \quad (3.4)$$

thus

$$\sum_{i=0}^a \sum_{j=0}^b \langle M^i \bar{M}^j \rangle = \varepsilon^a \bar{\varepsilon}^b \sum_{i=0}^a \sum_{j=0}^b \langle N^i \bar{N}^j \rangle, \quad (3.5)$$

where $s(n, k)$ denotes the Stirling number of the first kind (see B.1). The derivation of Eq. (3.5) can be found in B.2 Since $s(i, i) = 1$, we can deduce the following recursive expressions:

$$\begin{aligned} \langle M^a \bar{M}^b \rangle + \sum_{\substack{i, j \geq 0 \\ i, j \neq a, b}} s(a, i) s(b, j) \langle M^i \bar{M}^j \rangle &= \varepsilon^a \bar{\varepsilon}^b \langle N^a \bar{N}^b \rangle + \varepsilon^a \bar{\varepsilon}^b \sum_{\substack{i, j \geq 0 \\ i, j \neq a, b}} s(a, i) s(b, j) \langle N^i \bar{N}^j \rangle, \\ \rightarrow \langle N^a \bar{N}^b \rangle &= \frac{\langle M^a \bar{M}^b \rangle}{\varepsilon^a \bar{\varepsilon}^b} + \sum_{\substack{i, j \geq 0 \\ i, j \neq a, b}} s(a, i) s(b, j) \left(\frac{\langle M^i \bar{M}^j \rangle}{\varepsilon^a \bar{\varepsilon}^b} - \langle N^i \bar{N}^j \rangle \right), \end{aligned} \quad (3.6)$$

with the initial condition $\langle n^0 \bar{n}^0 \rangle = \langle N^0 \bar{N}^0 \rangle = 1$. In the case of fourth order cumulant, for example, what one needs to do is to calculate all combinations for $M^i \bar{M}^j$ with $i, j \geq 0$, where i and j cannot be 4 simultaneously. Then one obtains $\langle N^i \bar{N}^j \rangle$ ($a, b \leq 4$) by taking appropriate combinations for $\langle M^i \bar{M}^j \rangle$ recursively as shown in Eq. (3.6).

3.1.2 Many efficiency bins

Experimentally, efficiency depends on p_T , rapidity, azimuthal angles, and particle species, which needs to be implemented in the correction formulas. Number of factorial moments that we need to calculate for m th order cumulant with M efficiency bins is given by

$$N_m^{\text{fm}} = \sum_{r=1}^m {}_{r+M-1}C_r = {}_{m+M}C_m - 1, \quad (3.7)$$

, which indicates that the calculation cost becomes drastically large with increasing the efficiency bins. Therefore, if we apply efficiency correction precisely with many efficiency bins, the calculation will not finish with limited CPU time. In order to solve this problem, we have developed more efficient formulas by using the simple relationship between true and measured factorial cumulants as is seen in factorial moments in Eq. (3.2). We show final correction formulas up to sixth order cumulant and fourth order mixed cumulants.

$$\langle Q \rangle_c = \langle q_{(1,1)} \rangle_c, \quad (3.8)$$

$$\langle Q^2 \rangle_c = \langle q_{(1,1)}^2 \rangle_c + \langle q_{(2,1)} \rangle_c - \langle q_{(2,2)} \rangle_c, \quad (3.9)$$

$$\langle Q^3 \rangle_c = \langle q_{(1,1)}^3 \rangle_c + 3\langle q_{(1,1)}q_{(2,1)} \rangle_c - 3\langle q_{(1,1)}q_{(2,2)} \rangle_c + \langle q_{(3,1)} \rangle_c - 3\langle q_{(3,2)} \rangle_c + 2\langle q_{(3,3)} \rangle_c, \quad (3.10)$$

$$\begin{aligned} \langle Q^4 \rangle_c &= \langle q_{(1,1)}^4 \rangle_c + 6\langle q_{(1,1)}^2q_{(2,1)} \rangle_c - 6\langle q_{(1,1)}^2q_{(2,2)} \rangle_c + 4\langle q_{(1,1)}q_{(3,1)} \rangle_c + 3\langle q_{(2,1)}^2 \rangle_c \\ &\quad + 3\langle q_{(2,2)}^2 \rangle_c - 12\langle q_{(1,1)}q_{(3,2)} \rangle_c + 8\langle q_{(1,1)}q_{(3,3)} \rangle_c - 6\langle q_{(2,1)}q_{(2,2)} \rangle_c \\ &\quad + \langle q_{(4,1)} \rangle_c - 7\langle q_{(4,2)} \rangle_c + 12\langle q_{(4,3)} \rangle_c - 6\langle q_{(4,4)} \rangle_c, \end{aligned} \quad (3.11)$$

$$\begin{aligned} \langle Q^5 \rangle_c &= \langle q_{(1,1)}^5 \rangle_c + 10\langle q_{(1,1)}^3q_{(2,1)} \rangle_c - 10\langle q_{(1,1)}^3q_{(2,2)} \rangle_c + 10\langle q_{(1,1)}^2q_{(3,1)} \rangle_c - 30\langle q_{(1,1)}^2q_{(3,2)} \rangle_c \\ &\quad + 20\langle q_{(1,1)}^2q_{(3,3)} \rangle_c + 15\langle q_{(2,2)}^2q_{(1,1)} \rangle_c + 15\langle q_{(2,1)}^2q_{(1,1)} \rangle_c - 30\langle q_{(1,1)}q_{(2,1)}q_{(2,2)} \rangle_c \\ &\quad + 5\langle q_{(1,1)}q_{(4,1)} \rangle_c - 35\langle q_{(1,1)}q_{(4,2)} \rangle_c + 60\langle q_{(1,1)}q_{(4,3)} \rangle_c - 30\langle q_{(1,1)}q_{(4,4)} \rangle_c \\ &\quad + 10\langle q_{(2,1)}q_{(3,1)} \rangle_c - 30\langle q_{(2,1)}q_{(3,2)} \rangle_c + 20\langle q_{(2,1)}q_{(3,3)} \rangle_c \\ &\quad - 10\langle q_{(2,2)}q_{(3,1)} \rangle_c + 30\langle q_{(2,2)}q_{(3,2)} \rangle_c - 20\langle q_{(2,2)}q_{(3,3)} \rangle_c \\ &\quad + \langle q_{(5,1)} \rangle_c - 15\langle q_{(5,2)} \rangle_c + 50\langle q_{(5,3)} \rangle_c - 60\langle q_{(5,4)} \rangle_c + 24\langle q_{(5,5)} \rangle_c, \end{aligned} \quad (3.12)$$

$$\begin{aligned} \langle Q^6 \rangle_c &= \langle q_{(1,1)}^6 \rangle_c + 15\langle q_{(1,1)}^4q_{(2,1)} \rangle_c - 15\langle q_{(1,1)}^4q_{(2,2)} \rangle_c + 20\langle q_{(1,1)}^3q_{(3,1)} \rangle_c - 60\langle q_{(1,1)}^3q_{(3,2)} \rangle_c \\ &\quad + 40\langle q_{(1,1)}^3q_{(3,3)} \rangle_c - 90\langle q_{(1,1)}^2q_{(2,2)}q_{(2,1)} \rangle_c + 45\langle q_{(1,1)}^2q_{(2,1)}^2 \rangle_c + 45\langle q_{(1,1)}^2q_{(2,2)}^2 \rangle_c \\ &\quad + 15\langle q_{(2,1)}^3 \rangle_c - 15\langle q_{(2,2)}^3 \rangle_c + 15\langle q_{(1,1)}^2q_{(4,1)} \rangle_c - 105\langle q_{(1,1)}^2q_{(4,2)} \rangle_c + 180\langle q_{(1,1)}^2q_{(4,3)} \rangle_c - 90\langle q_{(1,1)}^2q_{(4,4)} \rangle_c \\ &\quad - 45\langle q_{(2,1)}^2q_{(2,2)} \rangle_c + 45\langle q_{(2,2)}^2q_{(2,1)} \rangle_c + 60\langle q_{(1,1)}q_{(2,1)}q_{(3,1)} \rangle_c - 180\langle q_{(1,1)}q_{(2,1)}q_{(3,2)} \rangle_c \\ &\quad + 120\langle q_{(1,1)}q_{(2,1)}q_{(3,3)} \rangle_c - 60\langle q_{(1,1)}q_{(2,2)}q_{(3,1)} \rangle_c + 180\langle q_{(1,1)}q_{(2,2)}q_{(3,2)} \rangle_c - 120\langle q_{(1,1)}q_{(2,2)}q_{(3,3)} \rangle_c \\ &\quad + 6\langle q_{(1,1)}q_{(5,1)} \rangle_c - 90\langle q_{(1,1)}q_{(5,2)} \rangle_c + 300\langle q_{(1,1)}q_{(5,3)} \rangle_c - 360\langle q_{(1,1)}q_{(5,4)} \rangle_c + 144\langle q_{(1,1)}q_{(5,5)} \rangle_c \\ &\quad + 15\langle q_{(2,1)}q_{(4,1)} \rangle_c - 105\langle q_{(2,1)}q_{(4,2)} \rangle_c + 180\langle q_{(2,1)}q_{(4,3)} \rangle_c - 90\langle q_{(2,1)}q_{(4,4)} \rangle_c \\ &\quad - 15\langle q_{(2,2)}q_{(4,1)} \rangle_c + 105\langle q_{(2,2)}q_{(4,2)} \rangle_c - 180\langle q_{(2,2)}q_{(4,3)} \rangle_c + 90\langle q_{(2,2)}q_{(4,4)} \rangle_c \\ &\quad + 10\langle q_{(3,1)}^2 \rangle_c - 60\langle q_{(3,1)}q_{(3,2)} \rangle_c + 40\langle q_{(3,1)}q_{(3,3)} \rangle_c + 90\langle q_{(3,2)}^2 \rangle_c - 120\langle q_{(3,2)}q_{(3,3)} \rangle_c + 40\langle q_{(3,3)}^2 \rangle_c \\ &\quad + \langle q_{(6,1)} \rangle_c - 31\langle q_{(6,2)} \rangle_c + 180\langle q_{(6,3)} \rangle_c - 390\langle q_{(6,4)} \rangle_c + 360\langle q_{(6,5)} \rangle_c - 120\langle q_{(6,6)} \rangle_c, \end{aligned} \quad (3.13)$$

$$\langle Q_{(x)} Q_{(y)} \rangle_c = \langle q_{(1,0,1)} q_{(0,1,1)} \rangle_c + \langle q_{(1,1,1)} \rangle_c - \langle q_{(1,1,2)} \rangle_c, \quad (3.14)$$

$$\begin{aligned} \langle Q_{(x)}^2 Q_{(y)} \rangle_c &= \langle q_{(1,0,1)}^2 q_{(0,1,1)} \rangle_c + 2\langle q_{(1,0,1)} q_{(1,1,1)} \rangle_c - 2\langle q_{(1,0,1)} q_{(1,1,2)} \rangle_c + \langle q_{(0,1,1)} q_{(2,0,1)} \rangle_c - \langle q_{(0,1,1)} q_{(2,0,2)} \rangle_c \\ &\quad + \langle q_{(2,1,1)} \rangle_c - 3\langle q_{(2,1,2)} \rangle_c + \langle q_{(2,1,3)} \rangle_c, \end{aligned} \quad (3.15)$$

$$\begin{aligned} \langle Q_{(x)}^2 Q_{(y)}^2 \rangle_c &= \langle q_{(1,0,1)}^2 q_{(0,1,1)}^2 \rangle_c \\ &\quad + \langle q_{(1,0,1)}^2 q_{(0,2,1)} \rangle_c - \langle q_{(1,0,1)}^2 q_{(0,2,2)} \rangle_c + \langle q_{(0,1,1)}^2 q_{(2,0,1)} \rangle_c - \langle q_{(0,1,1)}^2 q_{(2,0,2)} \rangle_c \\ &\quad + 4\langle q_{(1,0,1)} q_{(0,1,1)} q_{(1,1,1)} \rangle_c - 4\langle q_{(1,0,1)} q_{(0,1,1)} q_{(1,1,2)} \rangle_c \\ &\quad + 2\langle q_{(1,0,1)} q_{(1,2,1)} \rangle_c - 6\langle q_{(1,0,1)} q_{(1,2,2)} \rangle_c + 4\langle q_{(1,0,1)} q_{(1,2,3)} \rangle_c \\ &\quad + 2\langle q_{(0,1,1)} q_{(2,1,1)} \rangle_c - 6\langle q_{(0,1,1)} q_{(2,1,2)} \rangle_c + 4\langle q_{(0,1,1)} q_{(2,1,3)} \rangle_c \\ &\quad - 4\langle q_{(1,1,1)} q_{(1,1,2)} \rangle_c + 2\langle q_{(1,1,1)}^2 \rangle_c + 2\langle q_{(1,1,2)}^2 \rangle_c \\ &\quad + \langle q_{(2,0,1)} q_{(0,2,1)} \rangle_c - \langle q_{(2,0,1)} q_{(0,2,2)} \rangle_c - \langle q_{(2,0,2)} q_{(0,2,1)} \rangle_c + \langle q_{(2,0,2)} q_{(0,2,2)} \rangle_c \\ &\quad + \langle q_{(2,2,1)} \rangle_c - 7\langle q_{(2,2,2)} \rangle_c + 12\langle q_{(2,2,3)} \rangle_c - 6\langle q_{(2,2,4)} \rangle_c, \end{aligned} \quad (3.16)$$

$$\begin{aligned} \langle Q_{(x)}^3 Q_{(y)} \rangle_c &= \langle q_{(1,0,1)}^3 q_{(0,1,1)} \rangle_c \\ &\quad + 3\langle q_{(1,0,1)}^2 q_{(1,1,1)} \rangle_c - 3\langle q_{(1,0,1)}^2 q_{(1,1,2)} \rangle_c + 3\langle q_{(2,0,1)} q_{(1,0,1)} q_{(0,1,1)} \rangle_c - 3\langle q_{(2,0,2)} q_{(1,0,1)} q_{(0,1,1)} \rangle_c \\ &\quad + 3\langle q_{(1,0,1)} q_{(2,1,1)} \rangle_c - 9\langle q_{(1,0,1)} q_{(2,1,2)} \rangle_c + 6\langle q_{(1,0,1)} q_{(2,1,3)} \rangle_c \\ &\quad + 3\langle q_{(2,0,1)} q_{(1,1,1)} \rangle_c - 3\langle q_{(2,0,1)} q_{(1,1,2)} \rangle_c - 3\langle q_{(2,0,2)} q_{(1,1,1)} \rangle_c + 3\langle q_{(2,0,2)} q_{(1,1,2)} \rangle_c \\ &\quad + \langle q_{(3,0,1)} q_{(0,1,1)} \rangle_c - 3\langle q_{(3,0,2)} q_{(0,1,1)} \rangle_c + 2\langle q_{(3,0,3)} q_{(0,1,1)} \rangle_c \\ &\quad + \langle q_{(3,1,1)} \rangle_c - 7\langle q_{(3,1,2)} \rangle_c + 12\langle q_{(3,1,3)} \rangle_c - 6\langle q_{(3,1,4)} \rangle_c, \end{aligned} \quad (3.17)$$

where we used the symbol

$$q_{(r,s)} = q_{(a^r/p^s)} = \sum_{i=1}^M (a_i^r/p_i^s) n_i, \quad (3.18)$$

$$q_{(r,s,t)} = q_{(x^r y^s/p^t)} = \sum_{i=1}^M (x_i^r y_i^s/p_i^t) n_i. \quad (3.19)$$

This work is published in Physical Review C [21], where we also discussed the importance of precise efficiency correction with many efficiency bins.

We performed the calculation for efficiency correction in case of many efficiency bins up to 4+4, with simple toy model for both factorial moment method and new method. It was found that both methods give exactly the same value numerically. Comparison of number of necessary terms in correction formulas are compared between two methods as a function of number of efficiency bins in Fig. 3.1. It can be found that the number of terms are reduced by a factor of 100 in new methods N_6^c compared to factorial moment method N_6^c , and also it does not depend on the number of efficiency bins. CPU time is also compared in Tab. 3.1, where we see that the CPU time is drastically reduced compared to the conventional formulas.

3.1.3 Importance of precise efficiency correction

In previous section, we show more efficient formulas for efficiency correction. Then the question is, however, whether we really need to apply precise efficiency correction with many bins. In order to

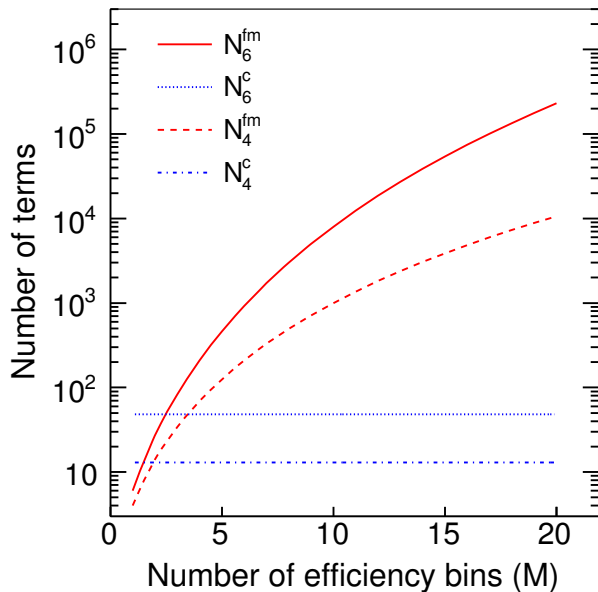


Figure 3.1: Comparison of number of necessary terms in correction formulas in two methods [21].

M	factorial moment	new method
4	64.7s	30.8s
8	17.3×10^2 s	31.3s
12	14.1×10^3 s	32.3s
200	—	62.7s

Table 3.1: Comparison of CPU time to calculate the sixth order cumulant between the conventional and new methods [21].

answer this question, we performed simple analytical calculation. The setup is following. We assume one distribution that we want to measure cumulants, which consists of two internal independent distributions. Both distributions have exactly the same value of cumulants C_n , then the cumulants for whole distributions is are $2C_n$. Also we assume two distributions have different efficiencies. We apply efficiency correction by using the averaged efficiency for two distributions, then the deviation ΔK_n can be expressed as:

$$\Delta K_2 = \frac{1}{2} \left(\frac{\Delta \varepsilon}{\bar{\varepsilon}} \right)^2 (C_2 - C_1), \quad (3.20)$$

$$\Delta K_3 = \frac{3}{2} \left(\frac{\Delta \varepsilon}{\bar{\varepsilon}} \right)^2 (C_3 - 2C_2 + C_1), \quad (3.21)$$

$$\Delta K_4 = \frac{1}{2} \left(\frac{\Delta \varepsilon}{\bar{\varepsilon}} \right)^2 (6C_4 - 18C_3 + 19C_2 - 7C_1) + \frac{1}{8} \left(\frac{\Delta \varepsilon}{\bar{\varepsilon}} \right)^4 (C_4 - 6C_3 + 11C_2 - 6C_1), \quad (3.22)$$

Equations (3.20–3.22) are plotted in Fig. 3.2 as a function of $\Delta \varepsilon$ with assuming the averaged efficiency to be $\bar{\varepsilon} = 0.5$. Figure 3.2 (a) assumes Gaussian distribution where more than second order cumulants are zero. Figure 3.2 (b) assumes 5% deviation of cumulants from the usual Poisson distribution. It can be found that the deviations from the true values become large with increasing the efficiency difference, and higher order cumulants have large deviation compared to lower orders. Interestingly, ΔK_n becomes zero by substituting $C_n = C_1$ to Eqs. (3.20)–(3.22) assuming the Poisson distributions. Since we measure the deviation from Poisson as a signal from the QCD critical point or phase transition, it is important for us to apply precise efficiency correction with appropriate efficiency bins.

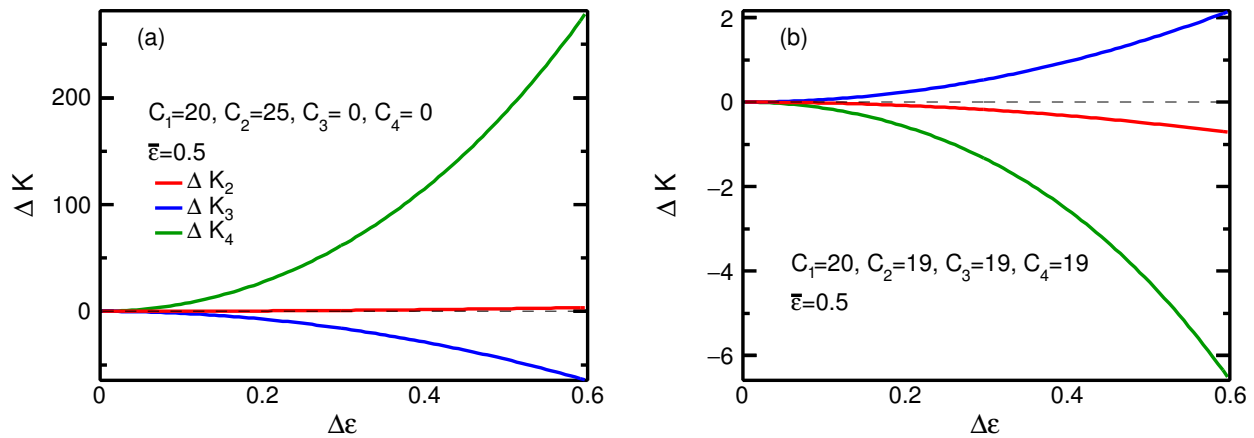


Figure 3.2: Deviation of the efficiency corrected values of cumulants using averaged efficiency, assuming (a) Gauss distribution and (b) distribution that has 5% smaller cumulants than Poisson distribution.

3.1.4 Statistical error estimation

Two methods are currently suggested for statistical error estimation for higher order cumulants. One is the Delta theorem and the other one is bootstrap [35, 37]. Delta theorem is the analytical way to estimate the statistical errors for cumulants and moments, but it is cumbersome to derive analytical formulas for higher order cumulants. In addition, those formulas are much complicated after efficiency correction, which will make the implementation very difficult in the case of many efficiency bins. On the other hand, bootstrap is very simple. One makes the new net-proton multiplicity distribution by random sampling from the original distribution and calculate cumulants. This is repeated with around 300 times, then the RMS of cumulants with 300 independent trials is taken as the statistical errors. Any en route calculation such as CBWC and the efficiency correction can be included inside the bootstrap. Therefore, bootstrap is used for the statistical error estimation for sixth order cumulant.

In a simple case of single efficiency bin, bootstrap is performed by random sampling from the two dimensional histogram between protons and antiprotons, which can be easily done by TH2D::GetRandom function in ROOT. In the case of many efficiency bins, however, further implementations are necessary. Suppose we estimate the statistical errors in case of $n+n$ efficiency bins. We prepare the $2n$ dimensional histograms which contains the bin coordinate with its contents. After normalization for bin contents, bin coordinates can be randomly selected by generating random numbers from 0 to 1 for each sampling.

In order to justify the bootstrap, we performed simple toy model calculations. The setup for the toy model is following. We generate four Poisson distributions with 1M events, two are for protons and the others are for antiprotons, where the mean parameter for Poisson is 5, 4, 3, and 1, respectively. Those distributions are randomly sampled with corresponding efficiencies, 80%, 60%, 70% and 90%. Then we apply efficiency correction to calculate C_6 and C_6/C_2 . Similarly, this procedure is also performed with respect to a new distribution made by random sampling from the original distribution, which is repeated with 300 times with 300 different (but sampled from the same original distribution) distributions. Then RMS of C_6 and C_6/C_2 are taken as the statistical errors. These procedures are randomly and independently performed with 50 times, which is shown in Fig. 3.3. The number of points touching the averaged value for 50 trials is 37 and 32 for C_6 and C_6/C_2 . They correspond to

74% and 64%, which are reasonable values of 1σ for a Gauss distribution to justify bootstrap for C_6 and C_6/C_2 .

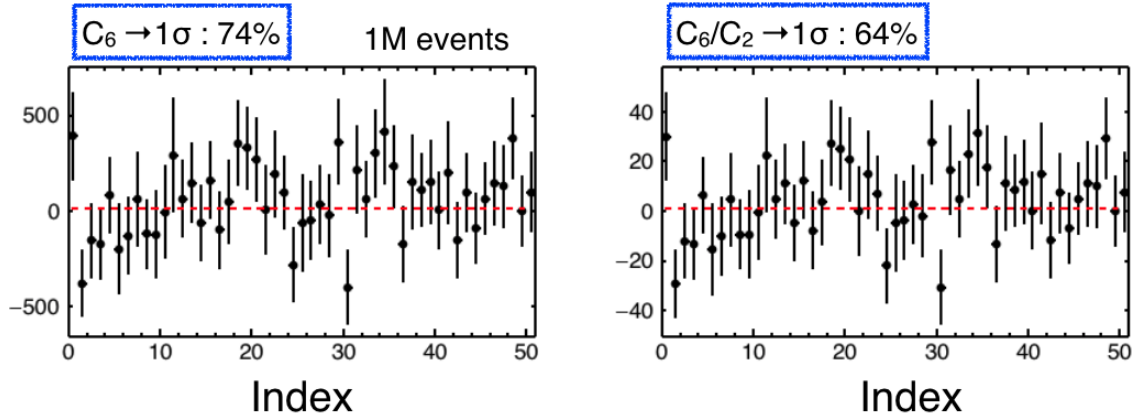


Figure 3.3: Efficiency corrected C_6 and C_6/C_2 and their statistical errors estimated by bootstrap, as a function of 50 independent trials. Red dotted lines represent the averaged value for 50 trials.

3.2 Unfolding

Efficiency correction formulas are derived based on the binomial response of efficiency. This binomial model can be broken in the experiment due to the track merging or splitting that occurs in the detector level. Reference [38] firstly demonstrates the effect of non-binomial efficiency. Once we apply efficiency correction under the non-binomial situation, then the results will be artificially changed, and the effect become large for higher order cumulants. Such non-binomial detector effect can no longer corrected by analytical approach – we need unfolding. Unfolding is the method to correct the detector effect, which is provided in ROOT as RooUnfold package [39]. However, most of programs are already packaged in the library, and users cannot touch the details for the implementations. In addition, it is limited to three dimensional unfolding. Since we should be totally clear for analysis methods especially to search for unknown distributions predicted around the QCD critical point, we start to develop new unfolding methods from scratch. In recent work, it was found that our unfolding method can easily correct the volume fluctuation, and it can be also extended to the multidimensional case, which is strong advantage compared to the existing unfolding method. Unfortunately discussions here are limited to basic part of our unfolding method, I hope those advanced unfolding method will be presented in other literature. Correction for non-binomial effect on higher order cumulants is first attempt in the STAR experiment. unfolding for sixth order cumulant is world's first attempt. In this section, we show the methodology of our unfolding method, then consider some non-binomial scenario expected in the STAR experiment from the embedding data.

3.2.1 Methodology

Poisson test

We explain the methodology with a simple toy model by using Poisson distributions. Figure 3.4 shows the flowchart for our unfolding method. As a setup, we first generate two two dimensional histograms for protons and antiprotons, one is for (A) experimental true distribution and the other is

for (B) simulation true distribution. Since the simulations are not complete and there should be some deviation compared to experiment, mean parameter for Poisson is set to be different between (A) and (B) as $\mu_{\text{exp,p}} = 10$, $\mu_{\text{exp,pbar}} = 7$, $\mu_{\text{sim,p}} = 12$ and $\mu_{\text{sim,pbar}} = 9$. We apply the detector effect which we call "MC filter", here we simply assume binomial efficiency $\varepsilon_{\text{p}} = 0.9$ and $\varepsilon_{\text{pbar}} = 0.7$, to (A) and (B) to make (C) experimental measured and (D) simulation measured distributions. Our goal is to reconstruct (A) by using (B), (C), (D) and MC filter. Our method consists of two kinds of unfolding approach. Let us start from the "incremental" unfolding approach.

1. Define the correction functions by the difference between experimental and simulation measured distributions (B)–(D) as shown in (C.F._rec).
2. Considering that such difference between experiment and simulation in reconstructed coordinate should also appear in generated coordinate, convert the correction function (C.F._rec) to (C.F._gen) by using the reversed response matrix RM_{rev} .
3. Apply smoothing to the correction function (C.F._gen).
4. Apply the correction function (C.F._gen) with scaling factor α to the simulation true distribution (C) to get (C') which is slightly modified to close to the experimental true distribution (D).
5. Apply MC filter again to the modified simulation true distribution (C') to generate the modified simulation measured distribution (D'), which is again compared to the experimental measured distribution (B).
6. Repeat 2–5 with substantial iterations.

Reversed response matrix RM_{rev} in 2 can be constructed in each iteration when we apply MC filter to the simulation true distribution. Smoothing in 3 is required to make the distribution smooth. Scaling factor α in 4 is essential to avoid the negative bin content after applying the correction function. In this approach, we apply MC filter iteratively to the simulation true distribution. Starting from the any distribution in simulation true, it should be incrementally modified to the experimental true distribution by comparing with the experimental measured distribution in each iteration. Thus we call this approach "incremental" unfolding. Cumulants in each iteration are plotted in Fig. 3.5. Red lines represent the true cumulants and black lines are incremental unfolding. Many lines are superimposed, which represents 30 independent trials for Fig. 3.4. It can be found that the cumulants of incremental unfolding becomes close to true values with iterations, but it seems difficult for C_3 and C_4 to recover the input values. This would be because we apply MC filter in each iteration, which might lead to unstable results of higher order cumulants. In order to solve this problem, another unfolding approach is implemented that we call "conventional" unfolding. After additional iterations for incremental unfolding, we switch to the conventional unfolding where we don't apply MC filter. We let $\text{RM}_{\text{inc,for}}$ and $\text{RM}_{\text{inc,rev}}$ being the forward and reversed response matrix defined in the last iteration for incremental unfolding.

1. Apply $\text{RM}_{\text{inc,rev}}$ to the experimental measured distribution to obtain the simulation true distribution.
2. Refold the simulation true distribution by using $\text{RM}_{\text{inc,for}}$ to make a simulation measured distribution.
3. Define the correction functions by taking the difference from the experimental measured distribution.

4. After conversion of correction functions from reconstructed to generated coordinate, apply it to the simulation true distribution.
5. Repeat 2–5 until cumulants for net-distribution converge.

Since we don't apply MC filter and don't update the response matrix, this "conventional" unfolding get quickly converged as shown in blue lines in Fig. 3.5.

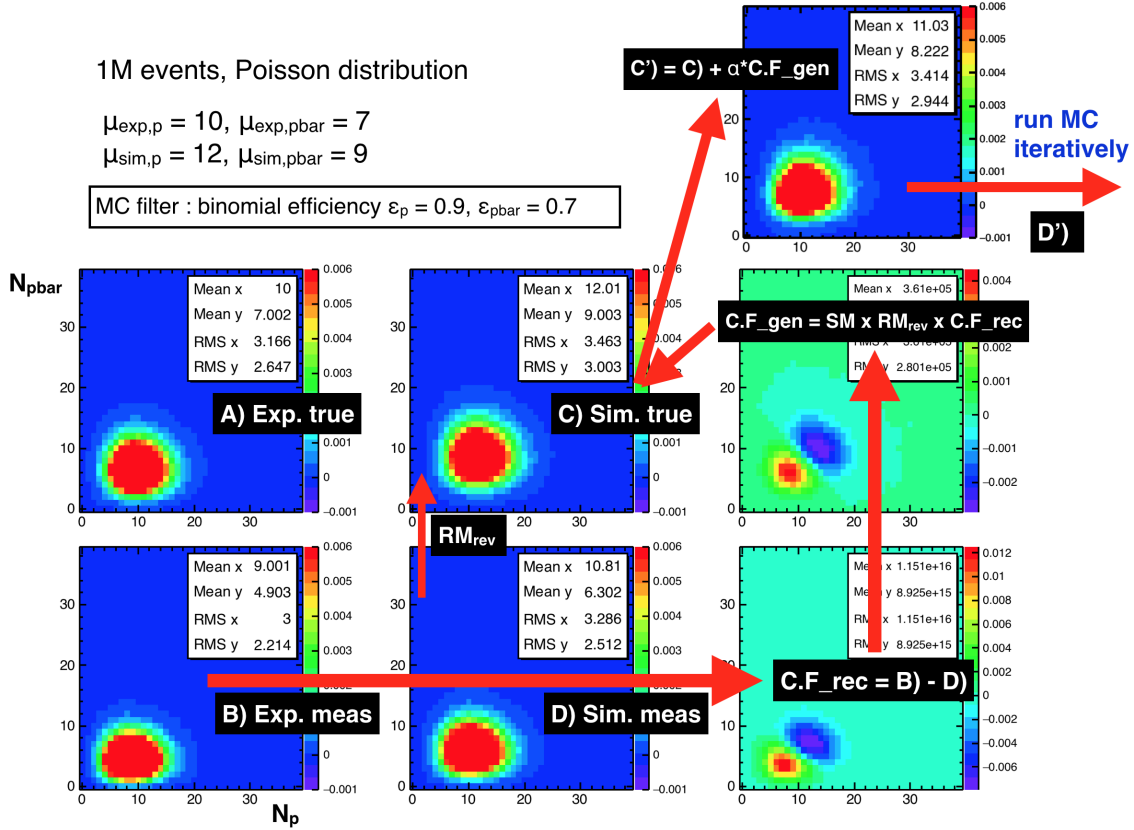


Figure 3.4: Flowchart for our unfolding method by using simple toy model with Poisson distributions. (A) is the experimental true, (B) is the simulation true, (C) is the experimental measured and (D) is the simulation measured distribution. RM_{rev} is the reversed response matrix. (C.F._rec) and (C.F._gen) are correction functions in reconstructed and generated coordinates.

Critical shape test

Since our new unfolding approach were originally motivated by reconstruction of the unknown shape of the conserved charge distributions predicted around the QCD critical point, we performed a critical shape test to show the feasibility of our unfolding method. Figure 3.6 shows the initial distributions in the critical shape test. Critical shape is assumed to have larger (or wider) Gauss distribution than the Poisson distribution at smaller (or larger) N_p values. Our goal is to reconstruct this critical shape starting from the simple Poisson distribution for simulation true distribution. Methodology is the same with performed in Poisson test. 100 and 200 iterations have been performed for incremental and conventional unfolding respectively. Two-dimensional distributions are shown in Fig. 3.7 at the

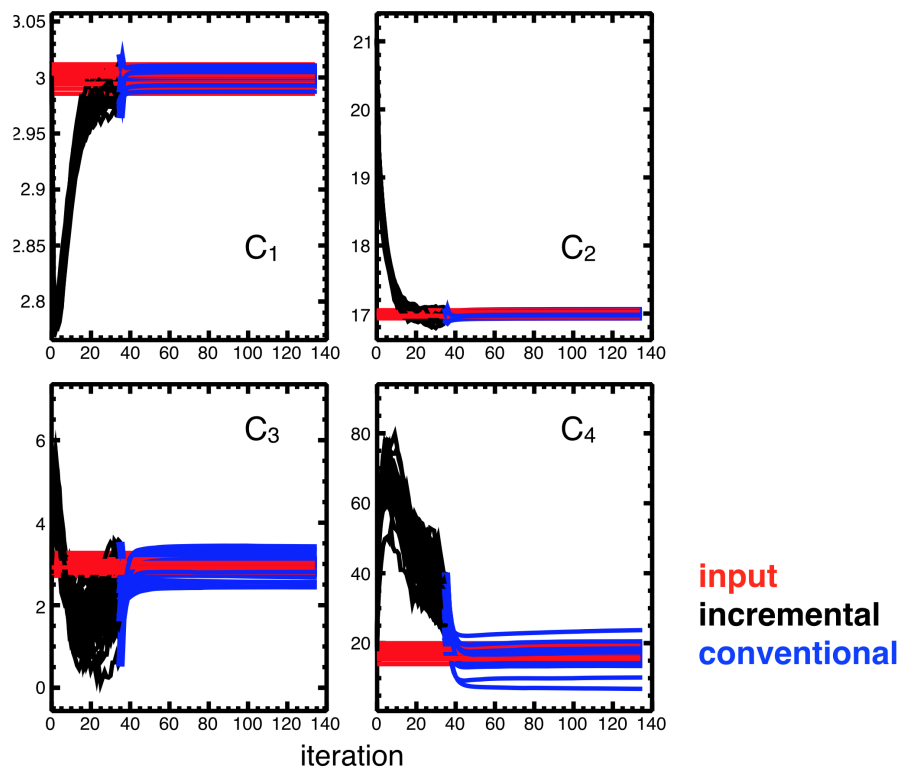


Figure 3.5: Cumulants up to fourth order as a function of iteration. Red lines represent the true cumulants, black lines are incremental unfolding, and blue lines are conventional unfolding. Results of independent 30 trials are superimposed.

different stage of iterations as well as initial distributions for experiment and simulation. A simple Poisson distribution is modified step by step, and finally the critical shape has been recovered. Let us also look at the net-distribution in Fig. 3.8. We see the two-peak structure for the critical shape. Starting from the simple Skellam distribution, two-peak structure has been recovered. Resulting cumulants are shown as a function of number of iterations in Fig. 3.9. We see that our unfolding approach works well to give true cumulants, and it can be found that the value of C_4 has been successfully modified from the value of Skellam to -2500.

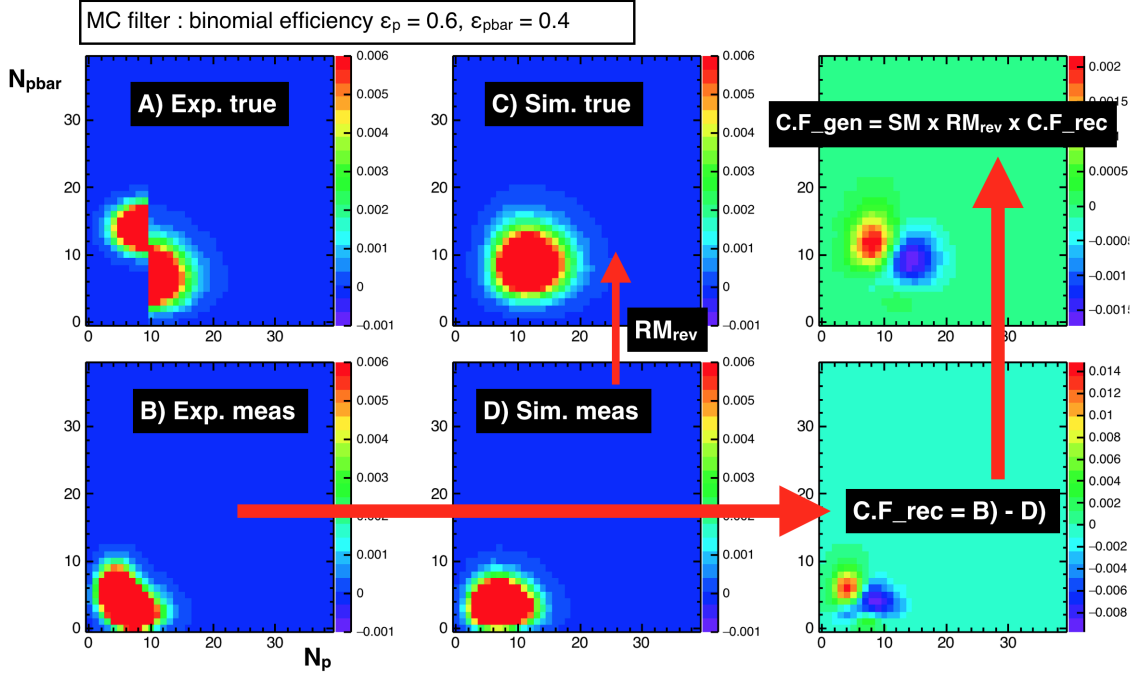


Figure 3.6: Flowchart for our unfolding method by using critical a distribution. (A) is the experimental true, (B) is the simulation true, (C) is the experimental measured and (D) is the simulation measured distribution. RM_{rev} is the reversed response matrix. (C.F._rec) and (C.F._gen) are correction functions in reconstructed and generated coordinates.

Statistical error

Statistical errors for unfolding can be estimated by bootstrap. A simple toy model calculation has been performed to show the feasibility of bootstrap on the unfolding. Figure. 3.10 shows the cumulants up to fourth order as a function of 100 independent trials. At each data point, bootstrap is performed by random sampling from the same experimental true distribution with 100 times. In the next trial, another experimental true distribution are independently generated to which we apply bootstrap sampling. This procedure is repeated with respect to 100 independent experimental true distribution. It can be found that the probability of data points touching the averaged value over 100 trials are around 70%, which shows that bootstrap works well for unfolding.

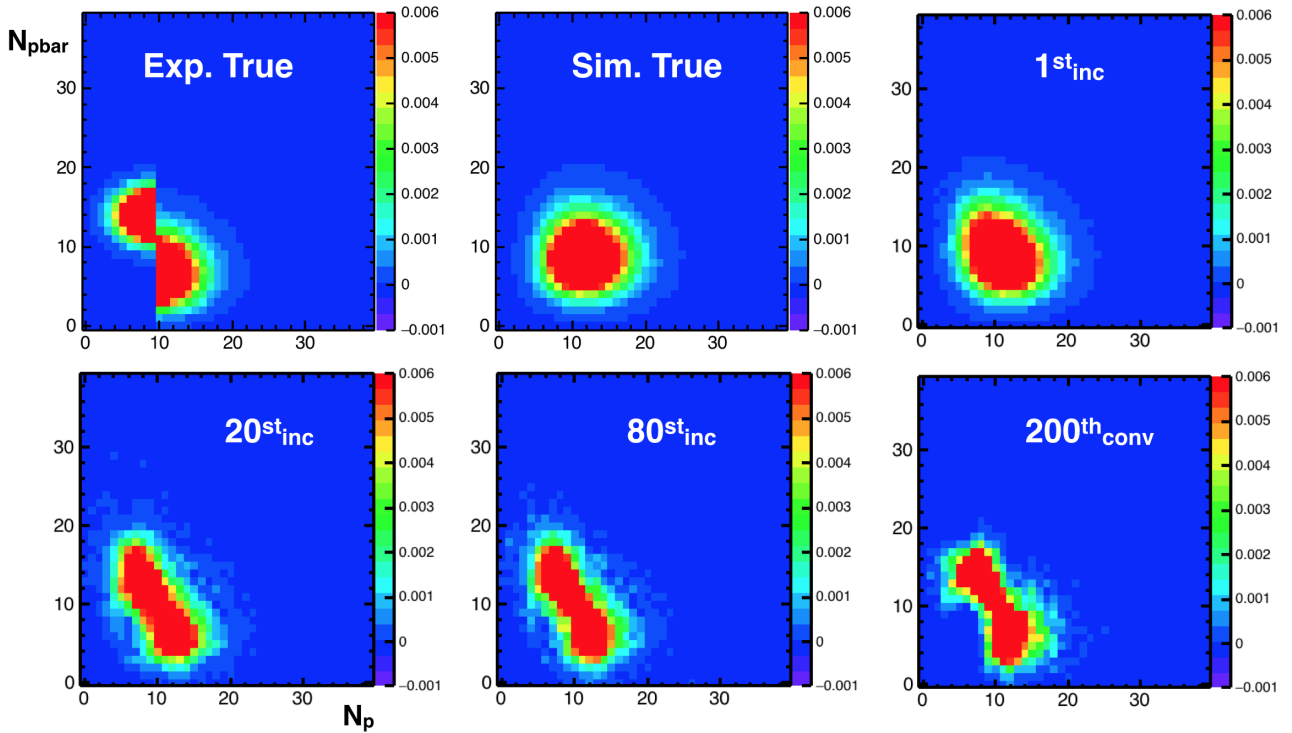


Figure 3.7: Two-dimensional distributions for protons and antiprotons at 1st, 20th and 80th iteration of incremental unfolding, and 200th iteration of conventional unfolding Initial distributions for experiment and simulation are also shown.

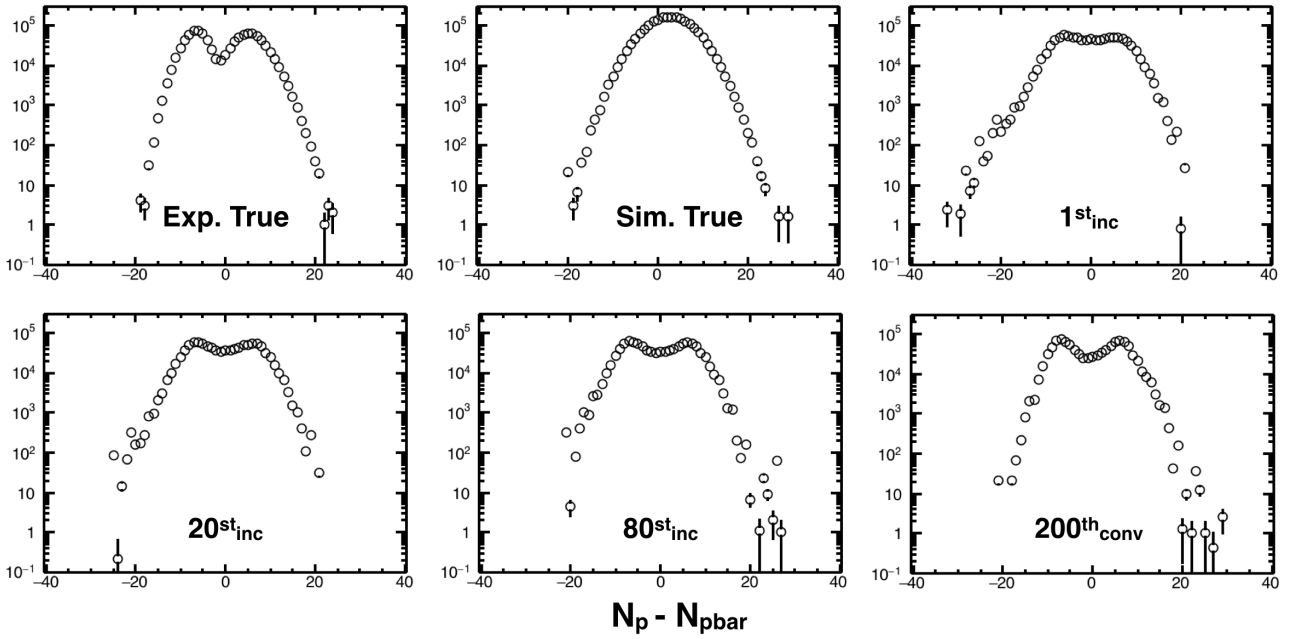


Figure 3.8: Net-proton distributions at 1st, 20th and 80th iteration of incremental unfolding, and 200th iteration of conventional unfolding Initial distributions for experiment and simulation are also shown.

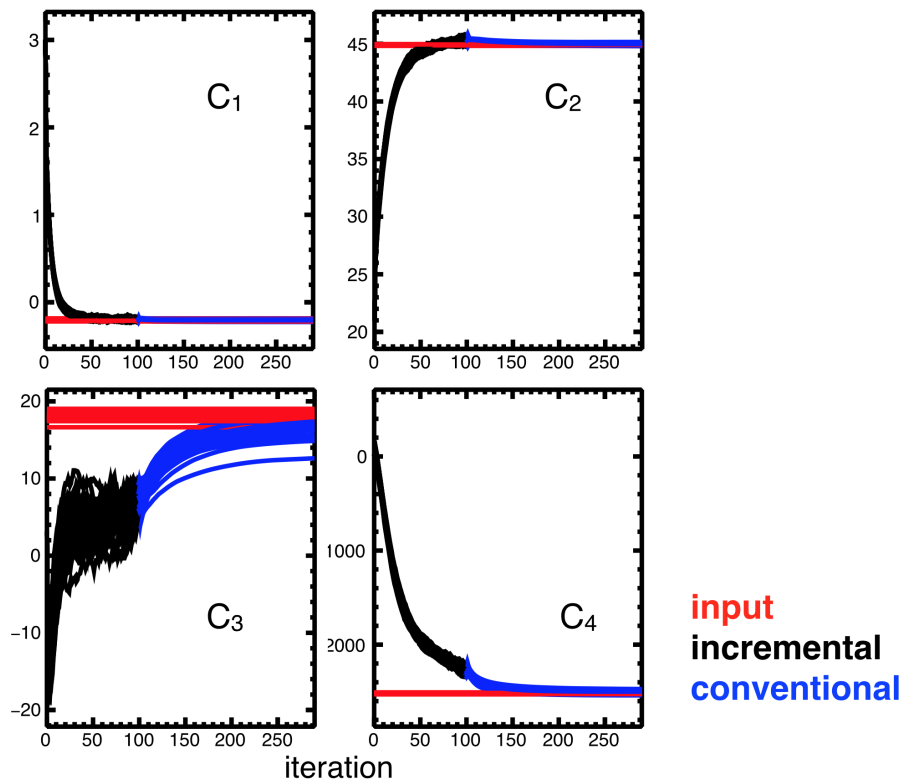


Figure 3.9: Cumulants up to fourth order as a function of iteration. Red lines represent the true cumulants, black lines are incremental unfolding, and blue lines are conventional unfolding. Results of independent 30 trials are superimposed.

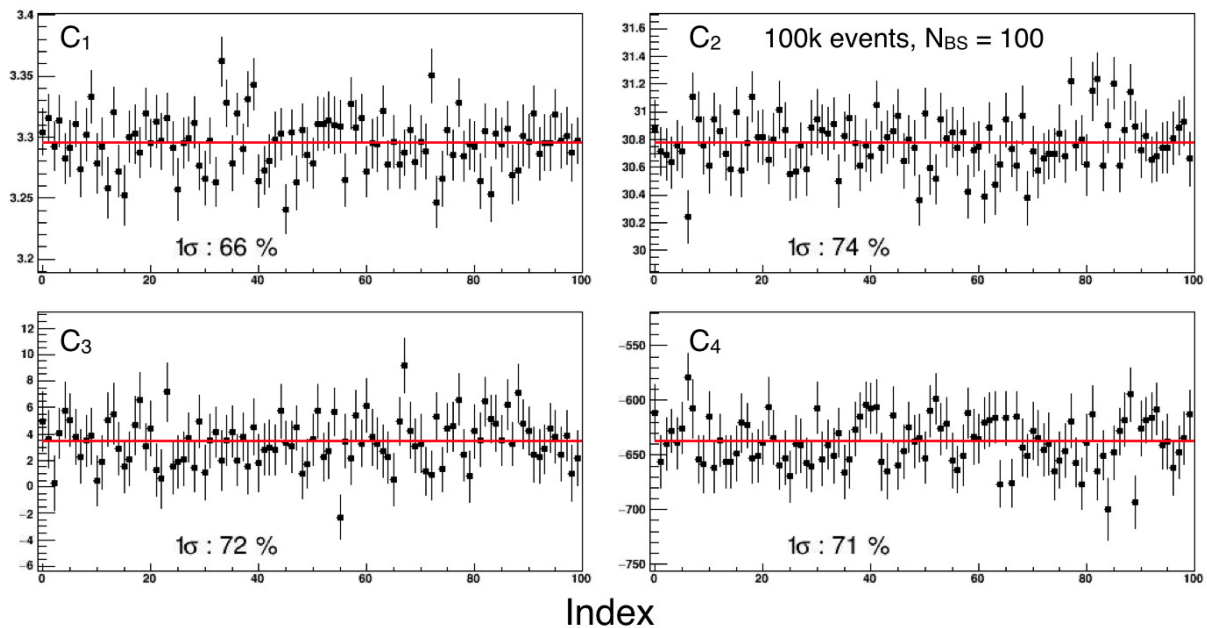


Figure 3.10: Results of toy model calculation with 100 bootstrap samplings with 100k events. Cumulants up to fourth order are shown as a function of 100 independent trials. Red lines represent the averaged value over trials.

3.2.2 Binomial model

Our main motivation on the unfolding is to correct the non-binomial efficiency. Before we start to study the effect of non-binomial efficiency, however, it is important to check whether the unfolding with binomial model gives the consistent results with efficiency correction or not. In the efficiency correction, p_T dependent efficiency has been implemented. For unfolding, it can be simply included inside the MC filter as shown in Fig. 3.11. We know the fractions of low and high p_T regions $F_{p(pbar), low}$ and $F_{p(pbar), high}$, which are calculated by efficiency corrected C_1 (mean) value separately for low and high p_T regions. Based on the information in a two-dimensional histogram in generated coordinate, we can divide the number of (anti)protons to low and high p_T regions. We apply the MC filter with the binomial efficiency in a corresponding bin. They are merged to be filled into the two-dimensional histogram in the reconstructed coordinate. Figure 3.12 shows the results of unfolding at $\sqrt{s_{NN}} = 200$ GeV. Unfolded distributions are shown in top panels. This is the first attempt to look at the corrected distributions. Bottom panels are cumulants up to fourth order for both efficiency correction and unfolding with binomial model. It can be found that both results are consistent, which shows the validity of our unfolding method. Note that the statistical errors for unfolding are slightly larger than efficiency correction, which is due to the MC statistics. Both statistical errors should be identical if we have substantial CPU time to increase the MC statistics.

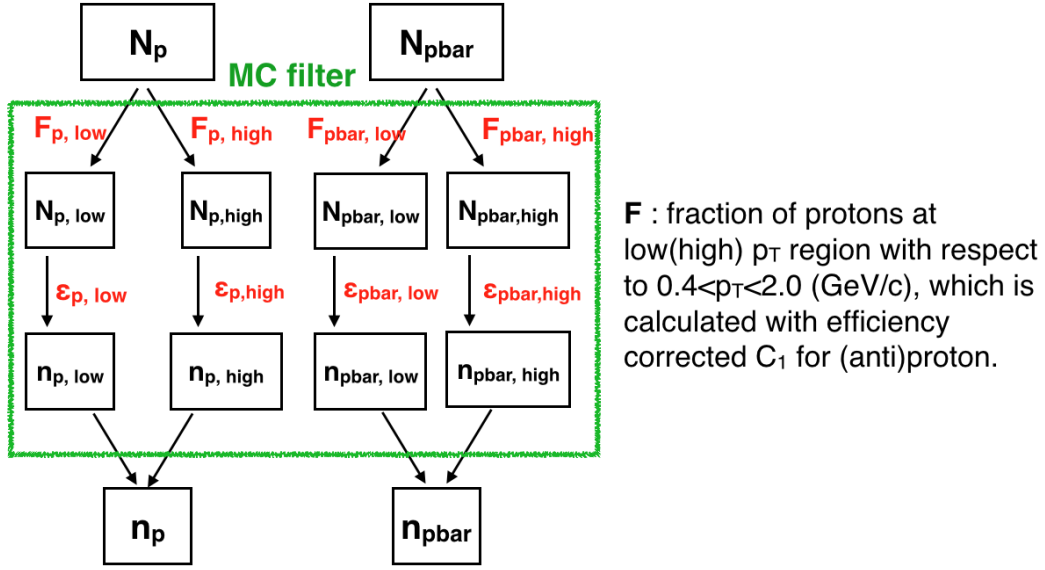


Figure 3.11: An image for the implementation of efficiency bins in unfolding. $N_{p(pbar), low(high)}$ and $n_{p(pbar), low(high)}$ are generated and reconstructed number of (anti)protons at low(high) p_T regions. $F_{p(pbar), low(high)}$ is the fraction at low and high p_T regions with respect to combined p_T . $\epsilon_{p(pbar), low(high)}$ is the efficiency in a corresponding bin.

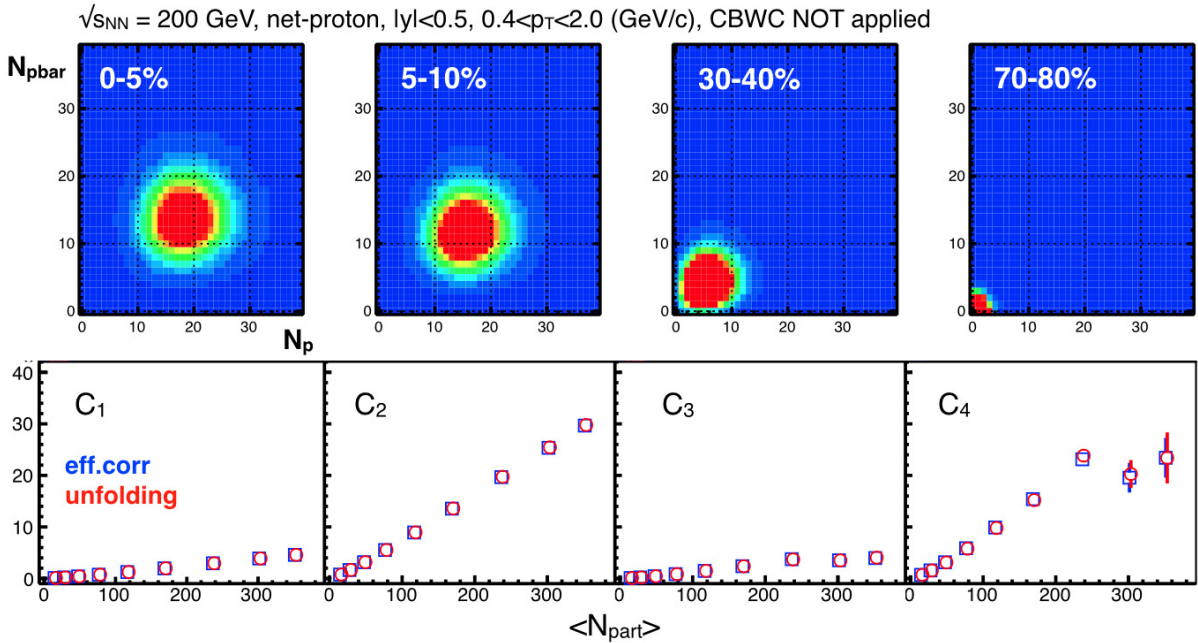


Figure 3.12: (Top) Unfolded distribution for protons and antiprotons at 0–5%, 5–10%, 30–40% and 70–80% centralities. (Bottom) Cumulants up to fourth order as a function of centrality. Blue squares are results of efficiency correction, and red circles are efficiency correction. Any volume fluctuation correction is not applied.

3.3 Embedding simulation

3.3.1 Single particle efficiency

Tracking efficiency of TPC can be estimated by embedding simulation. Embedding simulation is the MC approach, where we embed protons into real experimental data in detector level to see whether the embedded tracks can be reconstructed or not. By applying the same cuts in analysis to the embedded tracks, single track efficiency can be estimated. TOF matching efficiency are estimated according to the following equation by using the real experimental data:

$$\varepsilon_{\text{TOF}} = \frac{|n\sigma| < 2 \ \&\& \ \text{TOF matched}}{|n\sigma| < 2}. \quad (3.23)$$

Figure 3.13 shows the TPC tracking efficiency, TOF matching efficiency and combined efficiency at $0.8 < p_T < 2.0$ (GeV/c) for protons as a function of p_T for each centrality. Then we obtain the p_T

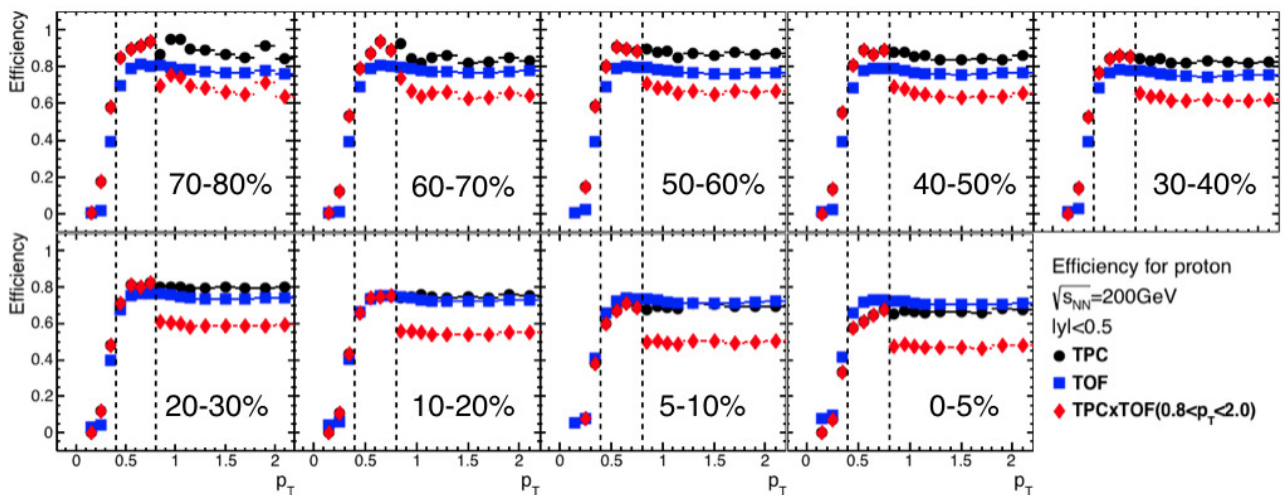


Figure 3.13: TPC tracking efficiency (black), TOF matching efficiency (blue) and combined efficiency at $0.8 < p_T < 2.0$ (GeV/c)(red) for protons as a function of p_T for each centrality.

integrated efficiency by using the following expression:

$$\varepsilon_{int} = \frac{\int \varepsilon(p_T) f(p_T) p_T dp_T}{\int f(p_T) p_T dp_T}, \quad (3.24)$$

where $f(p_T)$ are taken from the corrected p_T spectra for protons and antiprotons [40]. Figure 3.14 shows the p_T integrated efficiency for protons and antiprotons at $0.4 < p_T < 0.8$ (GeV/c) and $0.8 < p_T < 2.0$ (GeV/c) as a function of refmult3. Those data are fitted with polynomial function, which gives the value of refmult3 bin by bin efficiency.

In the net-proton analysis up to fourth order cumulant at the STAR experiment, four efficiency bins (low and high p_T , protons and antiprotons) have been implemented in the efficiency correction. It was found that TPC tracking efficiency depends on rapidity and azimuthal angles as well as p_T due to the fact that some TPC sectors can be in bad condition with electronic issues. Figure 3.15 shows the azimuthal and rapidity dependence of TPC tracking efficiency for protons in the 0–5% centrality. We see that the efficiency in sectors $-\pi/3 < \phi < 0$ are lower than others, which is also implemented in this study. Then the number of efficiency bins becomes eight including azimuthal dependence.

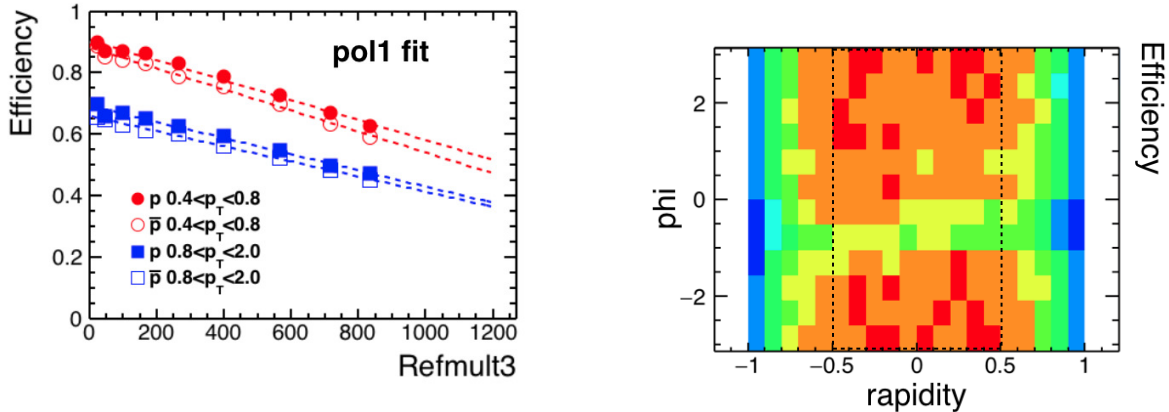


Figure 3.14: p_T integrated efficiency for protons (open) and antiprotons (filled) at $0.4 < p_T < 0.8$ GeV/c (red) and $0.8 < p_T < 2.0$ GeV/c (blue) 0–5% centrality as a function of azimuthal angles as a function of Refmult3. Dotted lines are polynomial fittings.

3.3.2 Efficiency distribution

Non-binomial distributions

By replacing the MC filter from binomial model to non-binomial model, we can see some scenarios how final results can be changed. We introduce two kinds of non-binomial distributions discussed in Ref. [41]. One is the hypergeometric distribution and the other one is the beta-binomial distribution. Former one has narrower width than binomial distribution, while the latter one has wider width. Definitions for these two distributions are following. Let us consider to determine the number of measured particles n from the true particles N with efficiency ε according to the hypergeometric distribution. Suppose an urn containing white and black balls. Number of those balls are denoted by N_w and N_b . We draw a ball from the urn, and count up n if it is white. This procedure is repeated with N times without throwing back to the urn. On the other hand, the beta-binomial distribution can be implemented similar manner but the previous procedure is repeated by returning two balls to the urn. Efficiency is determined by number of white and black balls as $\frac{1-\varepsilon}{\varepsilon} = \frac{N_b}{N_w}$. The deviation from binomial distribution can be implemented by another parameter α which determines the number of white balls. Figure 3.16 shows examples for hypergeometric and beta-binomial distributions. We assumed $N = 10$, $\varepsilon = 0.6$ and $N_w = 2\alpha N$. Different α parameters are shown in different colors. Binomial distribution is shown in black points. It can be found that smaller α gives narrower(wider) width for hypergeometric(beta-binomial) distributions, and it becomes close to binomial distribution with large α . This reflects the fact that the replacement or returning of balls will be irrelevant in the case of large number of white and black balls.

Modeling of the efficiency

We can model the response function extracted from the embedding datasets by fittings with binomial and non-binomial distributions, which will allow us to expect how much the efficiency can be non-binomial. Figure 3.17 shows the results of fittings to embedding datasets in 0–5% centrality at $1.0 < p_T < 2.0$ (GeV/c) by using the binomial, hypergeometric and beta-binomial distributions. Each panel shows different number of embedded protons, and the number of reconstructed protons are plotted in

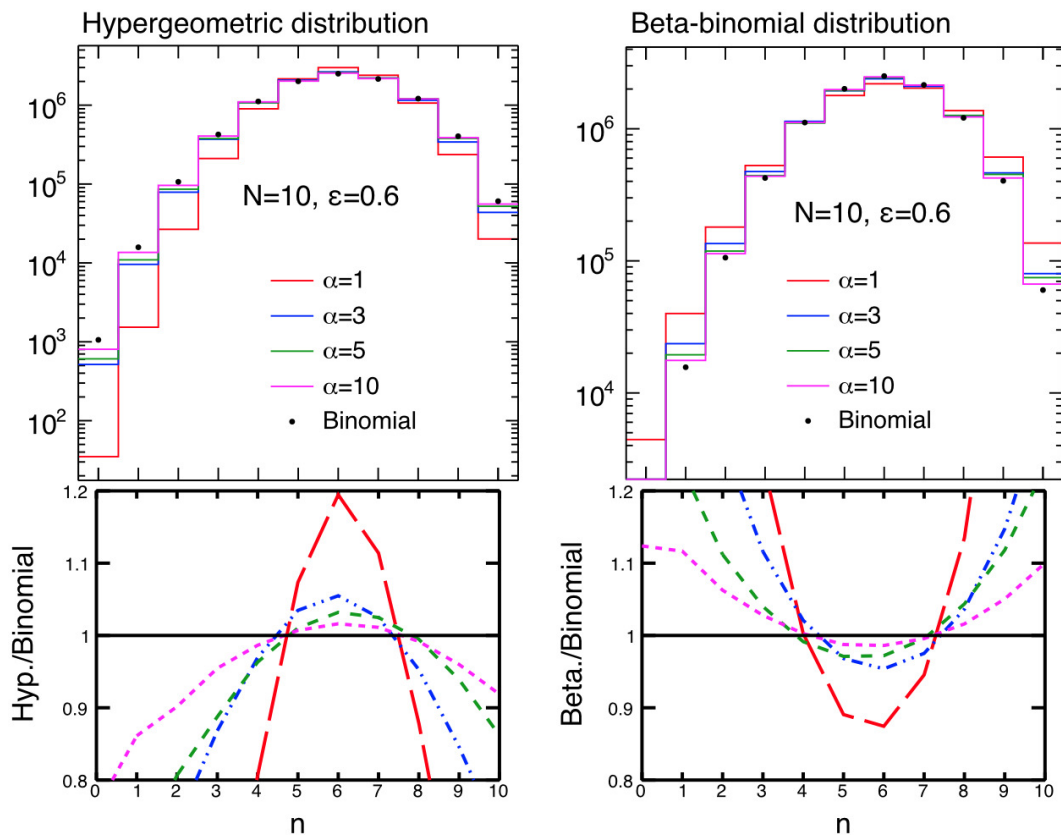


Figure 3.16: Hypergeometric and beta-binomial distributions with $N = 10$ and $\varepsilon = 0.6$. Distributions with different α are shown in different colors. Black points represent a binomial distribution. Bottom panels show the ratio to binomial.

black points. Lines in different colors represent the different fitting functions. Results of χ^2/NDF are shown in Fig. 3.18 as a function of number of embedded protons for different fitting functions. It can be found that the beta-binomial distribution is the best function to describe the embedding datasets followed by binomial and hypergeometric distributions. Fig. 3.19 shows the extracted α parameter by beta-binomial fittings as a function of the embedded (anti)protons, which is fitted by $y = a/x + b$ to extrapolate to the large number of embedded (anti)protons. These parameter a and b will be used as a part of systematic studies.

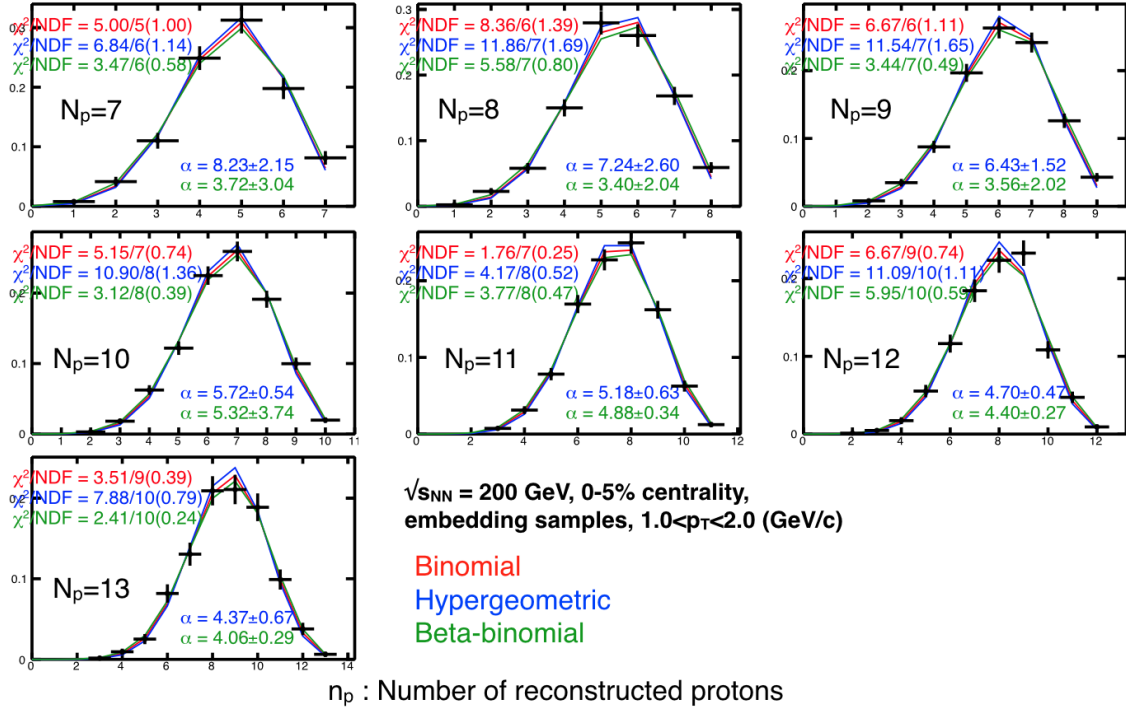


Figure 3.17: Number of reconstructed protons are plotted with different number of embedded protons from 7 to 13 in 0–5% centrality at $1.0 < p_T < 2.0$ (GeV/c), which are fitted by binomial (red), hypergeometric (blue) and beta-binomial (green) distributions. Fitting results for χ^2/NDF and α are also shown in each panel.

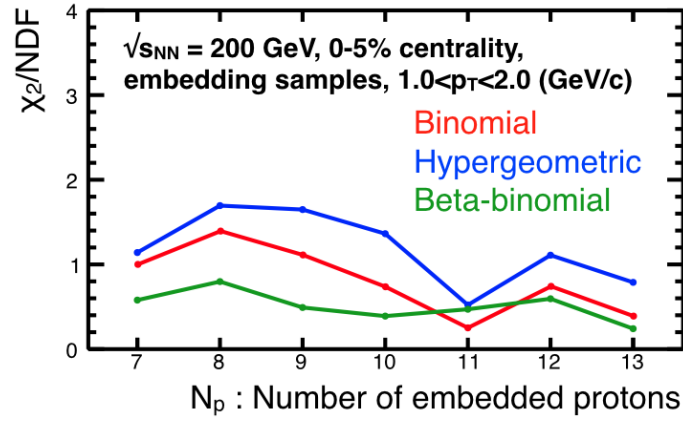


Figure 3.18: χ^2/NDF extracted from Fig. 3.17 as a function of number of embedded protons for binomial (red), hypergeometric (blue) and beta-binomial (green) fittings.

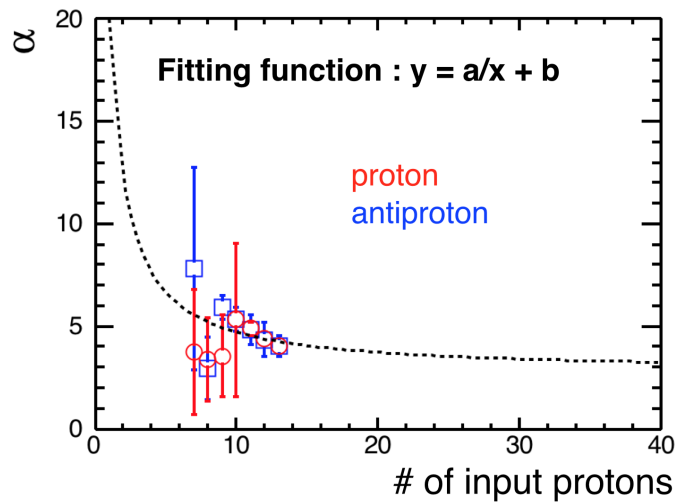


Figure 3.19: The non-binomial parameter α extracted from the beta-binomial fitting to the embedding data as a function of the number of input (anti)protons. Data points are fitted by $y = a/x + b$ to extrapolate to the large number of (anti)protons.

Chapter 4

Volume Fluctuation

Experimentally, the volume fluctuation effect needs to be addressed as backgrounds. Even in one centrality, two nuclei collides with different overlap volume or with different number of participant nucleons (N_{part}) event by event. Then the number of produced particles fluctuates due to the volume fluctuation, which directly affects the values of cumulants. In order to suppress the effect of the volume fluctuation, the STAR experiment has been using Centrality Bin Width Correction (CBWC). Recently, on the other hand, P. Braun-Munzinger. et al newly suggested a volume fluctuation correction (VFC) to eliminate the participant fluctuation with some model assumptions [42]. In this chapter, we discuss both CBWC and VFC. We compare both methods by using simple toy models, and show some important features.

4.1 Centrality Bin Width Correction (CBWC)

In this section, we note some important points on CBWC related to the centrality resolution and the auto-correlation effect using the UrQMD model [22]. Based on these points we can determine the best condition to define the centrality with volume fluctuation being substantially suppressed. Centrality definition is summarized in App. A.

4.1.1 Centrality Bin Width Correction (CBWC)

Centrality Bin Width Correction (CBWC) is defined as:

$$C_r = \sum_i \omega_i K_r^i, \quad (4.1)$$

$$\omega_i = \frac{n_i}{\sum_i n_i}, \quad (4.2)$$

where i denotes the i th multiplicity bin, K_r^i is the r th order cumulant in i th multiplicity bin, and n_i is the number of events in i th multiplicity bin. It can be found that CBWC depends on the multiplicity distribution used for the centrality definition. In other words, CBWC will be changed by the centrality resolution. Figure 4.1 shows $\kappa\sigma^2$ of net-proton distribution as a function of centrality with different rapidity coverage used for centrality determination. The value of $\kappa\sigma^2$ is artificially enhanced with narrow rapidity coverage for the centrality definition (bad centrality resolution), while $\kappa\sigma^2$ is suppressed to converge to certain value with large coverage for the centrality definition (good centrality resolution). This indicates that the better centrality resolution is required for better correction with CBWC, and thus we need to measure as large number of particles as possible for better centrality resolution better in the experiment.

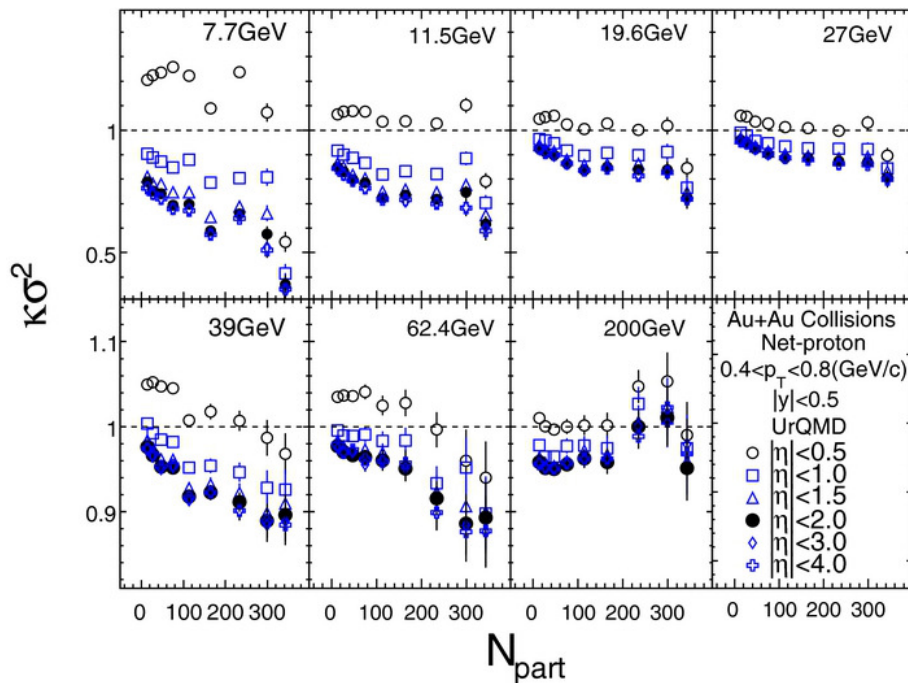


Figure 4.1: $\kappa\sigma^2$ (C_4/C_2) as a function of centrality with different rapidity coverage for centrality definition using UrQMD model [22].

4.1.2 Auto-correlation effect

Figure 4.2 shows the centrality dependence of $\kappa\sigma^2$ for net-proton distribution with BES energies with two sets of centrality definition, one uses all charged particles in $|\eta| < 2.0$ where protons used for cumulant analysis are included in the centrality determination, while the other uses charged kaons and pions in $|\eta| < 2.0$. We can see that the results for former case are suppressed compared to the latter case due to the auto-correlation effect, which becomes large in low beam energies, because the number of protons commonly used for cumulant analysis and the centrality determination becomes large due to the baryon stopping. Note that due to the resonance decay there are still some fractions of auto-correlation effect even if we define the centrality with pions and kaons excluding protons.

4.2 Volume Fluctuation Correction

As discussed in Sec. 4.1, CBWC has been studied with UrQMD model [22], where the conclusion is the CBWC results converge to certain value by increasing the centrality resolution, where we need to keep in mind the fact that CBWC results will not converge to the true cumulants even in UrQMD model. Recently new method for the volume fluctuation correction has been suggested in Ref. [42]. Although it needs some model inputs for correction factors, it has nice and important features compared to CBWC. In this section, we first derive the correction formulas. Then we perform a simple toy model calculation to show the validity of this method. Finally, we show an interesting feature of this method in view of the centrality resolution by using a toy model.

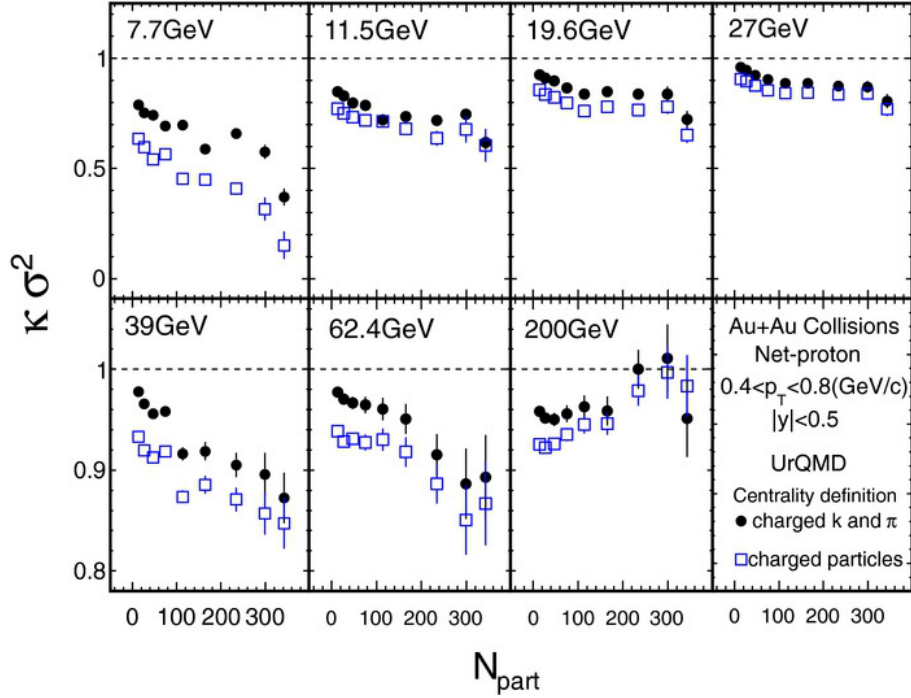


Figure 4.2: $\kappa\sigma^2$ (C_4/C_2) of net-proton distribution as a function of centrality with different centrality definition using UrQMD model [22].

4.2.1 Derivation

We assume that the independent particle productions of net-particle from the source of N_{pn} . Then r -th moment for each N_{pn} can be expressed as

$$\langle \Delta n^r \rangle = \left[\frac{d^r}{dt^r} M_{\Delta n}(t) \right]_{t=0}, \quad (4.3)$$

where Δn and $M_{\Delta n}$ denote the number of net-particle and the moment generating function for each N_{pn} . Due to the independent particle production model, a moment generating function for all source will be expressed by the product of the moment generating functions from each source as

$$M_{\Delta N}(t) = [M_{\Delta n}(t)]^{N_{\text{pn}}}, \quad (4.4)$$

where ΔN is the number of net-particle from all source $\Delta N = \Delta n \times N_{\text{pn}}$. Then r -th moment can be extracted by r derivatives on the moment generating function. The first and second order moments are obtained as

$$\langle \Delta N \rangle = \sum_{N_{\text{pn}}} P(N_{\text{pn}}) \left[\frac{dM_{\Delta N}(t)}{dt} \right]_{t=0} \quad (4.5)$$

$$= \sum_{N_{\text{pn}}} P(N_{\text{pn}}) \left[N_{\text{pn}} [M_{\Delta n}(t)]^{N_{\text{pn}}-1} \frac{dM_{\Delta n}(t)}{dt} \right]_{t=0} = \langle N_{\text{pn}} \rangle \langle \Delta n \rangle, \quad (4.6)$$

$$\langle \Delta N^2 \rangle = \sum_{N_{\text{pn}}} P(N_{\text{pn}}) \left[\frac{d^2 M_{\Delta N}(t)}{dt^2} \right]_{t=0} = \langle N_{\text{pn}}(N_{\text{pn}} - 1) \rangle \langle \Delta n \rangle^2 + \langle N_{\text{pn}} \rangle \langle \Delta n^2 \rangle, \quad (4.7)$$

where we apply additional summation over the probability distribution of participant nucleons $P(N_{\text{pn}})$ to consider the fluctuating number of N_{pn} . Once we obtain moments up to fourth order, they are converted to cumulants:

$$\langle \Delta N \rangle_c = \langle N_{\text{pn}} \rangle \langle \Delta n \rangle, \quad (4.8)$$

$$\langle \Delta N^2 \rangle_c = \langle N_{\text{pn}} \rangle \langle \Delta n^2 \rangle_c + \langle \Delta n \rangle^2 \langle N_{\text{pn}}^2 \rangle_c, \quad (4.9)$$

$$\langle \Delta N^3 \rangle_c = \langle N_{\text{pn}} \rangle \langle \Delta n^3 \rangle_c + 3 \langle \Delta n \rangle \langle \Delta n^2 \rangle_c \langle N_{\text{pn}}^2 \rangle_c + \langle \Delta n \rangle^3 \langle N_{\text{pn}}^3 \rangle_c, \quad (4.10)$$

$$\begin{aligned} \langle \Delta N^4 \rangle_c &= \langle N_{\text{pn}} \rangle \langle \Delta n^4 \rangle_c + 4 \langle \Delta n \rangle \langle \Delta n^3 \rangle_c \langle N_{\text{pn}}^2 \rangle_c + 3 \langle \Delta n^2 \rangle_c^2 \langle N_{\text{pn}}^2 \rangle_c \\ &\quad + 6 \langle \Delta n \rangle^2 \langle \Delta n^2 \rangle_c \langle N_{\text{pn}}^3 \rangle_c + \langle \Delta n \rangle^4 \langle N_{\text{pn}}^4 \rangle_c. \end{aligned} \quad (4.11)$$

Since we can calculate $\langle \Delta N^r \rangle_c$ from the experimental data and $\langle N_{\text{pn}}^r \rangle_c$ can be determined by some models like Glauber, cumulants for each source $\langle \Delta n^r \rangle$ are iteratively extracted from the first to r -th order cumulant. Cumulants for all source are obtained as

$$\langle \Delta N^r \rangle_c = \langle N_{\text{pn}} \rangle \langle \Delta n^r \rangle_c, \quad (4.12)$$

due to the assumption of independent source of participant nucleons. However, such derivation in terms of cumulants for net-particles and participant nucleons becomes complicated and cumbersome because of the conversions of explicit terms from moments to cumulants. In order to derive formulas up to sixth order cumulant, thus we introduce factorial moments for participant nucleons f_r and moments for net-particles from each source $\mu_r = \langle \Delta n^r \rangle$ because terms related to participant nucleons always appear as factorial moments as are seen in the first term in the right hand side in Eq. (4.7). Measured moments up to sixth order can be expressed as

$$\langle \Delta N \rangle = f_1 \mu_1, \quad (4.13)$$

$$\langle \Delta N^2 \rangle = f_2 \mu_1^2 + f_1 \mu_2, \quad (4.14)$$

$$\langle \Delta N^3 \rangle = f_3 \mu_1^3 + 3 f_2 \mu_1 \mu_2 + f_1 \mu_3, \quad (4.15)$$

$$\langle \Delta N^4 \rangle = f_4 \mu_1^4 + 6 f_3 \mu_1^2 \mu_2 + 3 f_2 \mu_2^2 + 4 f_2 \mu_1 \mu_3 + f_1 \mu_4, \quad (4.16)$$

$$\langle \Delta N^5 \rangle = f_5 \mu_1^5 + 10 f_4 \mu_1^3 \mu_2 + 15 f_3 \mu_1 \mu_2^2 + 10 f_3 \mu_1^2 \mu_3 + 10 f_2 \mu_2 \mu_3 + 5 f_2 \mu_1 \mu_4 + f_1 \mu_5, \quad (4.17)$$

$$\begin{aligned} \langle \Delta N^6 \rangle &= f_6 \mu_1^6 + 15 f_5 \mu_1^4 \mu_2 + 45 f_4 \mu_1^2 \mu_2^2 + 15 f_3 \mu_3^2 + 20 f_4 \mu_1^3 \mu_3 + 60 f_3 \mu_1 \mu_2 \mu_3 + 10 f_2 \mu_3^2 \\ &\quad + 15 f_3 \mu_1^2 \mu_4 + 15 f_2 \mu_2 \mu_4 + 6 f_2 \mu_1 \mu_5 + f_1 \mu_6. \end{aligned} \quad (4.18)$$

Moments from each source can be obtained up to sixth order by resolving Eqs.(4.13)–(4.18) iteratively. After we convert them to cumulants from each source, corrected cumulants are obtained by Eq. (4.12). Correction formulas more than fourth order cumulants are given by

$$\begin{aligned} \langle \Delta N^5 \rangle_c &= \langle N_{\text{pn}} \rangle \kappa_5(\Delta n) + \left[5 \kappa_4(\Delta n) \kappa_1(\Delta n) + 10 \kappa_3(\Delta n) \kappa_2(\Delta n) \right] \kappa_2(N_{\text{pn}}) \\ &\quad + \left[10 \kappa_3(\Delta n) \kappa_1^2(\Delta n) + 15 \kappa_2^2(\Delta n) \kappa_1(\Delta n) \right] \kappa_3(N_{\text{pn}}) + 10 \kappa_2(\Delta n) \kappa_1^3(\Delta n) \kappa_4(N_{\text{pn}}) \\ &\quad + \kappa_1^5(\Delta n) \kappa_5(N_{\text{pn}}), \end{aligned} \quad (4.19)$$

$$\begin{aligned} \langle \Delta N^6 \rangle_c &= \langle N_{\text{pn}} \rangle \kappa_6(\Delta n) + \left[6 \kappa_5(\Delta n) \kappa_1(\Delta n) + 15 \kappa_4(\Delta n) \kappa_2(\Delta n) + 10 \kappa_3^2(\Delta n) \right] \kappa_2(N_{\text{pn}}) \\ &\quad + \left[15 \kappa_4(\Delta n) \kappa_1^2(\Delta n) + 60 \kappa_3(\Delta n) \kappa_2(\Delta n) \kappa_1(\Delta n) + 15 \kappa_2^3(\Delta n) \right] \kappa_3(N_{\text{pn}}) \\ &\quad + \left[20 \kappa_3(\Delta n) \kappa_1^3(\Delta n) + 45 \kappa_2^2(\Delta n) \kappa_1^2(\Delta n) \right] \kappa_4(N_{\text{pn}}) + 15 \kappa_2(\Delta n) \kappa_1^4(\Delta n) \kappa_5(N_{\text{pn}}) \\ &\quad + \kappa_1^6(\Delta n) \kappa_6(N_{\text{pn}}), \end{aligned} \quad (4.20)$$

which can be easily derived by using cumulant expansion technique [43].

4.2.2 Toy model

The setup is following. We make the multiplicity distribution by using the Glauber and two component, and define the centrality using the multiplicity distribution. For proton productions, we tried two cases. In one case, protons and antiprotons are generated from event by event N_{part} determined by Glauber model. In the other case, N_{part} is fixed to the averaged value in one centrality. Figure 4.3 shows the net-proton distribution for two cases, and their ratios at each 0–5, 20–30 and 70–80% centralities. It can be found that the shape of the net-proton distributions are affected by participant fluctuations. Cumulants up to fourth order are shown in Fig. 4.4. For black circles N_{part} fluctuates which includes participant fluctuation given by the Glauber model For red squares N_{part} is fixed, which are true value of cumulant in this model. Black solid lines are results of VFC, and blue crosses are results of CBWC. We see that VFC results gives the true value of cumulants up to fourth order. For CBWC, however, there are still some fractions of volume fluctuations compared to the true values for C_3 and C_4 .

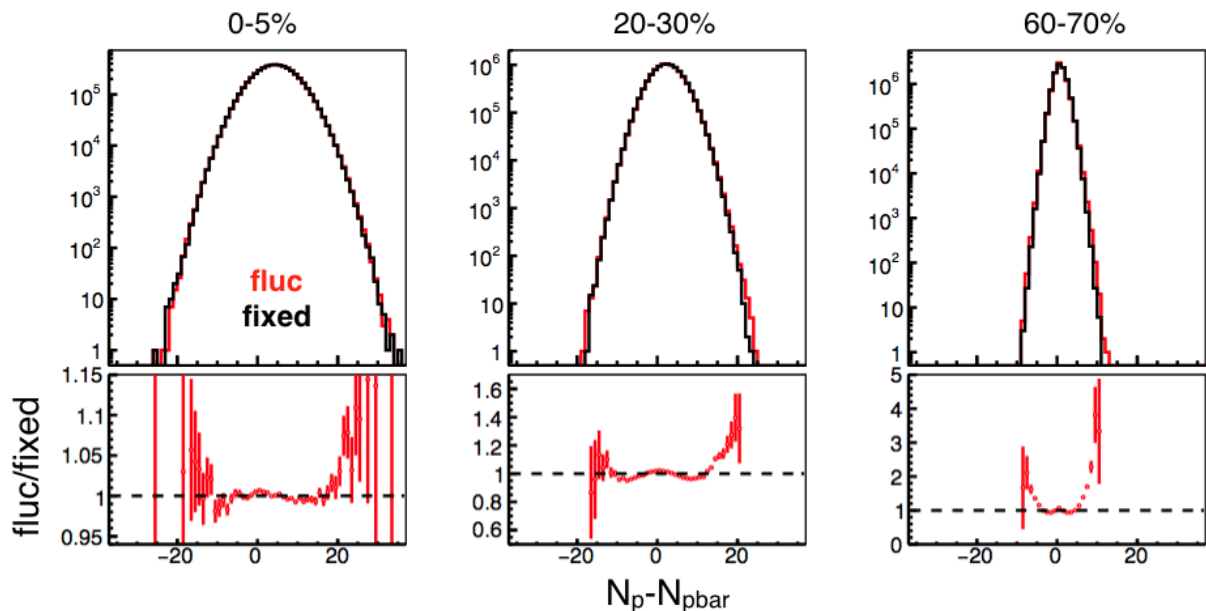


Figure 4.3: Upper panel shows the net-proton distributions at 0–5, 20–30 and 60–70% centralities. N_{part} fluctuates according to the Glauber model for red lines, while N_{part} is fixed in black lines. Lower panels show the ratio between two net-proton distributions.

4.3 CBWC vs VFC

4.3.1 Centrality resolution effect

As discussed in Sec. 4.1, CBWC depends on the centrality resolution. In order to see how VFC behaves with respect to the centrality resolution, we performed a simple toy model calculation. Although the setup for the toy model is mostly the same with Sec. 4.2.2, three multiplicity distributions are defined which have different centrality resolutions as shown in Fig. 4.4, where we defined the red multiplicity distribution as 100% centrality resolution, then multiplicity distributions which have 50% (blue) and 20% (green) centrality resolution were generated by random sampling from the multiplicity distribution with 100% centrality resolution. We apply both CBWC and VFC in these three cases of

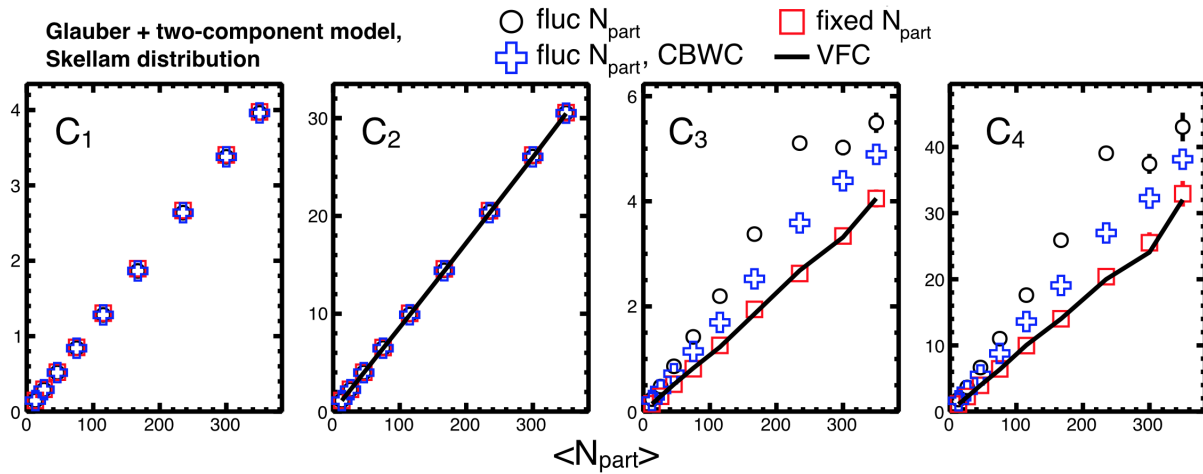


Figure 4.4: Cumulants up to fourth order as a function of centrality. For black circles N_{part} fluctuates which includes participant fluctuation given by the Glauber model. For red squares N_{part} is fixed, which are true value of cumulant in this model. Black solid lines are results of VFC, and blue crosses are results of CBWC.

centrality resolution, then compare results between two methods and different centrality resolution. Results are shown in the right hand side panels in Fig. 4.5. It can be found that the results of C_3 and C_4 without CBWC nor VFC and with CBWC are both enhanced by reducing the centrality resolution. On the other hand, VFC results does not depend on the centrality resolution and give true value of cumulants.

4.3.2 UrQMD model

Based on the discussions so far, let me summarize the merits and demerits for CBWC and VFC as followings. CBWC can suppress the volume fluctuation without any model assumption, but it depends on the centrality resolution. On the other hand, VFC can eliminate the volume fluctuation, but it requires some model assumptions. We start from the Glauber model and assume the independent particle production model. In real experiments, however, the centrality resolution depends on the detectors used for the centrality determination, and the independent particle production model could be possibly broken, since lots of results from the heavy ion colliding experiments cannot be explained by the superposition of p+p collisions. Therefore, both CBWC and VFC would never provide true cumulants. Then the question is which correction will more closer to the true cumulants than the other. In order to obtain some hints for this question, the UrQMD data has been analyzed. The UrQMD is an event generator that are tuned to reproduce single particle distributions measured in heavy ion colliding experiments. The independent particle production model is expected to be broken in UrQMD, therefore the comparison between CBWC and VFC will be better test compared to previous models. In addition, we can define true cumulants by using the information on the event by event N_{part} given by UrQMD. The centrality is defined by using pions and kaons in $|\eta| < 1.0$ as shown in Fig. 4.6-(a). Protons and antiprotons in $0.4 < p_T < 2.0$ GeV/c and $|y| < 0.5$ are used for the cumulant analysis. Figure 4.6-(b) shows the event by event N_{part} distribution given by UrQMD for each centrality. The two-dimensional distributions in N_p and N_{pbar} at $N_{\text{part}} = 240$ are shown in Fig. 4.6-(c) and (d) for 10-20 and 0-10% centrality, respectively. Then we can calculate cumulants at each N_{part} bin in different centralities. Taking average of cumulants for each N_{part} bin in one

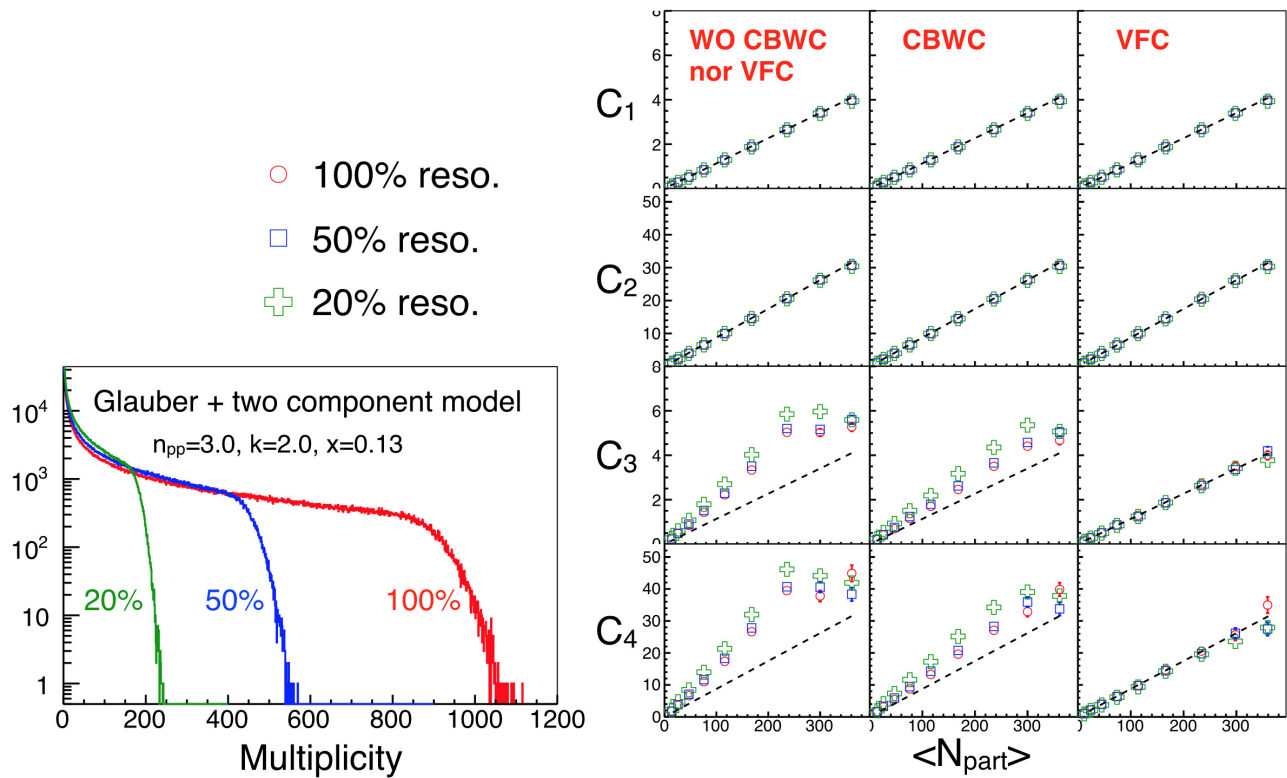


Figure 4.5: (Left) Multiplicity distributions with 100% (red), 50% (blue) and 20% (green) centrality resolution generated by Glauber and two component model. Distributions with 50% and 20% centrality resolution were defined by random sampling from the distribution with 100% resolution. (Right) Results up to fourth order cumulant as a function of centrality without CBWC nor CBWC, with CBWC and with VFC from left to right. Dotted lines represent the true cumulants.

centrality provides exactly the true cumulants in view of the participant fluctuation. This method corresponds to the CBWC on N_{part} . In order to distinguish this method with the conventional CBWC on the multiplicity distribution, I name both methods as CBWC-N and CBWC-M, respectively. The UrQMD data has been analyzed with CBWC-N, CBWC-M and VFC. For VFC, the multiplicity distribution in Fig. 4.6–(a) is fitted by the Glauber and two-component model to extract the N_{part} distribution and its cumulants, as is done in the experiment, instead of using the event by event N_{part} distribution given by UrQMD. The results from these three methods are shown in Fig. 4.7 for up to sixth order cumulant as a function of centrality. The cumulant ratios and the ratios of CBWC-M and VFC to CBWC-N are shown in Fig. 4.8. It can be found that the both CBWC-M and VFC don't provide the true cumulants (CBWC-N) as expected. Therefore for the final analysis of C_6/C_2 in the experimental data, the both methods CBWC-M and VFC have been adopted.

In order to calculate the true cumulants defined as CBWC-N, we need to know event by event N_{part} . One idea is to know the event by event N_{part} is to measure the spectator nucleons. But this is impossible in the collider experiments since we can only measure a part of the fragments of spectator nucleons by ZDC. On the other hand, however, it might be possible in the fixed-target experiment, where all spectators can be measured by ZDC in principle. If the ZDC resolution is high enough to measure the energy of spectators with unit nucleons, the true cumulants will be achieved without any assumptions.

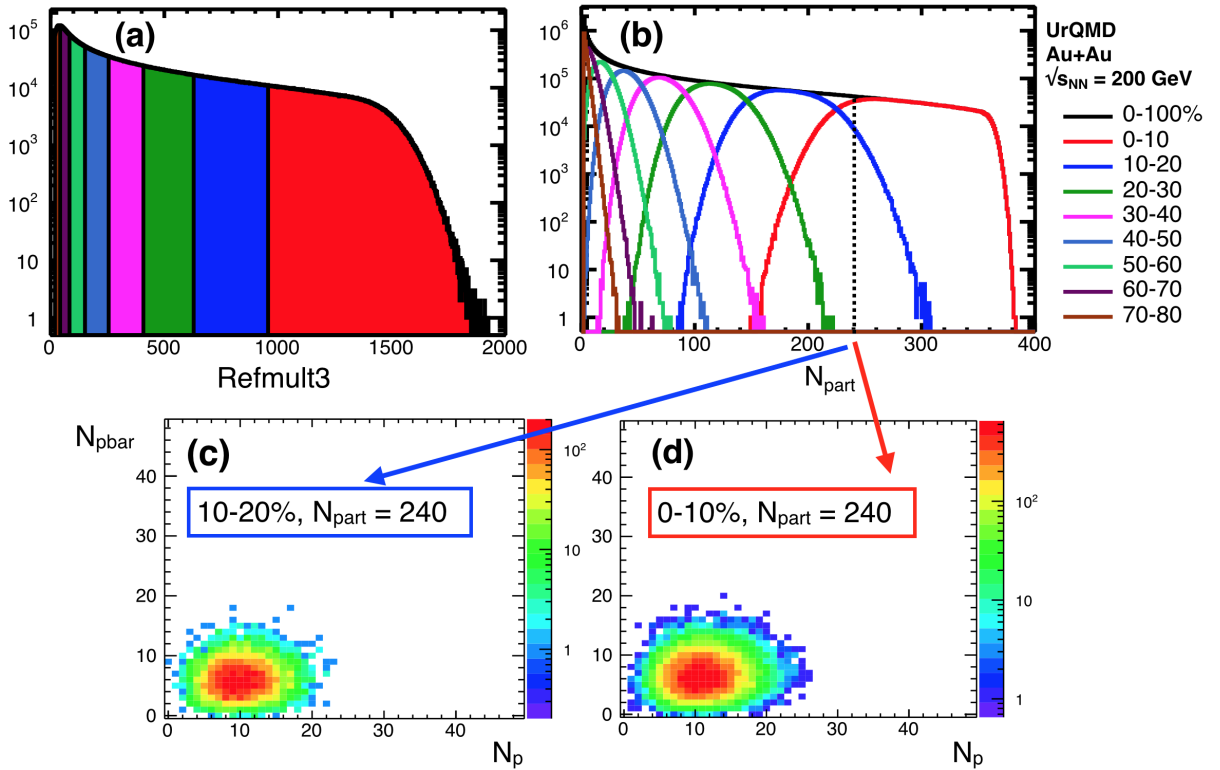


Figure 4.6: (a) The refmult3 distribution and (b) the N_{part} distribution, where the colors represent the different centralities. (c) and (d) show the two-dimensional histogram for N_p and N_{pbar} at $N_{\text{part}} = 240$ in 10-20 and 0-10% centralities.

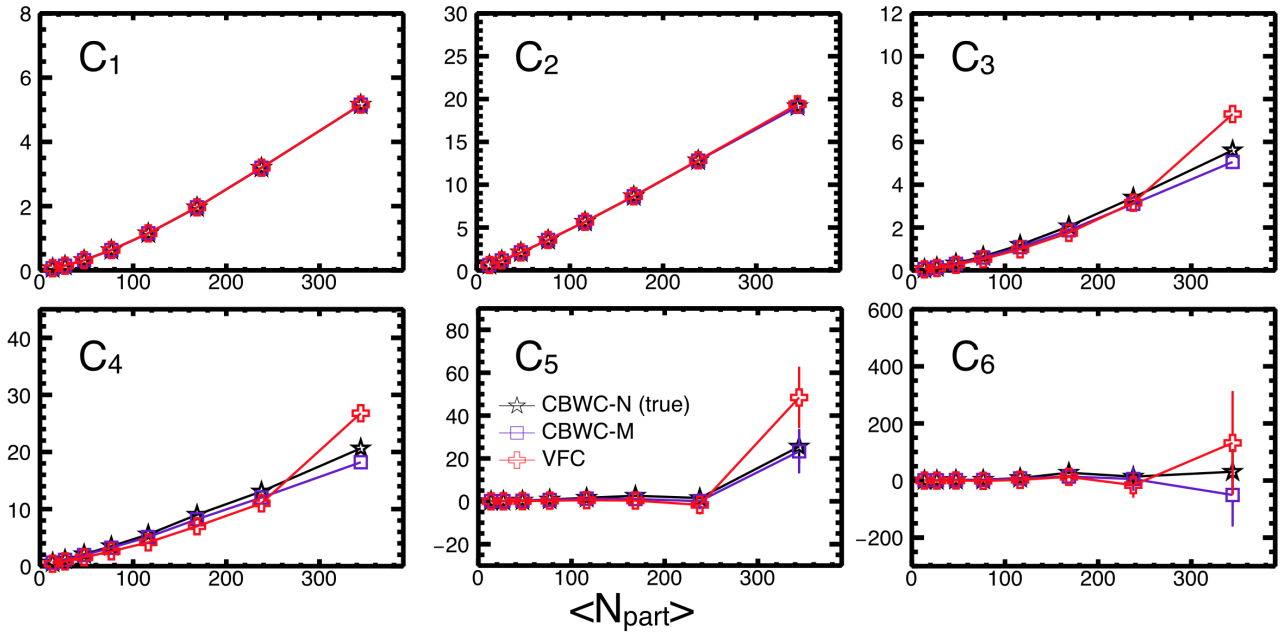


Figure 4.7: Cumulants up to sixth order as a function of centrality for CBWC-N (true), CBWC-M and VFC.

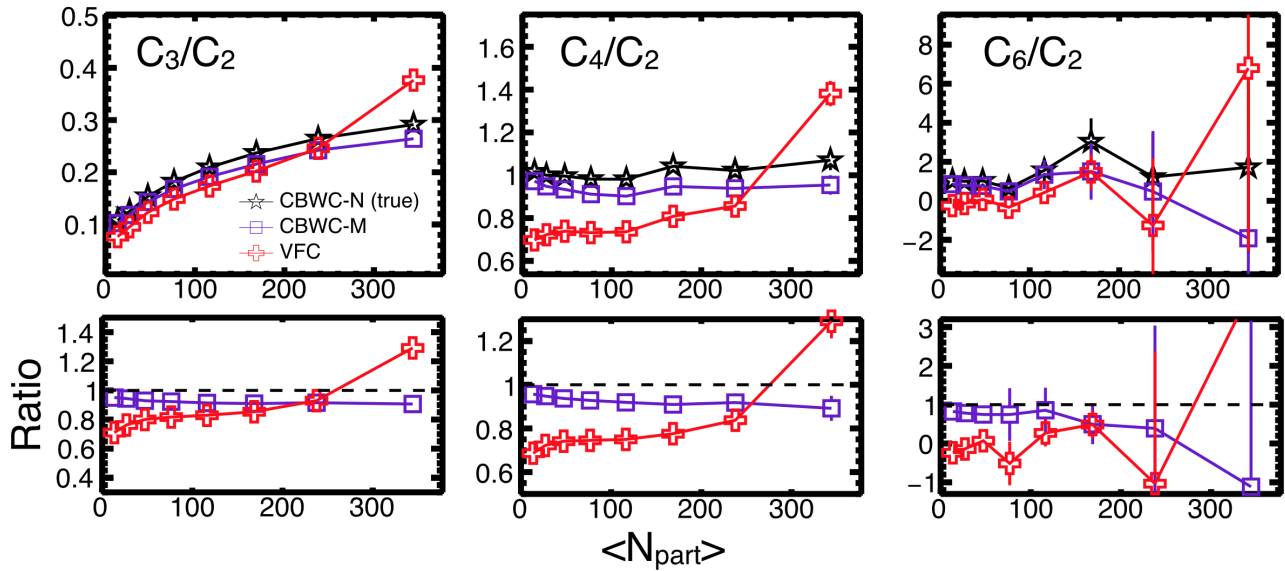


Figure 4.8: C_3/C_2 , C_4/C_2 and C_6/C_2 as a function of centrality for CBWC-N (true), CBWC-M and VFC. The ratios of CBWC-M and VFC to CBWC-N are shown in bottom panels.

Chapter 5

Results and Discussions

5.1 Systematic uncertainties

The systematic studies has been done by changing the cut variables and the value of efficiency used for the efficiency correction, and applying the unfolding with the beta-binomial model, which are summarized in Tab. 5.1. First, the unfolding with beta-binomial model has been performed. As the unfolding method are incompatible with CBWC, the results of the efficiency correction and unfolding are compared without any volume fluctuation corrections, which is shown in Fig 5.1. It is found that the unfolding results are consistent with the efficiency correction within statistical errors. The non-binomial detector effects on C_6/C_2 is thus negligible. The systematic uncertainties are estimated by changing parameters for PID cuts, track quality cuts, pileup rejection, and the efficiency correction. Loosening the $n\sigma_p$ and m^2 cuts worsen purity of protons and antiprotons, and decreases kaon contaminations. Requirement of small value of nHitsFit will increase the fraction of track splittings. Large DCA cut value will increase secondary protons. Pileup events are included by loosening the slope in a plane of the number of tofmatched tracks and Refmult. The values used in the efficiency correction are changed $\pm 5\%$ separately and simultaneously for low and high p_T regions. Finally, the systematic uncertainties are estimated by following formulas:

$$\sigma_{sys} = (C_6/C_2)_{def} \sqrt{\sum_j R_j^2}, \quad R_j = \sqrt{\frac{1}{n} \sum_i \left[\frac{(C_6/C_2)_{i,j} - (C_6/C_2)_{def}}{(C_6/C_2)_{def}} \right]^2}, \quad (5.1)$$

where $(\frac{C_6}{C_2})_{def}$ represents the results with the default cuts, and $(\frac{C_6}{C_2})_i$ represents i th change of the cut on j th variable.

Variable	Default cut	Changed cut	effect
$n\sigma_p$	< 2.0	< 2.5	worse purity
m^2	$0.6 < m^2 < 1.2$	$0.7 < m^2 < 1.3$ $0.8 < m^2 < 1.4$	decreases kaon contaminations
nHitsFit	> 20	> 15	increases track splittings
DCA	< 1.0	< 1.5	increases secondary protons
$n\text{TofMatch} = a \times \text{Refmult} + b$ $n\text{TofMatchBeta} = c \times \text{Refmult} + d$	$(a, b, c, d) = (0.5, -13, 0.46, -10)$	$(0.25, -13, 0.46, -10)$ $(0.50, -13, 0.23, -10)$ $(0, 0, 0, 0)$	increases pileup events
Efficiency	$(\varepsilon_{\text{lowpT}}, \varepsilon_{\text{highpT}})$	$(1.05 \times \varepsilon_{\text{lowpT}}, 1.05 \times \varepsilon_{\text{highpT}})$ $(0.95 \times \varepsilon_{\text{lowpT}}, 0.95 \times \varepsilon_{\text{highpT}})$ $(1.05 \times \varepsilon_{\text{lowpT}}, 0.95 \times \varepsilon_{\text{highpT}})$ $(0.95 \times \varepsilon_{\text{lowpT}}, 1.05 \times \varepsilon_{\text{highpT}})$	N/A
Detector model	Binomial	Beta-binomial	correct the non-binomial detector efficiency

Table 5.1: Summary of the systematic checks.

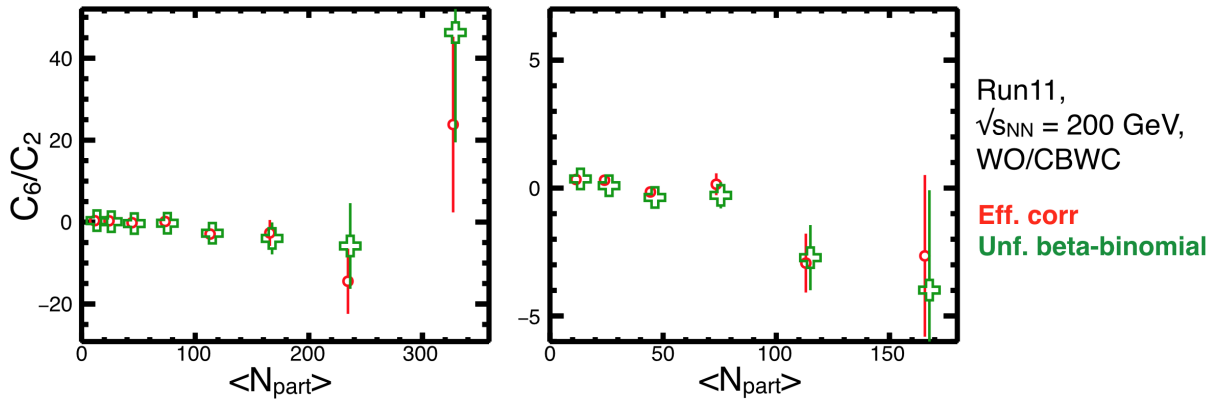


Figure 5.1: Centrality dependence of C_6/C_2 in Run11 without any volume fluctuation corrections. Results from the efficiency correction are shown in red circles, and results from the unfolding with the beta-binomial model are shown in green crosses.

5.2 Up to 4th order cumulants

Before the discussing the sixth order cumulant, let us compare results up to fourth order cumulant between CBWC and VFC. Figure 5.2 shows the cumulants up to fourth order as a function of centrality without CBWC nor VFC, with VFC and with CBWC. In the former two cases, results with different centrality bin width of 8bin, 16bin and 32bin (corresponding to 2.5%, 5.0% and 10% centrality step) are shown. It can be found that C_3 and C_4 in VFC results seems artificially suppressed at central collisions with 8bin centrality class, while they become smooth and converge to certain value with small centrality bin width of 16bin and 32bin. At first glance, it seems interesting because such centrality dependence is not observed in a toy model, and one might expect some physics in experimental data. However, it can be simply explained by multiplicity dependent efficiency. According to the analytical calculations in Ref. [41], if the averaged efficiency is used under the situation of multiplicity dependent efficiency, cumulants are artificially suppressed than they should be. One does know the fact that the efficiency depends on multiplicity as shown in Fig. 3.14. As was noted, the efficiency correction is applied using the averaged efficiency in one centrality, then subtract the participant fluctuations. This is exactly the case discussed in Ref. [41], which indicates that the results of C_3 and C_4 without CBWC or VFC shown in Fig. 5.2 are artificially suppressed. One can expect that such effect from multiplicity dependent efficiency becomes small with narrow centrality bin width, because efficiency variations will be reduced. Then the observed convergence of VFC results for C_3 and C_4 with 16bin and 32bin centrality classes is consistent with the expectation, and it indicates that the effect of multiplicity dependent efficiency becomes negligible with those centrality bin width.

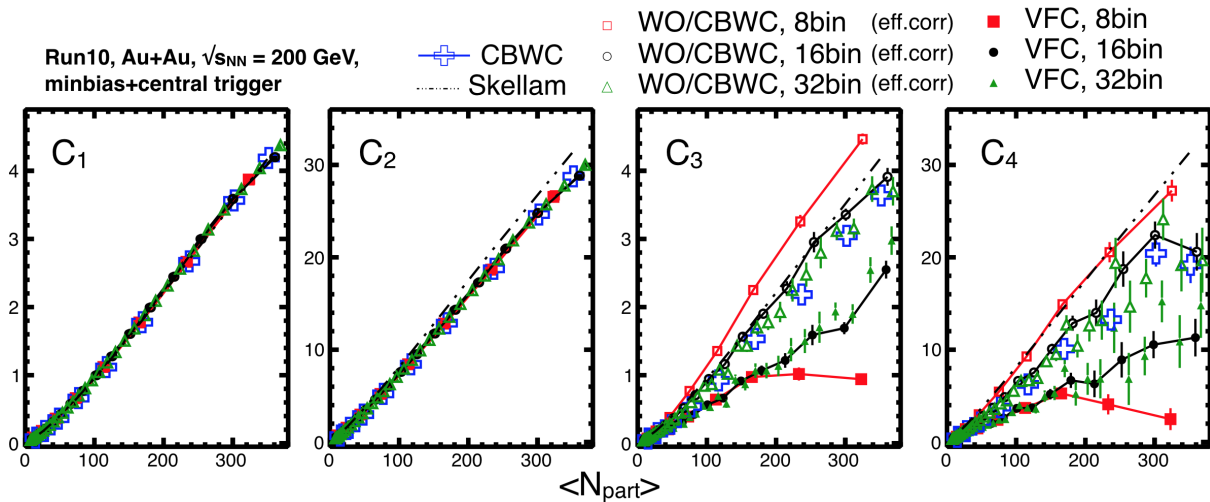


Figure 5.2: Cumulants up to fourth order as a function of centrality using the experimental data. Results without CBWC nor VFC, with VFC and with CBWC. In the former two cases, results with different centrality bin width of 8bin, 16bin and 32bin (corresponding to 2.5%, 5.0% and 10% centrality step) are shown.

Next, in order to see how much the STAR preliminary results on 3rd and 4th order fluctuations could be changed by using VFC instead of CBWC, datasets at $\sqrt{s_{NN}} = 7.7, 19.6$ and 62.4 GeV have been analyzed as well as 200 GeV. Figure 5.3 shows the centrality dependence of C_3/C_2 normalized by the value of Skellam and C_4/C_2 at different beam energies. It can be found that VFC results of $(C_3/C_2)/\text{Skellam}$ are systematically suppressed compared to CBWC in all centralities. The differences between CBWC and VFC seem large in mid-central collisions, and small in peripheral and central

collisions, which is consistent with results of the toy model in Fig. 4.4. This trend of downward convex in the centrality dependence changes to flat in high beam energy. For C_4/C_2 , results are consistent between CBWC and VFC in central collisions at $\sqrt{s_{\text{NN}}} = 7.7, 19.6$ and 62.4 GeV. Next, let us discuss the difference between the VFC results and the current STAR preliminary results. In Fig. 5.4, the VFC results are superimposed to the STAR preliminary results of beam energy dependence of C_4/C_2 and $S\sigma/\text{Skellam} = (C_3/C_2)/\text{Skellam}$ in 0-5, 5-10 and 70-80% centralities [23]. It can be found that the VFC results of $\kappa\sigma^2$ are consistent with preliminary results within errors in 0-5 and 5-10% centralities. The conclusion of non-monotonic behaviour in the beam energy dependence of $\kappa\sigma^2$ would be thus robust to the method for the volume fluctuation correction. However, large differences are observed in $S\sigma/\text{Skellam}$ and in 70-80% centrality of $\kappa\sigma^2$. Further understandings on the volume fluctuations would be necessary to interpret these differences.

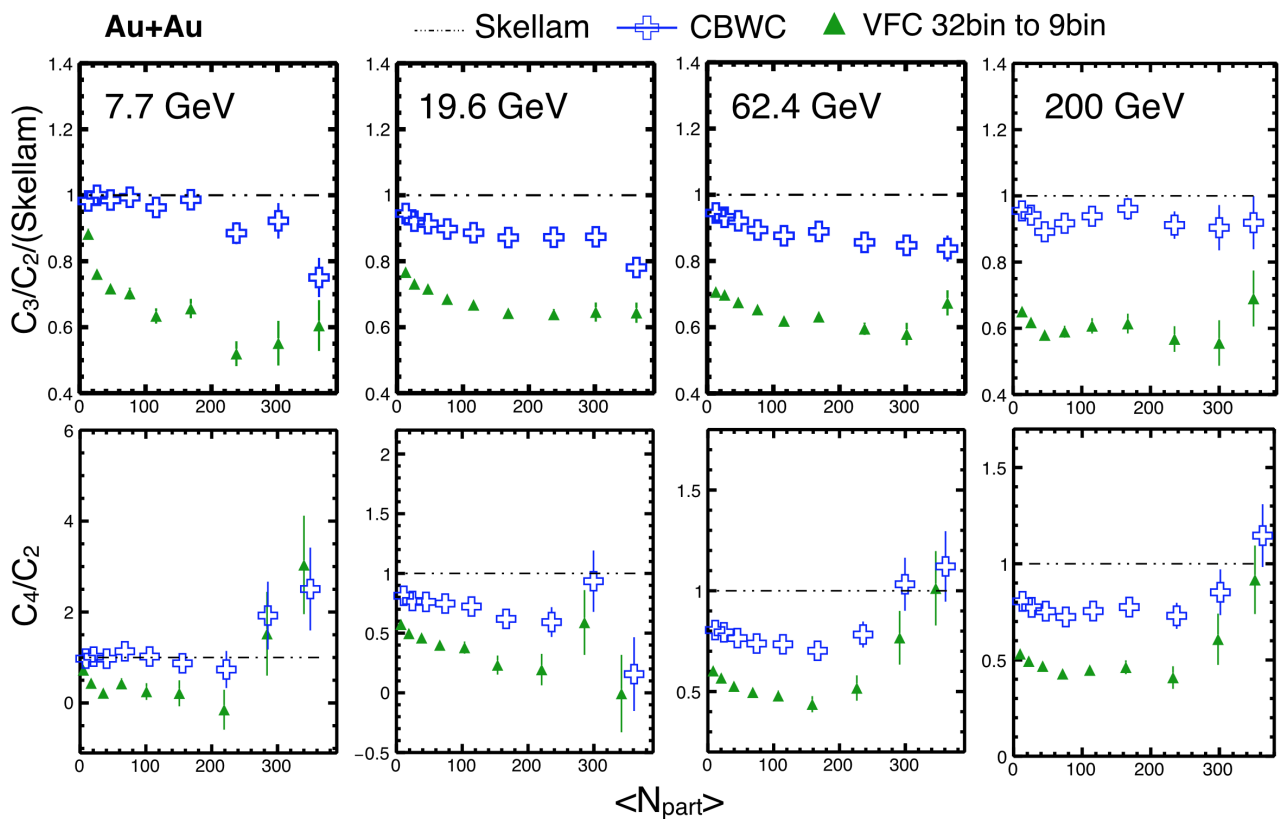


Figure 5.3: The centrality dependence of C_3/C_2 normalized by the value of Skellam (top) and C_4/C_2 (bottom) at $\sqrt{s_{\text{NN}}} = 7.7, 19.6, 62.4$ and 200 GeV. Results using CBWC are shown in blue crosses, and VFC results are shown in green triangles. The Skellam baselines are shown in dotted lines.

5.3 6th order fluctuation

First, the Run10 and Run11 datasets are analyzed separately, and checked the consistency. Figure 5.5 shows the centrality dependence of C_6/C_2 for Run10 and Run11, where the efficiency correction and CBWC are applied. Due to the huge errors in central collisions, the expanded plot is shown in right hand side from 20% centrality. It can be found that they are mostly consistent within errors except 40-50% centrality that would be the statistical fluctuation. Then the both results are merged to reduce

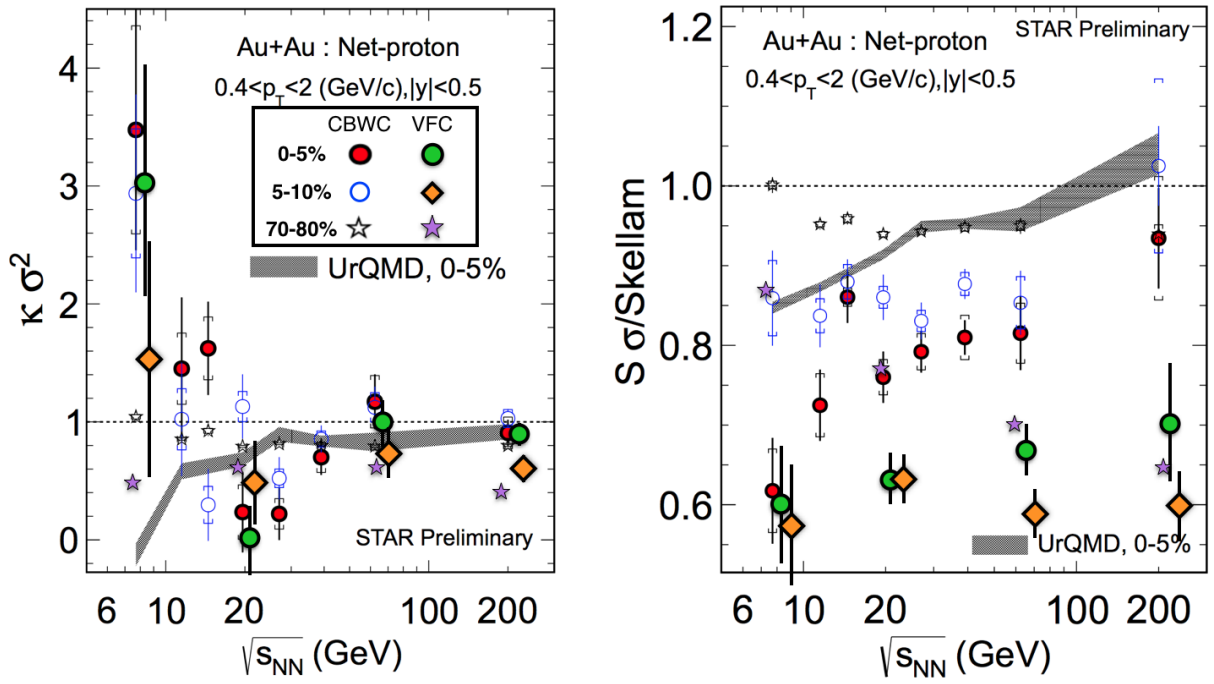


Figure 5.4: The STAR preliminary results on the beam energy dependence of $\kappa \sigma^2 = C_4/C_2$ and $S \sigma / \text{Skellam} = (C_3/C_2) / \text{Skellam}$ using CBWC [23], where VFC results at $\sqrt{s_{NN}} = 7.7, 19.6$ and 62.4 and 200 GeV are superimposed in green circles, orange diamonds and purple stars for 0-5, 5-10 and 70-80% centralities, respectively.

errors, which is shown in Fig. 5.6 with Skellam and the binomial baselines. It is found that the results are systematically smaller than Skellam baseline, and mostly consistent with the binomial expectation. It is natural for the binomial expectation can explain the results better than Skellam baseline since the binomial distribution has two parameters while Skellam has one. One can see that the experimental data is closer to the binomial distribution than Skellam distribution. In central collisions, however, results are still systematically suppressed compared to the binomial expectation. Since the results contain the baryon stopping effect which is known to lead to the suppression with respect to the Skellam baseline, one should compare the results with UrQMD model. CBWC is applied in UrQMD model as is done in the experimental data, which is shown in Fig. 5.7 in purple band. It can be found that the results of UrQMD is systematically suppressed than the Skellam baseline, which can be understood by the baryon stopping effect. But the experimental results still show smaller results than UrQMD.

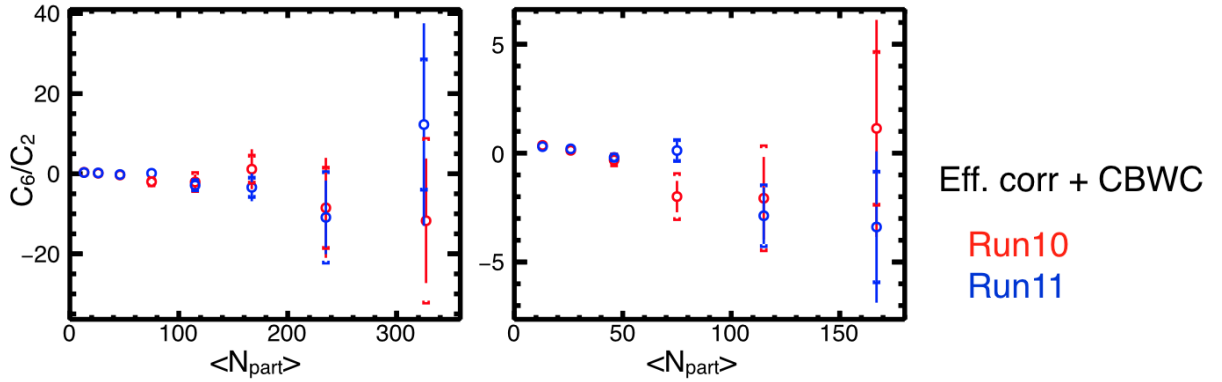


Figure 5.5: Centrality dependence of C_6/C_2 for Run10 and Run11. Statistical errors are shown in bars, while systematic uncertainties are shown in brackets. The expanded plot is shown in right hand side from 20% centrality.

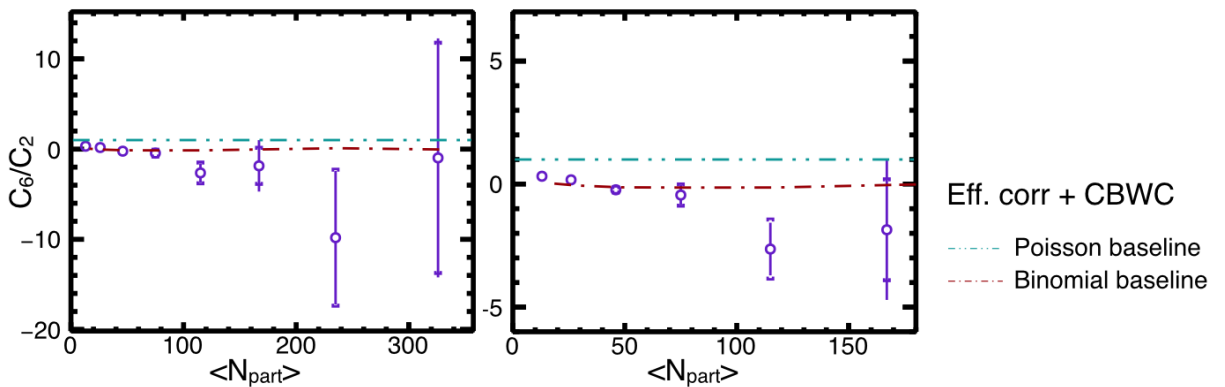


Figure 5.6: C_6/C_2 as a function of centrality, where results from Run10 and Run11 are merged. The expanded plot is shown in right hand side from 20% centrality. Skellam and the binomial baselines are also shown.

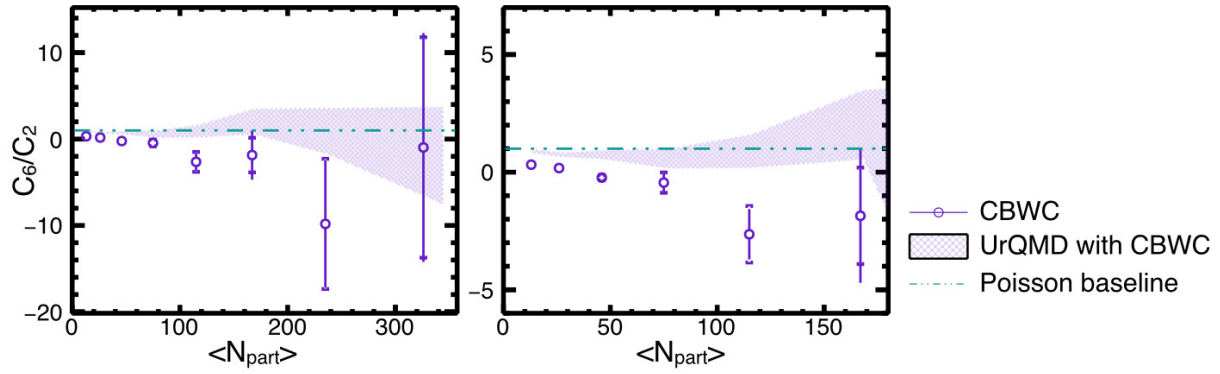


Figure 5.7: C_6/C_2 as a function of centrality with Skellam baseline and the results of UrQMD model. CBWC is applied in UrQMD model as is done in experimental data.

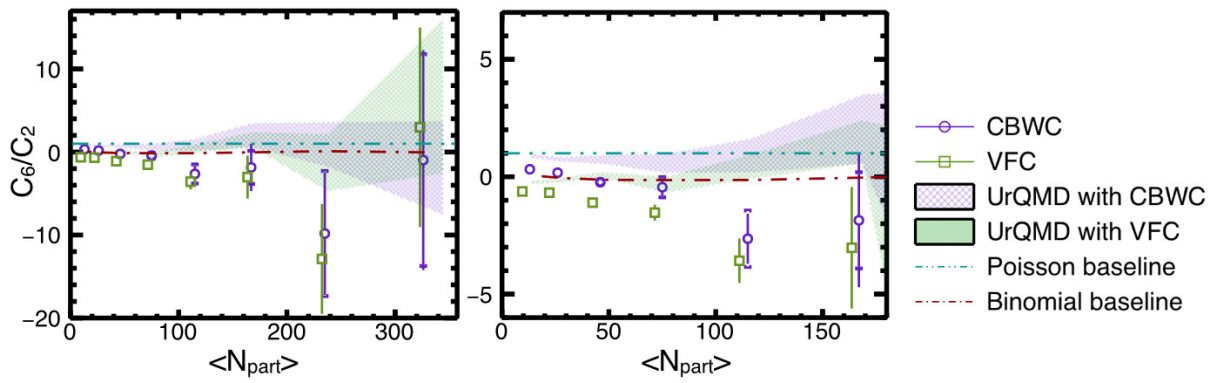


Figure 5.8: C_6/C_2 as a function of centrality using CBWC or VFC for both experimental data and UrQMD model. Results with CBWC are shown in purple and the results with VFC are in green. Results of UrQMD model are shown in band.

5.4 Interpretation

When one discusses the centrality dependence of higher order fluctuations, the finite size effect should be considered. In heavy ion collisions the system size is limited in the size of nucleus, which indicates that the fluctuations don't substantially grow up. In other words, number of produced particles is small in peripheral collisions, thus anything other than statistical fluctuations would not be observed, while the fluctuations will get larger in central collisions (but still restricted to the size of nuclei). Another issue is that one still doesn't know from which centrality QGP is created. If there is no QGP, off course, phase transition should not occur, which leads to null fluctuation. In order to see whether some signals from the phase transition are observed or not, the significance with respect to zero is plotted as a function of centrality in Fig. 5.9. For CBWC results, it is found that the C_6/C_2 shows the systematic reduction from positive to negative values in peripheral and semi-central collisions. It can be understood by the absence of QGP or finite size effect. Even in semi-central collisions, QGP might be created and C_6/C_2 would become more sensitive to the phase transition than finite size effect, then the negative values of C_6/C_2 are observed.

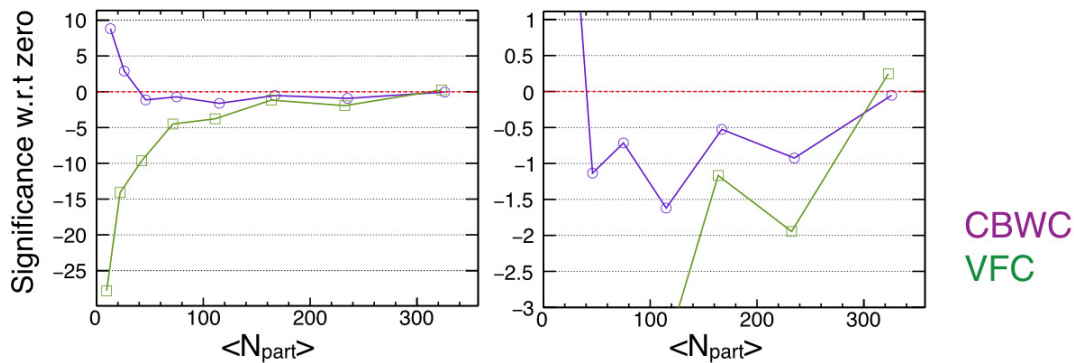


Figure 5.9: Significance with respect to zero as a function of centrality for CBWC and VFC. The expanded plot is shown in right hand side panel.

5.5 Comparison with theoretical calculations

The model calculation in Ref. [14] would provide us hints to restrict the location of the chiral crossover with respect to the chemical freeze-out. The results of C_4/C_2 and C_6/C_2 on net-proton distribution in 0-10 and 30-40 % centralities, as well as a rough estimates on χ_6^B/χ_2^B and χ_4^B/χ_2^B with different freeze-out conditions from model calculation [14] are summarized in Tabs. 5.2 and 5.3. It can be found that the experimental results are consistent with the freeze-out condition of $T^{\text{freeze}}/T_{pc} \simeq 1$. This is also consistent with the conjecture in Sec. 1.2.3 that the crossover region might be close enough to the chemical freeze-out line.

One should note that the absolute values in Fig. 1.9 is model dependent, quantitative comparisons can thus only be done with the lattice QCD calculation. Recently the value of χ_6^B/χ_2^B has been calculated by the lattice QCD [24], which is shown in Fig. 5.10 as a function of the temperature. At $\sqrt{s_{\text{NN}}}$, the chemical freeze-out temperature is around 166 MeV. Corresponding results from the lattice QCD are superimposed to the experimental results as red shadow in Fig. 5.11. It can be found that the experimental results do not conflict with the lattice QCD, but there are still large errors for both results. It should be also noted that the direct comparison with experiments and the lattice QCD

Centrality	0-10 %	30-40 %
C_4/C_2	0.98 ± 0.11	0.74 ± 0.03
C_6/C_2	-0.97 ± 18.4	-2.64 ± 1.63
	2.98 ± 12.0	-3.57 ± 0.95

Table 5.2: Results on C_4/C_2 and C_6/C_2 in 0-10 and 30-40 % centralities at Au+Au collisions $\sqrt{s_{NN}} = 200$ GeV. CBWC and VFC results are shown in upper and lower at each cell. (Statistical errors only)

	$T^{\text{freeze}}/T_{pc} \simeq 1$	$T^{\text{freeze}}/T_{pc} \leq 0.9$
χ_4^B/χ_2^B	~ 0.5	≥ 1
χ_6^B/χ_2^B	< 0	≥ 1

Table 5.3: Rough estimates on the ratio of fourth to second and sixth to second order baryon number susceptibilities with different freeze-out conditions.

would be difficult. There are several experimental effects that are not fully considered in the theory, such as the global baryon number conservation effect [42, 44], volume fluctuation effects [22, 42] and the difference between net-baryon with net-proton [36].

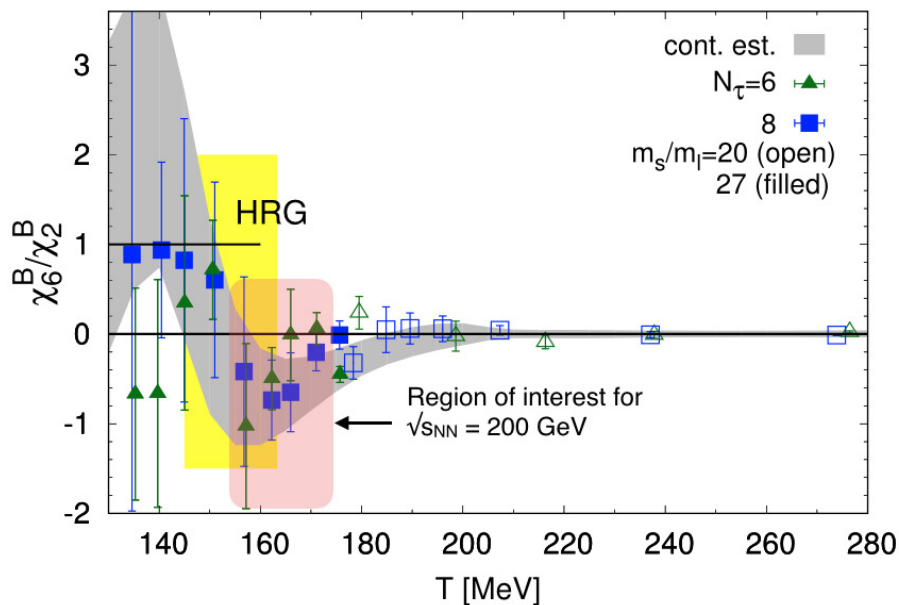


Figure 5.10: χ_6^B/χ_2^B calculated with the lattice QCD as a function of temperature [24]. The red shaded area is the region of interest at $\sqrt{s_{NN}} = 200$ GeV.

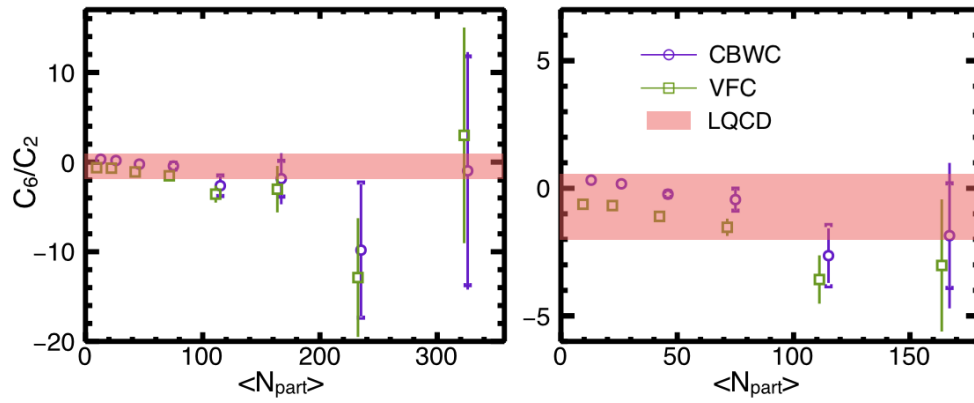


Figure 5.11: Final results on C_6/C_2 of net-proton distribution at $\sqrt{s_{\text{NN}}} = 200$ GeV, where the corresponding results calculated by the lattice QCD on the ratio of sixth to second order susceptibility of the net-baryon distribution [24] are superimposed in red shadows.

Chapter 6

Conclusions

The ratio of the sixth to second order cumulant of net-proton multiplicity distributions in Au+Au collisions at $\sqrt{s_{\text{NN}}} = 200$ GeV at the STAR experiment has been measured as a function of centrality. The experimental non-binomial detector efficiency was determined by using the embedding simulations. The non-binomial model was implemented into the unfolding, and it was found that the non-binomial detector effect was negligible, which indicates that the analytical correction for the binomial detector efficiency is applicable to the data. Regarding the volume fluctuation effect arising from the participant fluctuations, it was found that both CBWC and VFC would not be correct by using the UrQMD model. VFC was applied to C_3/C_2 and C_4/C_2 at $\sqrt{s_{\text{NN}}} = 7.7, 19.6, 62.4$ and 200 GeV. In most centralities and beam energies, VFC results are systematically smaller than CBWC results. It was found that the non-monotonic behaviour, which could be possible signature of the critical end point, observed in C_4/C_2 as a function of beam energy using CBWC was robust even if VFC is applied instead of CBWC. Both CBWC and VFC were applied to C_6/C_2 . For CBWC, the results show positive values in the peripheral collisions and negative values in central collisions systematically. This could be possibly a signature of the crossover phase transition in central collisions. For VFC, on the other hand, the results show negative values for all centralities, which could indicate that the QGP is formed and the phase transition is probed even in peripheral collisions. The results show systematically smaller values compared to the statistical baselines and the UrQMD model. Based on the theoretical calculation, observed negative values of C_6/C_2 would indicate that the chiral crossover region is located near the chemical freeze-out line. The result was also compared with the lattice QCD. The experimental and lattice QCD results are consistent with large errors. However, one should note several effects like volume fluctuations, global baryon number conservation, and the difference between the net-baryon and net-proton, which are not fully understood. Further development of experiments and theories would be essential to extract more definite information on the QCD phase structure.

Appendix A

Centrality definition

Based on Sec. 4.1, we used charged pions and kaons measured by TPC in $|\eta| < 1.0$, that we call `refmult3`, for the centrality determination. Figure A.1 shows averaged `refmult3` as a function of ZDC coincidence rate which represents the luminosity. We can see that `refmult3` decreases with increasing the luminosity as shown in blue markers, which was corrected as shown in red markers. After luminosity correction, we looked at the `refmult3` distributions as shown in the left hand side in Fig. A.2 to perform fitting with following function:

$$f(x) = a \times \text{Erf}(-b \times (x - c)) + a, \quad (\text{A.1})$$

$$\text{Erf}(x) = \frac{2}{\sqrt{\pi}} \int_0^x e^{-t^2} dt, \quad (\text{A.2})$$

where $\text{Erf}(x)$ is the error function and c was extracted as a parameter which represents the maximum value of `refmult3` distribution. This was performed at different V_z windows with 2 cm step, which is plotted as a function of V_z in the right hand side in Fig. A.2, where we observe V_z dependence which was corrected by 2nd polynomial fitting.

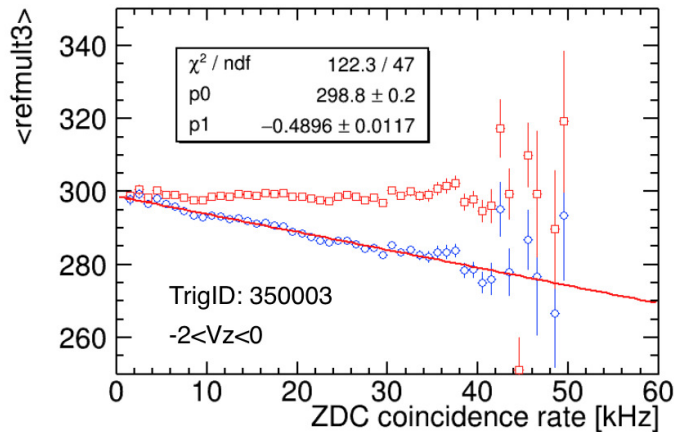


Figure A.1: Luminosity dependence of averaged `refmult3` in $-2 < V_z < 0$ cm. Blue markers are uncorrected and fitted by first order polynomial function (red lines) which is used for the correction. Corrected results are shown in blue markers.

After luminosity and acceptance corrections, we define the centrality. Since trigger efficiency drops in peripheral collisions, experimental measured multiplicity distribution cannot be directly used to di-

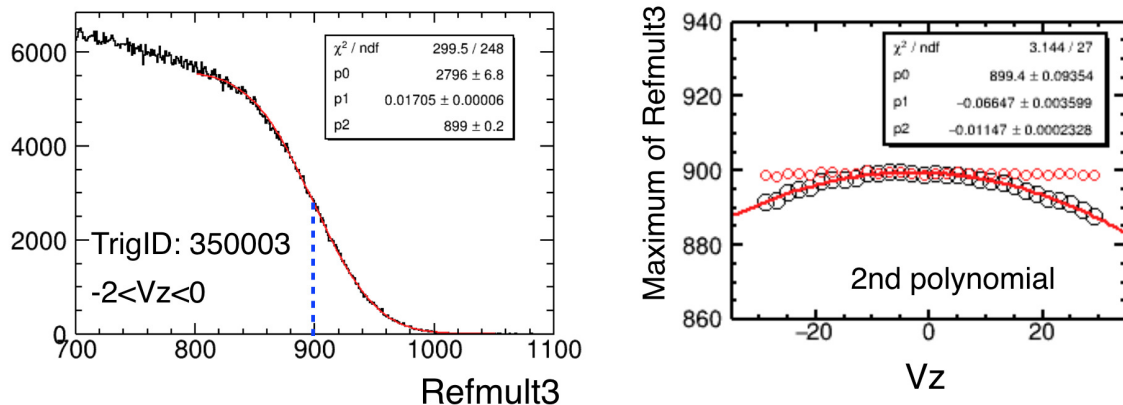


Figure A.2: (Left) Tail of the refmult3 distribution fitted by error function shown in a red line. The blue dotted line represents the parameter c in Eq. (A.1). (Right) Maximum value of refmult3 distribution as a function of V_z (black) and the corrected distribution (red).

vide the centrality. So we have to perform some model calculations to reproduce the experimental measured multiplicity distribution except very peripheral collisions, which is used to divide the centrality. We used Glauber and two-component model to generate the multiplicity distributions. In Glauber model, inelastic cross section for p+p collisions are set to $\sigma_{pp} = 43.6$ (mb) at $\sqrt{s_{NN}} = 200$ GeV. Other parameters for geometry are set to be of Au nuclei. 100 M events were proceeded. Once the number of participant nucleons (N_{part}) and the number of binary collisions (N_{coll}) are determined by Glauber model, particles were generated by two-component model with negative binomial fluctuation:

$$N_{\text{prod}} = n_{\text{pp}} \left[(1-x) \frac{N_{\text{part}}}{2} + x N_{\text{coll}} \right], \quad (\text{A.3})$$

$$n_{\text{pp}} = \frac{\Gamma(a+k)}{\Gamma(a+1)\Gamma(0)} \frac{(\mu/k)^a}{(1+\mu/k)^{-a-k}} \quad (\text{A.4})$$

where x is the fraction of hard component in particle production, n_{pp} represents the number of produced particles per unit p+p collision, and Γ represents the gamma function. In each collision event, the number of "source" for particle production is determined according to the second terms shown in the first equation, then particles are generated from the "source" by n_{pp} , which is randomly selected by the negative binomial distribution in the second equation. Multiplicity dependent efficiency were also implemented to reproduce the multiplicity distribution at the STAR experiment:

$$N_{\text{meas}} = \varepsilon_{\text{mult}} \times N_{\text{prod}}, \quad (\text{A.5})$$

$$\varepsilon_{\text{mult}}(N_{\text{prod}}) = 0.98 \left(1 - \varepsilon_{\text{const}} \frac{N_{\text{prod}}}{560} \right), \quad (\text{A.6})$$

where the slope of N_{meas} distribution can be controlled by $\varepsilon_{\text{const}}$. Those parameters were selected so that the N_{meas} distributions can well reproduced the refmult3 distribution in $\text{refmult3} > 100$, which is shown in the left hand side in Fig. A.3, where red points represent N_{meas} distribution and black points are refmult3 distribution. Right hand side panel in Fig. A.3 shows the ratio of N_{meas} to refmult3 distributions. We can see the fitting is good (χ^2/ndf) except $\text{refmult3} < 100$. The blue line is the fitting in $\text{refmult3} < 100$, which can be used for trigger inefficiency correction for cumulant analysis. MC multiplicity distribution are divided into 9 centrality classes, 0-5%, 5-10% and 10% step up to

70-80% centrality. Table A.1 shows the results of centrality definition, where low edge multiplicity bin and the averaged number of participant nucleons for each centrality class are shown.

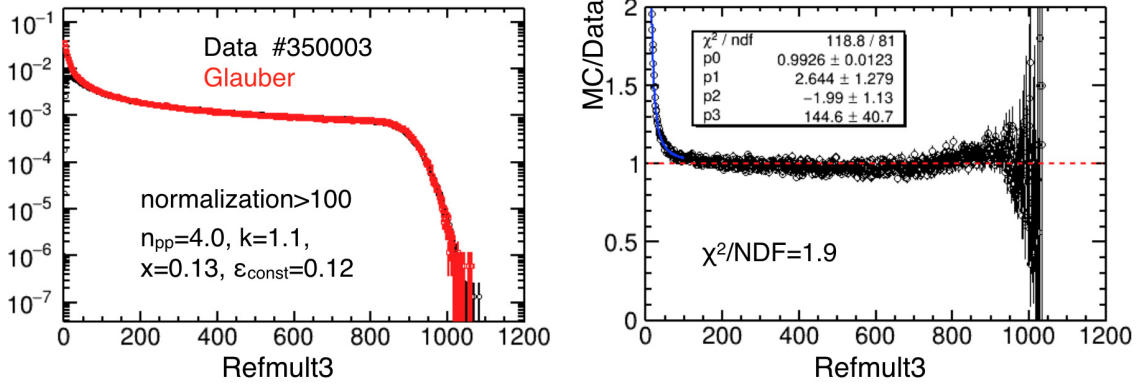


Figure A.3: (Left) Refmult3 distribution (black points) fitted by MC distribution generated by Glauber and two-component model (red points). (Right) Ratio of MC to refmult3 distribution. The solid blue line represents the fitting for trigger inefficiency correction.

Centrality(%)	Low edge bin	$\langle N_{part} \rangle$
0–5	784	350
5–10	674	300
10–20	484	235
20–30	332	167
30–40	216	115
40–50	131	75
50–60	73	47
60–70	36	26
70–80	15	13

Table A.1: Summary for the centrality definition at $\sqrt{s_{NN}} = 200$ GeV in run11 datasets. The middle row shows the low edge refmult3 bin and the right row is the averaged number of participant nucleons.

Appendix B

Tips on the efficiency correction

B.1 Stirling number of the first kind

The falling factorial moment is defined by using Stirling number of the first kind as:

$$(x)_n = \sum_{k=0}^n s(n, k)x^k, \quad (\text{B.1})$$

with $s(n, k)$ being the Stirling number of the first kind, which is given by

$$s(n, k) = (-1)^{n-k} \binom{n}{k}, \quad \binom{n}{k} = |s(n, k)|. \quad (\text{B.2})$$

The second equation represent the unsigned Stirling number of the first kind, which is calculated by the following recursive relation:

$$\binom{n+1}{k} = n \binom{n}{k} + \binom{n}{k-1}, \quad (\text{B.3})$$

with the initial condition

$$\binom{0}{0} = 1, \quad \binom{n}{0} = \binom{0}{n} = 0. \quad (\text{B.4})$$

B.2 Factorial moments with the binomial model

In this section, I introduce Eq. (3.5) which holds under the binomial model. For convenience, I use the Pochhammer symbol

$$(x)_i = x(x-1)(x-2) \cdots (x-i+1) = \frac{x!}{(x-i)!}. \quad (\text{B.5})$$

Starting from Eq. (3.3),

$$\begin{aligned}
f_{ab} &= \left\langle \sum_{i=0}^a s(a, i) M^i \sum_{j=0}^b s(b, j) \bar{M}^j \right\rangle \\
&= \sum_{M, \bar{M}} p(M, \bar{M}) \times (M)_a (\bar{M})_b \\
&= \sum_{M, \bar{M}} (M)_a (\bar{M})_b \sum_{N, \bar{N}} P(N, \bar{N}) \frac{N!}{M!(N-M)!} \varepsilon^M (1-\varepsilon)^{N-M} \frac{\bar{N}!}{\bar{M}!(\bar{N}-\bar{M})!} \bar{\varepsilon}^{\bar{M}} (1-\bar{\varepsilon})^{\bar{N}-\bar{M}} \\
&= \sum_{N, \bar{N}} P(N, \bar{N}) \sum_{M, \bar{M}} \frac{M!}{(M-a)!} \frac{\bar{M}!}{\bar{M}-b} \frac{N!}{M!(N-M)!} \frac{\bar{N}!}{\bar{M}!(\bar{N}-\bar{M})!} \varepsilon^M \bar{\varepsilon}^{\bar{M}} (1-\varepsilon)^{N-M} (1-\bar{\varepsilon})^{\bar{N}-\bar{M}} \\
&= \sum_{N, \bar{N}} P(N, \bar{N}) (N)_a (\bar{N})_b \sum_{M, \bar{M}} \frac{(N-a)!}{(M-a)!(N-M)!} \frac{(\bar{N}-b)!}{(\bar{M}-b)!(\bar{N}-\bar{M})!} \varepsilon^M \bar{\varepsilon}^{\bar{M}} (1-\varepsilon)^{N-M} (1-\bar{\varepsilon})^{\bar{N}-\bar{M}} \\
&= \sum_{N, \bar{N}} P(N, \bar{N}) (N)_a (\bar{N})_b \varepsilon^a \bar{\varepsilon}^b \sum_{M=a}^{\infty} B(N-a, M-a; \varepsilon) \sum_{\bar{M}=b}^{\infty} B(\bar{N}-b, \bar{M}-b; \bar{\varepsilon}) \\
&= \varepsilon^a \bar{\varepsilon}^b F_{ab}.
\end{aligned} \tag{B.6}$$

Appendix C

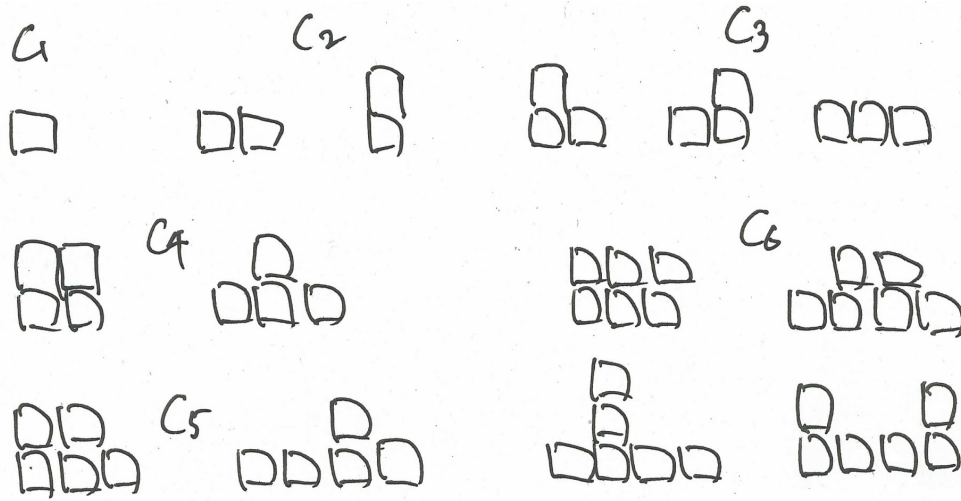
Net-proton distribution

In this appendix, the shape of the net-proton distribution is discussed. Corrected cumulants deviate from the Skellam expectation. Furthermore, higher order cumulants more than second order have been observed, which indicates that the observed net-proton distribution is no longer the Gaussian. The unfolded distribution is compared with the Skellam and Gaussian distribution and discuss how the values of higher order cumulants up to the sixth order could appear as the shape of the distribution.

C.1 Shape for the sixth order cumulant

As was explained in Sec. 1.3, the third order cumulant represents the asymmetry of the distribution, and the fourth order cumulant represents the sharpness of the distribution. What about for the fifth and sixth order cumulant? For our intuitive understanding, let us consider to stack n boxes for the n -th order cumulant, and suppose that the structure made by n boxes represents the shape of the distribution. Figure C.1 shows a simple sketch for up to the sixth order. For one box, the box can only be located there without any other choices. For two boxes, two boxes can be placed vertically or horizontally, the entire shape of two boxes can thus represent the width of the distribution. By adding another box, for three boxes, the last one box can be placed at the right or left hand side of vertically stacked two boxes, which represents the asymmetry of the distribution. For four boxes, box-like and convex upward shape can be considered. In the case of five and six boxes, the degree of freedom at the top and side part of the distribution is added with respect to the cases of three and four boxes, respectively. Therefore, the "expanded" or "dented" shape at the side and top part of the distribution could be possibly the reason for the finite value of the sixth order cumulant.

A simple toy model has been performed to check this conjecture. First, a Gaussian distribution with mean and sigma being 0 and 5 is generated. In order to change the shape around the side part of the Gaussian, additional two Gaussians are also prepared, which have the mean value of ± 15 and the sigma of 1. The original Gaussian is then modified to be expanded or dented shape by adding or subtracting two symmetric Gaussians, which are shown in Fig. C.2. The ratio of the modified distribution to the Gaussian fitting in bottom panels. The kink structure is observed around $N = 15$, which represents the dented and expanded shape. Cumulants up to the sixth order on the two distributions are shown in Tab. C.1. For the ordinary Gaussian distribution, higher order cumulants become zero by definition. Even for the expanded and dented distributions, they are still symmetric, C_3 and C_5 are thus zero. But the even order cumulants are affected. For the expanded distribution, the shape around the top becomes relatively sharper than the side part, so the value of C_4 are positive. On the other hand, the value of C_4 of the dented distribution is negative. It can be also found that the value of C_6 is negative for the expanded distribution, while positive for the dented one. Therefore,

Figure C.1: A simple sketch to stack n boxes for the n -th order cumulant.

the observed negative value of C_6 could be observed as the expanded shape around the side part of the distribution.

Cumulants	Gaussian	expanded	dented
C_1	0	0	0
C_2	25	25.88 ± 0.01	24.69 ± 0.01
C_3	0	0	0
C_4	0	77.39 ± 1.03	-40.17 ± 0.99
C_5	0	0	0
C_6	0	-5890 ± 133	2131 ± 127

Table C.1: Cumulants up to the sixth order on the distributions in Fig. C.2.

C.2 Net-proton distribution

Let us compare the observed net-proton distribution with the conjectures discussed in previous section. Top panels in Fig. C.3 shows the net-proton distributions in 0-5, 30-40 and 70-80 % centralities. Blue squares are the measured distribution. Red circles are unfolded distribution assuming the binomial model. Black lines represent Skellam distributions, and dotted green lines are Gaussian distributions. The ratios of the unfolded distribution to the Skellam and Gaussian distributions are shown in the bottom panels. Since the unfolded distribution includes the effect of the volume fluctuation, corresponding cumulants are red open squares in Fig. 5.2 in which any volume fluctuation corrections are not applied. Unfolded distributions are a bit narrower than the Skellam distributions in all centralities, which leads to the shape of convex upward as is seen in the ratio in Fig. C.3. This is consistent with the results on C_2 . In 0-5 and 30-40% centralities, the ratio of the unfolded to the Skellam distribution are skew to the left hand side. This asymmetry is also observed in the ratio of the unfolded to the Gaussian distribution. Larger C_3 than the Skellam baseline in Fig. 5.2 is thus observed. In addition, the ratio of the unfolded to the Gaussian distribution behaves like "W". This indicates that the

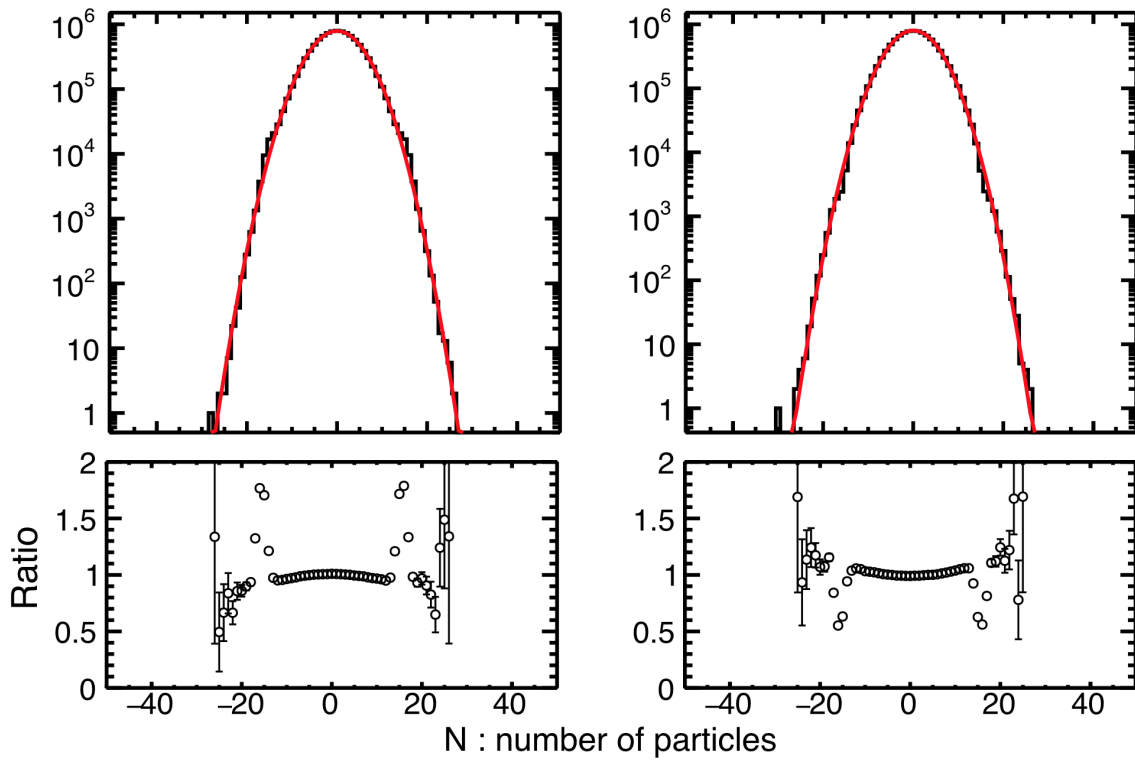


Figure C.2: Gaussian distributions with the mean value of 0 and the sigma of 5, in which another two symmetric Gaussians around $N = \pm 15$ are added (left) or subtracted (right). Red lines represent the Gaussian fittings. The ratio to the fitting are shown in the bottom panels.

unfolded distribution is sharper than the Gaussian, which can explain the positive C_4 . Interestingly, some modifications like convex upward are observed at $N = -5$ and 20 in 0-5 %, and at $N = -8$ and 10 in 30-40 % centrality in the ratio of the unfolded to the Skellam distributions. Such modifications cannot be explained by cumulants up to the fourth order, which could be the origin of the finite C_6 in 30-40% centrality. One should note that the error bar of the unfolded distribution is not correct. The current unfolding technique cannot allow us to calculate errors on the distribution but errors on the cumulants. Thus the observed modification of the unfolded distribution might be negligible including true errors.

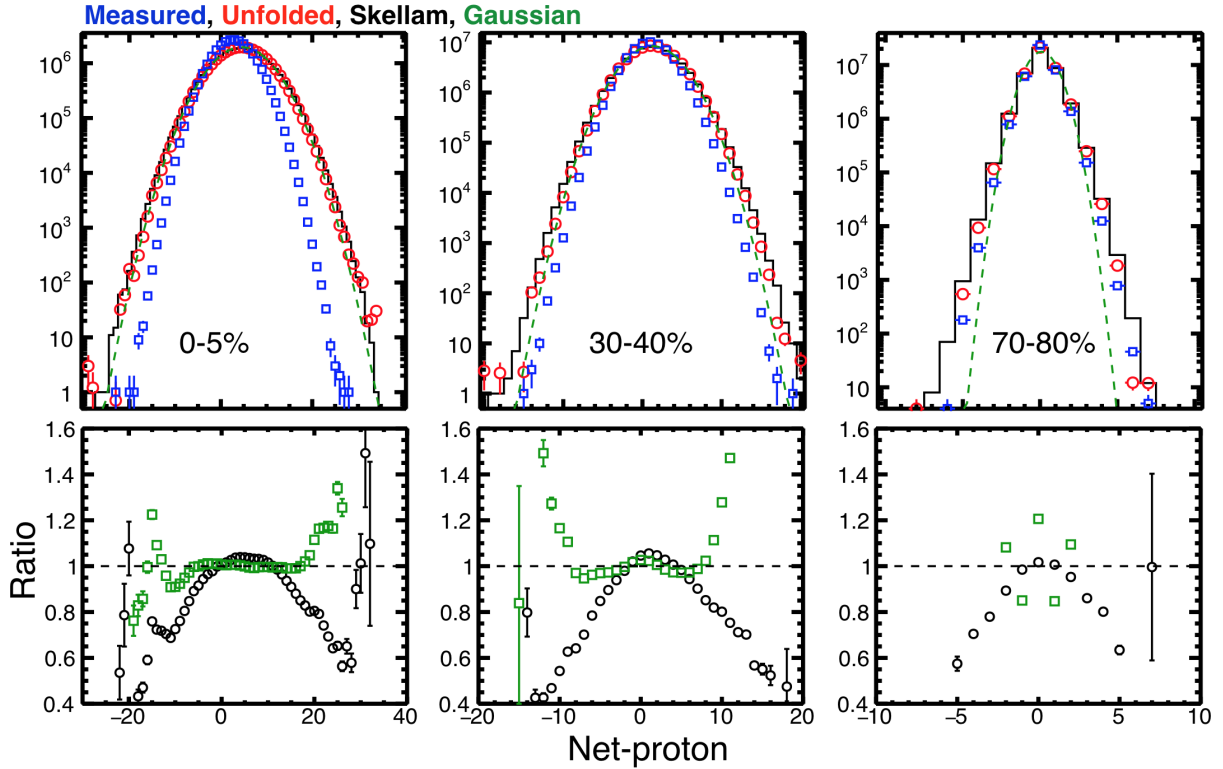


Figure C.3: (Top) Net-proton distributions in 0-5, 30-40 and 70-80% centralities. Blue squares are the measured distribution. Red circles are unfolded distribution without any volume fluctuation corrections. Black lines represent Skellam distributions, and dotted green lines are Gaussian distributions. (Bottom) Ratios of the unfolded distribution to the Skellam and Gaussian distributions.

Appendix D

Robustness to the time dependence

According to Fig. 2.12, it can be found that the total multiplicity has time dependence, which is around $\pm 5\%$ in 3σ . Assuming that the single particle efficiency directly depends on the total multiplicity, the efficiency variation could be assumed to be within $\pm 5\%$. This efficiency variation has been included in the systematic studies. Here some hints will be given on how much robust the higher order cumulants are, assuming that the efficiency drops in some fractions of total statistics by using a simple toy model. Protons and antiprotons are generated with 100 M events with mean values of 5.64 and 4.39. The efficiencies are assumed to be $\varepsilon = 0.65$, which corresponds to 30-40 % centrality at $\sqrt{s_{\text{NN}}}$ 200 GeV. The efficiency is dropped with $\Delta\varepsilon$ in some "bad" events, then apply the efficiency correction by using $\varepsilon = 0.65$. Figure D.1 shows the relative difference to the true value of cumulants up to the sixth order as a function of the fraction of bad events which have the efficiency of $\varepsilon(1 - \Delta\varepsilon)$ with $\Delta\varepsilon = 0.05, 0.2, \text{ and } 0.4$. It can be found that the effect is smaller than 1 % for $\Delta\varepsilon = 0.05$ for all the order of cumulants. For the case of $\Delta\varepsilon = 20\%$, C_3 and C_4 start to deviate significantly from 5% fraction of bad events, whereas the effects on C_5 and C_6 are statistically negligible. As a simple criterion, therefore, the fraction of bad events in which the efficiency drops 20 % has to be controlled to be less than 5 % in order to measure cumulants up to the fourth order with 1 % accuracy.

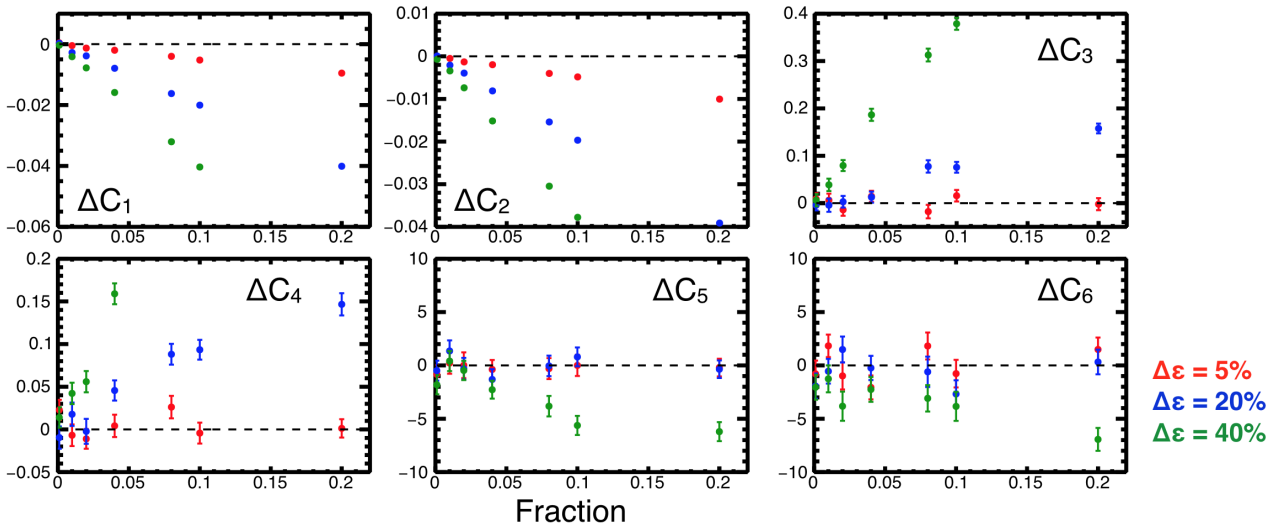


Figure D.1: Relative deviations with respect to the true value of cumulants up to the sixth order as a function of the fraction of bad events in which the efficiency drops with $\Delta\varepsilon$.

Bibliography

- [1] **Particle Data Group** Collaboration, J. Beringer *et al.*, *Review of Particle Physics (RPP)*, *Phys. Rev.* **D86** (2012) 010001.
- [2] **CP-PACS** Collaboration, A. Ali Khan *et al.*, *Light hadron spectroscopy with two flavors of dynamical quarks on the lattice*, *Phys. Rev.* **D65** (2002) 054505, [[hep-lat/0105015](#)]. [Erratum: *Phys. Rev.* **D67**, 059901(2003)].
- [3] K. Fukushima and T. Hatsuda, *The phase diagram of dense QCD*, *Rept. Prog. Phys.* **74** (2011) 014001, [[1005.4814](#)].
- [4] C. Nonaka and M. Asakawa, *Modeling a Realistic Dynamical Model for High Energy Heavy Ion Collisions*, *PTEP* **2012** (2012) 01A208, [[1204.4795](#)].
- [5] **STAR** Collaboration, L. Adamczyk *et al.*, *Bulk Properties of the Medium Produced in Relativistic Heavy-Ion Collisions from the Beam Energy Scan Program*, *Phys. Rev.* **C96** (2017), no. 4 044904, [[1701.07065](#)].
- [6] **STAR** Collaboration, L. Adamczyk *et al.*, *Beam Energy Dependence of Jet-Quenching Effects in Au+Au Collisions at $\sqrt{s_{NN}} = 7.7, 11.5, 14.5, 19.6, 27, 39,$ and 62.4 GeV*, [1707.01988](#).
- [7] **STAR** Collaboration, L. Adamczyk *et al.*, *Beam-Energy Dependence of the Directed Flow of Protons, Antiprotons, and Pions in Au+Au Collisions*, *Phys. Rev. Lett.* **112** (2014), no. 16 162301, [[1401.3043](#)].
- [8] **STAR** Collaboration, L. Adamczyk *et al.*, *Beam energy dependence of moments of the net-charge multiplicity distributions in Au+Au collisions at RHIC*, *Phys. Rev. Lett.* **113** (2014) 092301, [[1402.1558](#)].
- [9] **STAR** Collaboration, L. Adamczyk *et al.*, *Energy Dependence of Moments of Net-proton Multiplicity Distributions at RHIC*, *Phys. Rev. Lett.* **112** (2014) 032302, [[1309.5681](#)].
- [10] **STAR** Collaboration, L. Adamczyk *et al.*, *Collision Energy Dependence of Moments of Net-Kaon Multiplicity Distributions at RHIC*, [1709.00773](#).
- [11] X. Luo, *Exploring the QCD Phase Structure with Beam Energy Scan in Heavy-ion Collisions*, *Nucl. Phys.* **A956** (2016) 75–82, [[1512.09215](#)].
- [12] M. A. Stephanov, *On the sign of kurtosis near the QCD critical point*, *Phys. Rev. Lett.* **107** (2011) 052301, [[1104.1627](#)].
- [13] S. Borsanyi, G. Endrodi, Z. Fodor, A. Jakovac, S. D. Katz, S. Krieg, C. Ratti, and K. K. Szabo, *The QCD equation of state with dynamical quarks*, *JHEP* **11** (2010) 077, [[1007.2580](#)].

- [14] B. Friman, F. Karsch, K. Redlich, and V. Skokov, *Fluctuations as probe of the QCD phase transition and freeze-out in heavy ion collisions at LHC and RHIC*, *Eur. Phys. J.* **C71** (2011) 1694, [1103.3511].
- [15] M. Asakawa and M. Kitazawa, *Fluctuations of conserved charges in relativistic heavy ion collisions: An introduction*, *Prog. Part. Nucl. Phys.* **90** (2016) 299–342, [1512.05038].
- [16] M. Anderson *et al.*, *The Star time projection chamber: A Unique tool for studying high multiplicity events at RHIC*, *Nucl. Instrum. Meth.* **A499** (2003) 659–678, [nucl-ex/0301015].
- [17] X. Zhang, *Lifetime Calculations for Unstable Nuclei and ϕ Meson Production at RHIC*. PhD thesis, Nanjing University, 2010.
- [18] W. J. Llope, *The large-area time-of-flight upgrade for STAR*, *Nucl. Instrum. Meth.* **B241** (2005) 306–310.
- [19] W. J. Llope *et al.*, *The STAR Vertex Position Detector*, *Nucl. Instrum. Meth.* **A759** (2014) 23–28, [1403.6855].
- [20] X. Luo, *Search for experimental signatures of critical point with beam energy scan at STAR*, in *CiRfSE workshop 2016*.
- [21] T. Nonaka, M. Kitazawa, and S. Esumi, *More efficient formulas for efficiency correction of cumulants and effect of using averaged efficiency*, *Phys. Rev.* **C95** (2017), no. 6 064912, [1702.07106].
- [22] X. Luo, J. Xu, B. Mohanty, and N. Xu, *Volume fluctuation and auto-correlation effects in the moment analysis of net-proton multiplicity distributions in heavy-ion collisions*, *J. Phys.* **G40** (2013) 105104, [1302.2332].
- [23] X. Luo, *Energy Dependence of Moments of Net-Proton and Net-Charge Multiplicity Distributions at STAR*, vol. CPOD2014, 2015. 1503.02558.
- [24] A. Bazavov *et al.*, *The QCD Equation of State to $\mathcal{O}(\mu_B^6)$ from Lattice QCD*, *Phys. Rev.* **D95** (2017), no. 5 054504, [1701.04325].
- [25] M. Cheng *et al.*, *The Transition temperature in QCD*, *Phys. Rev.* **D74** (2006) 054507, [hep-lat/0608013].
- [26] Y. Aoki, G. Endrodi, Z. Fodor, S. D. Katz, and K. K. Szabo, *The Order of the quantum chromodynamics transition predicted by the standard model of particle physics*, *Nature* **443** (2006) 675–678, [hep-lat/0611014].
- [27] M. A. Stephanov, *QCD phase diagram: An Overview*, *PoS LAT2006* (2006) 024, [hep-lat/0701002].
- [28] O. Philipsen, *Status of the QCD Phase Diagram from Lattice Calculations*, *Acta Phys. Polon. Supp.* **5** (2012) 825–835, [1111.5370].
- [29] **STAR** Collaboration, L. Adamczyk *et al.*, *Beam-energy dependence of charge separation along the magnetic field in Au+Au collisions at RHIC*, *Phys. Rev. Lett.* **113** (2014) 052302, [1404.1433].

- [30] **STAR** Collaboration, L. Adamczyk *et al.*, *Beam Energy Dependence of the Third Harmonic of Azimuthal Correlations in Au+Au Collisions at RHIC*, *Phys. Rev. Lett.* **116** (2016), no. 11 112302, [1601.01999].
- [31] H. Stoecker, *Collective flow signals the quark gluon plasma*, *Nucl. Phys.* **A750** (2005) 121–147, [nucl-th/0406018].
- [32] R. V. Gavai and S. Gupta, *Lattice QCD predictions for shapes of event distributions along the freezeout curve in heavy-ion collisions*, *Phys. Lett.* **B696** (2011) 459–463, [1001.3796].
- [33] A. Bzdak and V. Koch, *Acceptance corrections to net baryon and net charge cumulants*, *Phys. Rev.* **C86** (2012) 044904, [1206.4286].
- [34] A. Bzdak and V. Koch, *Local Efficiency Corrections to Higher Order Cumulants*, *Phys. Rev.* **C91** (2015), no. 2 027901, [1312.4574].
- [35] X. Luo, *Unified Description of Efficiency Correction and Error Estimation for Moments of Conserved Quantities in Heavy-Ion Collisions*, *Phys. Rev.* **C91** (2015), no. 3 034907, [1410.3914].
- [36] M. Kitazawa and M. Asakawa, *Relation between baryon number fluctuations and experimentally observed proton number fluctuations in relativistic heavy ion collisions*, *Phys. Rev.* **C86** (2012) 024904, [1205.3292]. [Erratum: *Phys. Rev.* **C86**, 069902(2012)].
- [37] X. Luo, *Error Estimation for Moments Analysis in Heavy Ion Collision Experiment*, *J. Phys.* **G39** (2012) 025008, [1109.0593].
- [38] A. Bzdak, R. Holzmann, and V. Koch, *Multiplicity dependent and non-binomial efficiency corrections for particle number cumulants* *Multiplicity-dependent and nonbinomial efficiency corrections for particle number cumulants*, *Phys. Rev.* **C94** (2016), no. 6 064907, [1603.09057].
- [39] T. Adye, *Unfolding algorithms and tests using RooUnfold*, in *Proceedings, PHYSTAT 2011 Workshop on Statistical Issues Related to Discovery Claims in Search Experiments and Unfolding*, CERN, Geneva, Switzerland 17-20 January 2011, (Geneva), pp. 313–318, CERN, CERN, 2011. 1105.1160.
- [40] **STAR** Collaboration, B. I. Abelev *et al.*, *Identified baryon and meson distributions at large transverse momenta from Au+Au collisions at $\sqrt{s_{NN}} = 200$ GeV*, *Phys. Rev. Lett.* **97** (2006) 152301, [nucl-ex/0606003].
- [41] A. Bzdak, R. Holzmann, and V. Koch, *Multiplicity dependent and non-binomial efficiency corrections for particle number cumulants* *Multiplicity-dependent and nonbinomial efficiency corrections for particle number cumulants*, *Phys. Rev.* **C94** (2016), no. 6 064907, [1603.09057].
- [42] P. Braun-Munzinger, A. Rustamov, and J. Stachel, *Bridging the gap between event-by-event fluctuation measurements and theory predictions in relativistic nuclear collisions*, *Nucl. Phys.* **A960** (2017) 114–130, [1612.00702].
- [43] M. Kitazawa, *Efficient formulas for efficiency correction of cumulants*, *Phys. Rev.* **C93** (2016), no. 4 044911, [1602.01234].
- [44] A. Bzdak, V. Koch, and V. Skokov, *Baryon number conservation and the cumulants of the net proton distribution*, *Phys. Rev.* **C87** (2013), no. 1 014901, [1203.4529].